Study of Higgs Self-couplings at the International Linear Collider (ILC)

Junping Tian

A Thesis submitted for the degree of Doctor of Philosophy

Physics

Tsinghua University

May 2011

Declaration

I hereby certify that the work presented in this thesis is my own.

Junping Tian

To my beloved **Luming**.

Contents

Acknowledgement

First, I would like to thank my supervisor Prof. Yuanning Gao, providing me the chance that made this PhD possible. Thank you for leading me to the frontier of Particle Physics with the constant support, encouragement and guidance. Second, I would like to express my heartfelt gratitude to Prof. Keisuke Fujii, who supervised most of the work in this thesis. Without his help and discussion during my visit at KEK, this thesis could not be possible. I am also greatly indebted to Prof. Xiaoyan Shen, who instructed me into the existing experiment being carried out at BESII. She has instructed and helped me during the two years when I visited IHEP.

I would like to express my deepest gratitude to my parents and wife for their loving considerations and great confidence in me all through these years. I also owe my gratitude to my friends and my fellow classmates of Center for High Energy Physics, Tsinghua University, who gave me lots of help and enjoyment.

Special thanks to Dr. Zhenwei Yang, who gave much support for typesetting this thesis.

Abstract

The Higgs Sector is the piece of Standard Model which is responsible for the spontaneous breaking of electroweak symmetry; the Higgs boson is the last particle of the Standard Model to be found by experiment. Once a Higgs-like boson is discovered, probably at LHC, we need to verify that it is indeed the Higgs boson that condenses in the vacuum and gives masses to all the standard model particles. Higgs self-coupling is just the force that makes the Higgs boson condense in the vacuum, therefore probe of this coupling is one of the most decisive test. For a light Higgs which dominantly decays into $b\bar{b}$, it will be very difficult if not impossible to measure its self-coupling at the LHC. It therefore becomes crucial to measure it at the proposed International Linear Collider (ILC).

The double Higgs-strahlung process ZHH and WW fusion process $\nu\bar{\nu}$HH are the leading channels to perform Higgs self-coupling measurement at ILC. In this thesis, full simulations of three decay modes of ZHH at 500 GeV have been carried out based on the detector concept ILD, assuming a Higgs mass of 120 GeV/c^2. Two of the three modes, ZHH decaying to l^+l^-HH and $\nu\bar{\nu}$HH, are fully simulated for the first time. Combing these with the $q\bar{q}$HH mode and using 2 ab^{-1} data, a 3.9σ significance is expected for observing the excess of ZHH events; the ZHH cross-section can be measured to an accuracy of 32%, corresponding to a precision of 57% on the trilinear Higgs self-coupling.

Using fast simulation the WW fusion at 1 TeV is also investigated. The $\nu\bar{\nu}$HH mode is used for this study; a 2.4σ excess is expected and the cross-section can be determined to a precision of 52%, corresponding to an accuracy of 44% on the trilinear Higgs self-coupling. The processes $t\bar{t}$, ZZ, ZZZ and ZZH are the dominant backgrounds and their cross sections are much larger than that of signal. A multivariate analysis, neural network, is used to improve the background suppression.

A study of J/ψ decays into $\eta K^{*0}\overline{K}^{*0}$ based on BESII is completed, where the branching ratio determination is a first measurement of this quantity. This study can be found in the Appendix.

Key words: ILC; ILD; Higgs; Self-coupling; Neural-net

Chapter 1

Introduction to the accelerator and detector

The proposed **I**nternational **L**inear **C**ollider (ILC) is a linear electron-positron collider based on 1.3 GHz superconducting radio-frequency (SCRF) accelerating cavities, working in the centre of mass energy from about 200 to 500 GeV and onwards to the region of 1 TeV. The physics at ILC will be extremely rich and important, complementing the possible discoveries at the **L**arge **H**adron **C**ollider (LHC) now running at CERN and finally making it possible to reveal the mysteries of origin of mass, super symmetry, dark matter, asymmetry of matter and anti-matter, and unification of the four fundamental interactions.

The world wide ILC research and development (R&D) are still ongoing aiming to the full demonstration of both the construction and physics goal it will achieve. There are three major milestones in the past ILC roadmap, first of which is the creation of the Baseline Configuration Document (BCD) [1] in 2005, second the publication of the draft ILC Reference Design Report (RDR) [2] in 2006 and the last of which is that two of the three detector concepts for ILC are validated in 2009. The validated detectors are ILD [3] and SiD [4], where the former is developed from two concepts GLD [5] and LDC [6]. Another detector concept is Fourth [7] which however is not validated. The next milestone will be the release of Technical Design Report (TDR) at the end of 2012, after which the ILC is ready for the final phase before construction.

In this chapter, a brief introduction to the ILC accelerator and ILD detector will be given. Several topics about the choices of ILC parameters which all the studies in the following chapters are based on will be discussed, leaving the technical details in references.

1.1 The Accelerator

1.1.1 Layout of the accelerator

The ILC as designed in the RDR [2] is an approximately 31 km long linear machine for accelerating the electrons and positrons. Figure 1.1 shows the schematic view of the baseline layout, where the major sub-systems are indicated: electron source, positron source, damping rings, main linacs, beam delivery system and detectors.

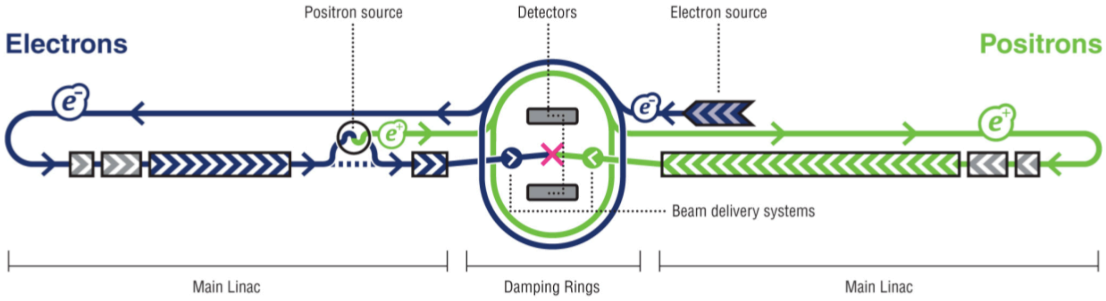

Figure 1.1: The schematic view of the ILC baseline layout.

- The **electron source** is located at the positron main linac side, where the electrons are produced by a laser illuminating the photocathode in a Direct Current (DC) gun. The electron beam can be polarized to above the level of 80% and then be accelerated to 5 GeV through a 250 meter pre-accelerating structure which is based on SCRF. The pre-accelerated beam will be delivered to the damping ring.

- The **positron source** is located at the electron main linac side. While positrons do not naturally exist, first we will send the accelerated high energy electron beam (about 150 GeV) through an undulator which is made of special arranged magnets. In the undulator, electrons will be forced to make a wobbing motion and then emit a stream of photons (about 10 MeV). These photons will hit a titanium-alloy target and produce electron-positron pairs. Then the positrons will be collected and also be boosted to 5 GeV by a pre-accelerating structure.

- The **damping rings** are made of one electron ring and one positron ring, each 6.7 km long, located near the center of the site. As mentioned above, the pre-accelerated electron and positron beams (5 GeV) will be sent to the damping rings, because at that point neither the electron nor the positron bunches are compact enough to yield the high density needed to produce collision in the detectors. The damping rings will reduce the beam emittances to a very low level required for luminosity production (the effect of emittance to luminosity will be discussed in the following section), damp incoming beam jitter and provide highly stable beams for downstream systems.

- The **main linacs** are respectively located in the two sides, each 11.5 km long. Electron and positron beams are accelerated from 15 GeV (the 5 GeV beams from damping rings are transported by the rings to main linacs which accelerate the beams to 15 GeV) to the maximum 250 GeV in the main linacs with the average accelerating gradient 31.5 MV/m. The electron and positron linacs are respectively composed by 7332 and 7228 nine-cell SCRF accelerating cavities which operate at the frequency 1.3 GHz. Because approximately 3 GeV of extra energy is required in the electron linac to compensate for positron production, the required number of cavities is a bit more than for the positron linac. The accelerating cavities are assembled by SCRF crymodules each of which contains 26 cavities.

- The **beam delivery system** transports the beams from the main linacs to the collision region. It is responsible for focusing the beam to the sizes which are needed for the luminosity goals, measuring and monitoring the key physics parameters such as energy and polarization before and after the collisions. Also, the beam delivery system will protect the beamline and detector against mis-steered beams from the main linacs and bring the spent beams to the main beam dumps.
- The **detectors** will be located in the center of site. Two detectors ILD [3] and SiD [4] are proposed in the same interaction point (IP) using a push-pull mechanism. These two detectors will incorporate different but complementary technologies to capture information about every particles produced in each collision and offer the vital cross-checking of the potential physics discoveries. The design of ILD concept will be discussed in the following section of this chapter.

The electron and positron beams delivered to interacting point will be 5.0 Hz pulses. Each of the pulse will last for about 1 ms and is formed by about several thousands of bunches. The nominal beam parameter set is given in Table 1.1.

Table 1.1: The nominal beam parameters of ILC (values at 500 GeV centre of mass energy)

Parameter	Value	Unit
Centre of mass energy range	$200 - 500$	GeV
Peak luminosity	2×10^{34}	$\mathrm{cm}^{-2}\mathrm{s}^{-1}$
Average beam current in pulse	9.0	mA
Pulse rate	5.0	Hz
Number of bunches per pulse	$1000 - 5400$	
Charge per bunch	$1.6 - 3.2$	nC
Accelerating gradient	31.5	MV/m
RF pulse length	1.6	ms
Beam power (per beam)	10.8	MW
Typical beam size at IP ($h \times v$)	640×5.7	nm
Total AC Power consumption	230	MW

1.1.2 Required Energy and Luminosity

As seen in Table 1.1, the centre of mass energy of ILC will be adjustable from 200 to 500 GeV and upgradable to 1 TeV. Why is the energy chosen like this, why do we need such high luminosity? Some considerations which motivate these choices will be presented in this section.

- Currently, the most important and most urgent task for high energy physics community is to reveal the mask of Higgs Mechanism [8] which is responsible for the electroweak symmetry breaking in the **S**tandard **M**odel (SM). There are already some clues obtained mainly at LEP, SLC and Tevatron. First of all, from the direct searches done by the four experiments at LEP at the centre of mass energies up to 209 GeV, a lower bound of 114.4 GeV with 95% **C**onfidence **L**evel (CL) [9] for the SM Higgs mass was derived, and 17 candidate events found by the four experiments at around $115-116$ GeV were presented. From the recent results of CDF and D0, the region of $162-166$ GeV for Higgs mass was excluded at 95% CL by using the search mode $H \to W^+W^-$ [10]. Second, since quantum corrections to the mass of W boson and Z boson depend logarithmically on the Higgs mass and quadratically on the Top quark mass, a global fit [11] was carried out by using the combined precision electroweak measurements done at LEP, SLC and Tevatron. Some constraints for SM were obtained, one of which is concerned with the Higgs mass. The Higgs mass was fit to be $M(H) = 87^{+35}_{-26}$ GeV, and by using the lower limit from the direct search, a 95% CL upper bound of 186 GeV for the Higgs mass was derived. The result of global fit is shown in Figure 1.2. Finally, there are some other theoretical constraints on the Higgs mass [12, 13, 14, 15] where a light Higgs below 1 TeV is favored. If the Higgs mass is really in these regions, through the processes $e^+ + e^- \to HZ$, $e^+ + e^- \to ZHH$ and $e^+ + e^- \to t\bar{t}H$ where the required centre of mass energies could be covered at the ILC, the Higgs profiles could be precisely measured, for example the Higgs mass, width, spin, self couplings and top Yukawa coupling. These measurements will shed light on the nature of electroweak symmetry breaking.

- An additional consideration comes from the top quark pair threshold scan at around the energy 350 GeV, which could perform a 100 MeV precision for the top quark mass [16, 17, 18] measurment. The physics impact of the precision measurement of top quark mass is well explained in Ref.[19], which tells us that the top quark mass is essential for both SM and physics beyond SM.

- Another consideration comes from the possible situation that if no light Higgs was discovered at LHC. In this case, the W^+W^- scattering process will violate the unitarity [12] at round 1 TeV unless there are new physics beyond SM and new resonances. Then precision measurements at 1 TeV e^+e^- collider will have the capability to investigate these new physics and extract the contributions of these new resonances.

- Other considerations come from new physics beyond SM, like Super Symmetry (SUSY), extra dimension, Little Higgs and so on. These new physics also predict a light higgs or light new resonances, which could be covered at the energies 200 to 500 GeV and onwards to 1 TeV.

A consensus [20] about the energy region for ILC $200-500$ GeV at Phase I and 1 TeV at Phase II was established to reveal the Terascale physics.

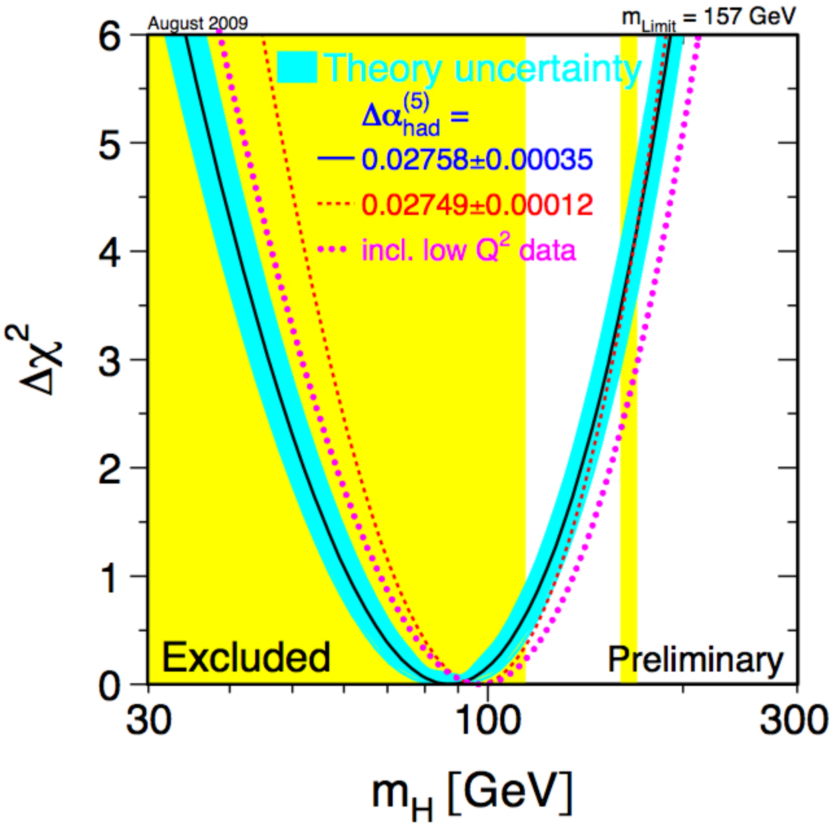

Figure 1.2: The direct and indirect constraints for Higgs mass, where the curves show the global fit result and vertical bands show the direct searches from LEP (left) and Tevatron (right).

Why is the luminosity required to be as high as 2×10^{34} cm^{-2}s^{-1}? First let's have a look at the quantities which could affect the luminosity. The luminosity is defined by

$$L = \frac{\nu N_1 N_2}{4\pi\sigma_x\sigma_y}$$

, where ν is the bunch collision frequency, N_1, N_2 are the numbers of electrons or positrons in the two bunches colliding to each other, σ_x, σ_y are the transverse widths of the bunches, corresponding respectively to the horizontal and vertical directions. High luminosity requires large N_1 and N_2, high bunch collision frequency, and small beam cross sectional area $\sigma_x\sigma_y$. A more useful quantity is the integrated luminosity which is defined by $\int Ldt$. The integrated luminosity in a year corresponding to the luminosity 2×10^{34} cm^{-2}s^{-1} is 200 fb^{-1}, counting effectively 10^7 seconds for a year. The required luminosity is dependent on the cross sections of the physics processes through which we can perform the designed measurements, and the precisions which are need to achieve. Different measurements need different luminosity. Figure 1.3 shows the cross sections of typical physics processes at ILC as a function of centre of mass energy [21]. Most of them fall like $1/s$ (characteristic of s-channel Feynman diagram), where s is the square of the centre of mass energy. As indicated by current simulation study [3], we need 250 fb^{-1} integrated luminosity to perform a 2.7% percent level measurement of the branching ratio of Higgs decaying into $b\bar{b}$. And if we want to measure the top quark mass to the precision 100 MeV, the required integrated luminosity should be as high as 500 fb^{-1}. We will see, from this study of Higgs Self-coupling, 2 ab^{-1} integrated luminosity would be needed for a 4 σ significance ZHH events excess. The design luminosity which is as high as 2×10^{34} cm^{-2}s^{-1} can make all these measurement possible at ILC.

1.1.3 Reasons for an e^+e^- Linear Collider

Comparing to the last generation lepton colliders LEP and SLC, and the now operating hadron colliders Tevatron and LHC, the reasons for ILC are quite clear:

- For a circular collider, the synchrotron radiation rises as $\frac{E^4}{Rm^4}$, where E is the beam energy, R is the radius and m is the mass of colliding particle. Hadron colliders like the Tevatron and LHC do not have severe synchrotron radiation issues due to that the mass of proton is 1800 times larger than the mass of electron. However, due to the small electron mass, LEP at 208 GeV was radiating 3% of the beam energy per turn. If we build a 500 GeV circular collider, without significantly increasing the radius, the synchrotron radiation would be so high that the running costs would be too expensive. That is the reason we chose a linear collider, which has no synchrotron radiation issues at all, since R = infinity.

- The centre of mass energy is well determined in case of a lepton collider. In a hadron collider such as LHC where the energy reach is much higher, the effective centre of mass is determined by $\sqrt{s} = \sqrt{2x_1x_2}E_{beam}$, where x_1, x_2 are the fractions of the partons energies which are not constant for every event, E_{beam} is the beam energy. Instead in a linear collider, the centre of mass

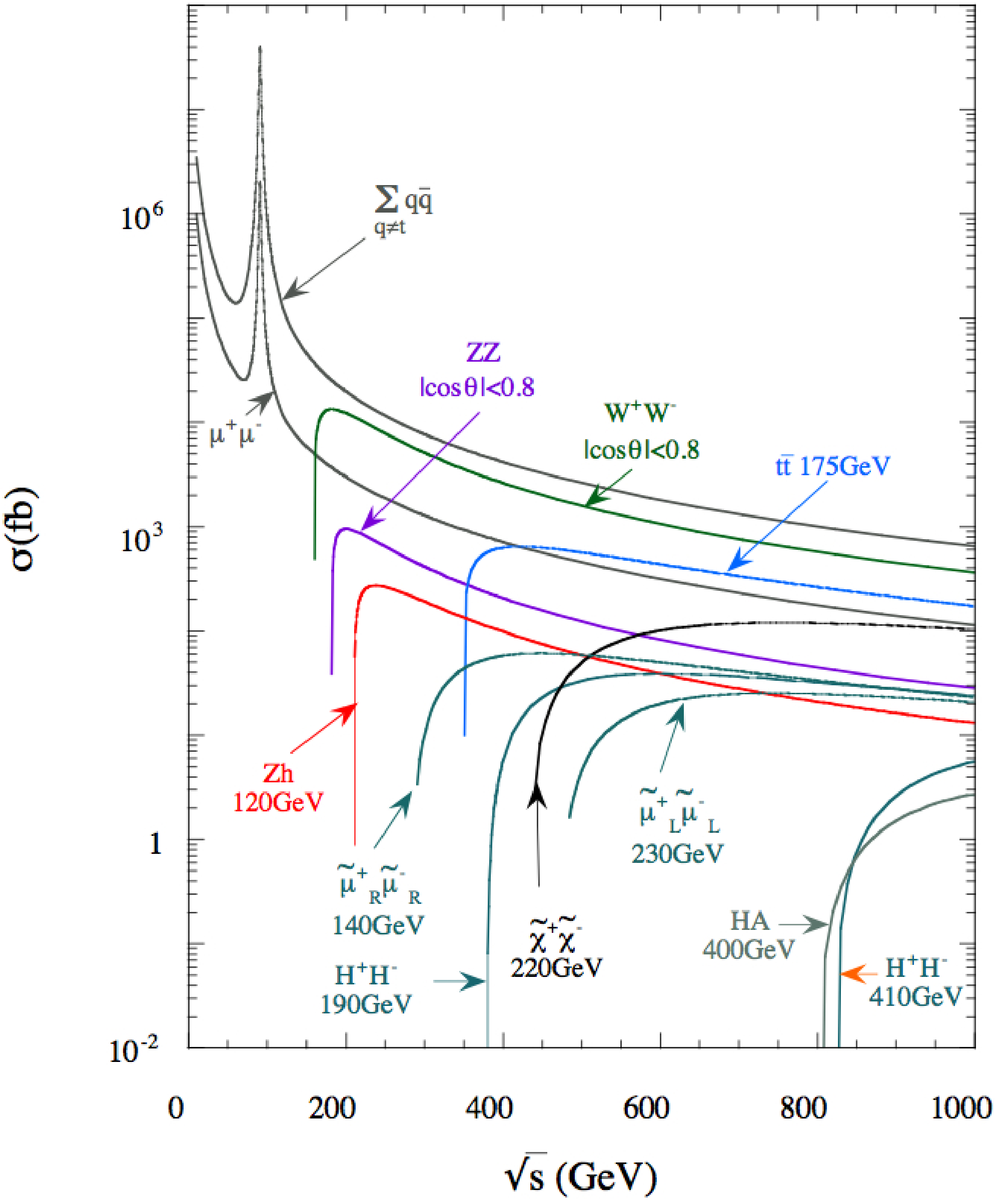

Figure 1.3: The cross sections for some real and possible processes at ILC energy region.

energy is determined by $\sqrt{s} = 2E_{beam}$, though there is a small correction due to the beamstrahlung. This feature makes the linear collider extremely suitable for the investigation of exotic phenomena, such as those demonstrated by the discovery of J/Ψ at SLAC [22] and precision measurements done at LEP. Meanwhile, this feature offers an excellent environment for the threshold physics, such as ZH threshold scan and $t\bar{t}$ threshold scan.

- The Standard Model background-event rates at the Linear Collider are relatively small, a feature which is often called 'cleanliness'. The electroweak processes at a hadron collider are smaller by nine orders of magnitude than the QCD hadronic background which is the dominant process at a hadron collider. At ILC the rates for signal and background differ by only two orders of magnitude: the environment is 'clean'.

- The polarization of electron can be adjustable. The baseline of ILC is capable of producing electron beams with polarization of at least 80%. This feature can be used to suppress the process such as W^+W^-, which usually is one of the main background processes, to 20% of non-porloarized case.

1.1.4 Options

The baseline of ILC will be a 500 GeV e^+e^- collider. But depending on the results of LHC and first stage of ILC, it is capable of several options:

- Without any big modification, the e^+e^- machine could be changed to a e^-e^- machine[23], by adding a electron gun at the positron beam end. Some super symmetry processes could benefit from this option [21].

- Using Compton scattering by an intense laser to the electron beam just a few millimeters before reaching the interact point, we can produce a high energy photon beam which is nearly following along the original direction of electron beam. Then the machine could be changed to a photon collider ($e^-\gamma$ or $\gamma\gamma$) based on the e^-e^- option. The physics potential for a photon collider has been widely discussed [24] and shown to be a good option for measuring the profile of Higgs boson.

- By running the machine at Z Pole or W pair threshold, called GigaZ, foresees the possibility of generating over 10^9 Z decays events and 10^6 W^+W^- scattering events, 100 times statistics larger then those collected on LEP, in less than one year. These events may help us to measure the standard model processes with a precise accuracy, which is crucial to offer the advancing test of standard model and the clues to any new physics beyond standard model.

1.2 The International Large Detector ILD

The interact region of ILC is designed to host two detectors, which can be moved into the beam position using a push-pull mechanism. Two detector concepts ILD [3] and SiD [4] have been validated to meet the physics requirements. In this section, an introduction to the basic layout of ILD, which all the studies in this thesis are based on, is presented. Also the designed performance will be covered.

1.2.1 Basic Layout of ILD

The proposed ILD concept, which is derived for the GLD [5] and the LDC [6] detector concepts, is designed as a general multi-purpose detector. It can provide excellent precision in spatial and energy measurement over a large solid angle. The detail performance and design philosophy are summarized in the ILD Letter of Intent(LoI) [3]. The ILD detector concept is shown schematically in Figure 1.4. The main components of ILD are the following [3]:

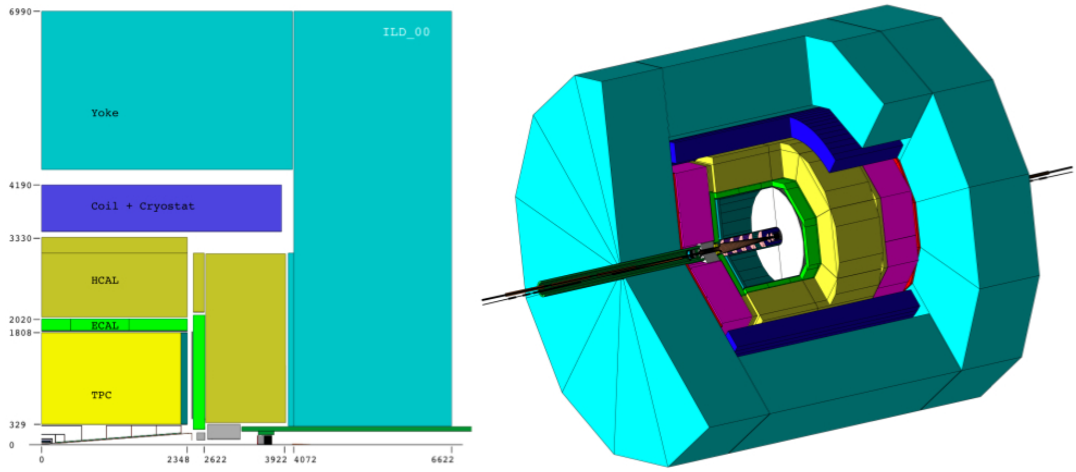

Figure 1.4: View of the ILD detector concept. From the inside to the outside, the detector components are: VTX, SIT, TPC, SET, ECAL, HCAL, Coil and Yoke. In the forward region, FTD, ETD, LCAL, LHCAL and BCAL are shown.

- Vertex Detector (VTX) is a multi-layer pixel-vertex detector to measure the precision vertex information. It is located in the inner most surrounding the beams, with three cylindrical super-layers each comprising two layers. All layers are equipped with arrays of pixel sensors. The pixel sensors are as thin as 50 μm, providing a very good single point resolution of 2.8 μm over all the sensitive VTX area. Once a particle with measurable life time decays in the VTX area, the charged tracks from this particle will generate hit responses while passing these layers. By using the hit information, we can reconstruct the displaced vertices, which are also called secondary vertices (the primary vertex is the interact point). These second vertices information are crucial for flavor tagging. The VTX also plays an important role in the track reconstruction, especially for low momentum particles which don't reach the main tracker or barely penetrate its sensitive volume because of the strong magnetic field of the experiment, or due to their shallow production angle. The VTX design is still evolving and there is another alternative option featuring 5 equidistant single layers. Figure 1.5 shows the two design options.

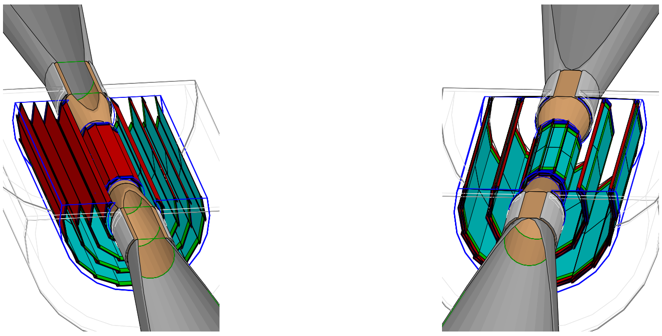

Figure 1.5: Vertex detector geometries of the two design options. Left: 5 single ladders (VTX-SL). Right: 3 double ladders (VTX-DL).

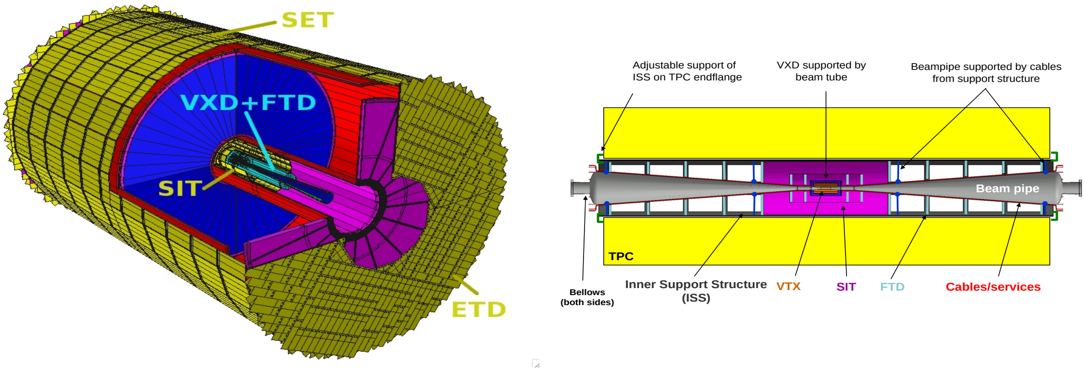

Figure 1.6: Schematic view of the tracking system and of the sillicon tracking components. The plot on the right shows a side-view of the inner silicon tracking system, including the support structure.

- Silicon Tracking System is made of two sets of detectors. The first set is located in the central barrel and is made of the Silicon Internal Tracker (SIT), between the VTX and TPC, and the Silicon External Tracker (SET), between the TPC and ECAL. The second set is located in the forward region and is constituted of the Forward Tracking Detector (FTD) in the very forward region, and the end cap Tracking Detector (ETD), providing a space point between the TPC endplate and the calorimeter in the end cap region. The Silicon Tracking System can give a very good track link between VTX and TPC, give a precise entry point to ECAL after TPC and extend the tracking coverage almost to 4π. Along with the VTX and TPC, the Silicon Tracking System can offer very good momentum resolution and tracking efficiency. Figure 1.6 shows the components of Silicon Tracking System.

- The Time Projection Chamber (TPC) is the central tracker to measure the momenta of charged particles, offering up to 224 space points per track. It is mainly constituted of the barrel field cage which provides the electric field along the axis direction, the gas in which the ionization signals are generated when

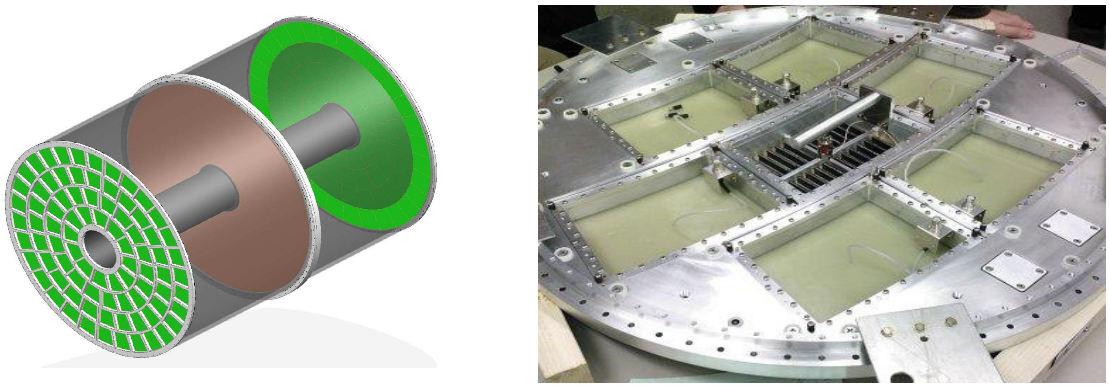

Figure 1.7: (left)Conceptual design of end plate for LCTPC. (right) View of the end cap subdivision as used for the Large Prototype.

charged particles pass through it, and the end plates which collect and amplify the electron signals drifted to it by the electric field. TPC presents a minimum amount of material, as required by the precision momentum measurement and the best calorimeter performance. The point resolution and the double-hit resolution, which are moderate when compared to silicon detectors, are compensated by continuous tracking. The TPC also provides dE/dx-based particle identification capabilities. Figure 1.7 illustrates a conceptual design, by the LCTPC collaboration [25] which is responsible for the design and for the R&D, of the end plate and shows the end plate subdivisions used for the Large Prototype.

- Electromagnetic Calorimeter (ECAL), outside of TPC and SET, is a sampling calorimeter to measure the energy of electrons and photons through electromagnetic showering, with tungsten as absorber layers and silicon or scintillator as active layers. It is constituted of the cylindrical barrel and two end caps. The usage of tungsten (radiation length X_0 = 3.5mm, Molière Radius $\mathrm{R_M}$ = 9mm and interaction length λ_I = 99mm) allows for a compact design with a depth for roughly $24X_0$ within 20cm. To achieve an adequate energy resolution, the ECAL is longitudinally segmented into around 30 layers and the active layers are segmented into cells with a lateral size of $5-10$mm to reach the required pattern recognition performance. Figure 1.8 shows the layout of ECAL and layout of one module.

- Hadron Calorimeter (HCAL), outside of ECAL, is a sampling calorimeter to measure the energy of hadrons such as π, K, n, p, etc... through hadronic showering, with steel as absorber and scintillator tiles (analogue HCAL) or gaseous devices (digital HCAL) as active medium. The overall structure of HCAL follows the "short barrel" concept, with two large end caps with about the same outer radius as the barrel. The iron, as absorption material, with its moderate ratio of hadronic interaction length (λ_I = 17cm) to electromagnetic radiation length (X_0 = 1.8cm) allows a fine longitudinal sampling in terms of X_0 with a reasonable number of layers in a given total hadronic absorption length, thus keeping the detector volume and readout channel count small.

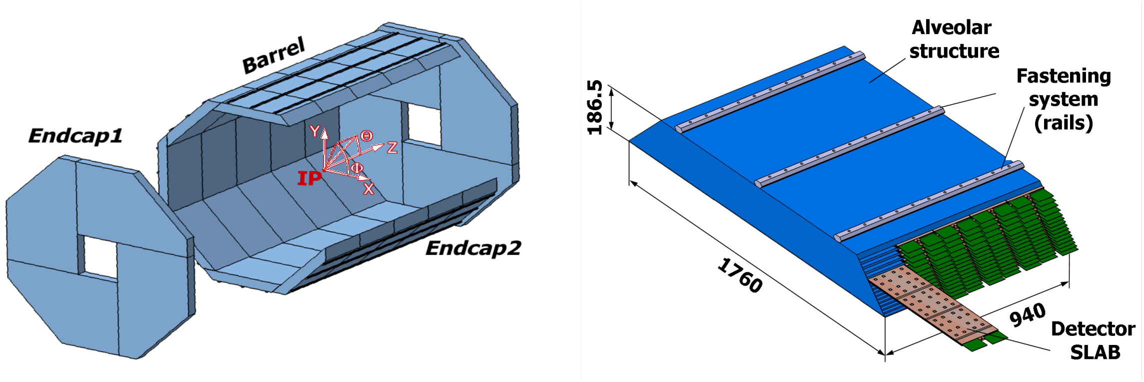

Figure 1.8: Global layout of the ECAL (left) and layout of one module (right).

The R&D of ECAL and HCAL is carried out by CALICE collaboration [26]. Figure 1.9 shows the layout of HCAL and layout of one module.

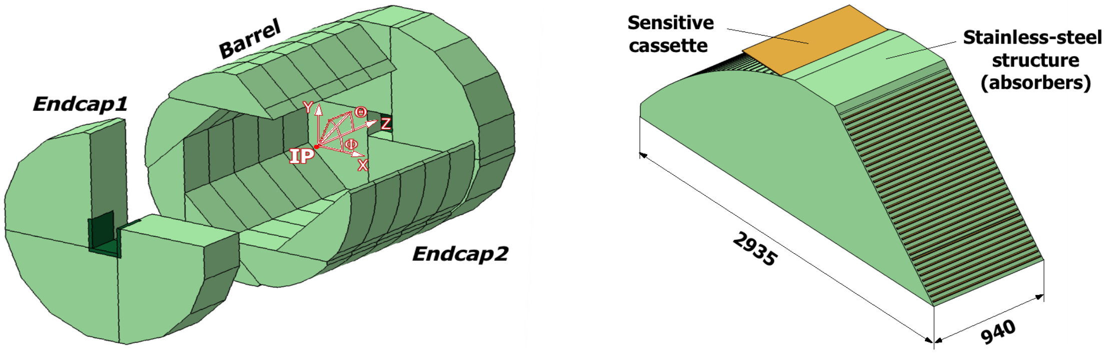

Figure 1.9: Layout of the HCAL (left) and layout of one module (right).

- Forward Detectors are a set of special detectors in the very forward regions: FTD, ETD, LumiCal, LHCal and BeamCal. FTD and ETD introduced in Silicon Tracking System are used for forward tracking. Luminosity Calorimeter (LumiCal) is a compact silicon-tungston sandwich electromagnetic calorimeter for the precise luminosity measurement by counting the Bhabha scattering events. LHCal is a hadron calorimeter extending the coverage of the HCAL endcaps to small polar angles. BeamCal is designed as a solid state sensor-tungsten sandwich electromagnetic calorimeter for detecting the electron-positron pairs originating from beamstrahlung, useful for bunch-by-bunch luminosity estimate and the determination of beam parameters.

- The coil and return yoke, located outside of HCAL consist of the superconducting solenoid and the iron yoke. The superconducting solenoid provides the 3.5T magnetic field parallel to the beam direction inside the magnet. The strong magnetic field is crucial for precise momentum measurement of charged particles, which not only has the benefit of large curvature but also of compressing the transverse diffusion of drifting electrons in TPC. It is also useful

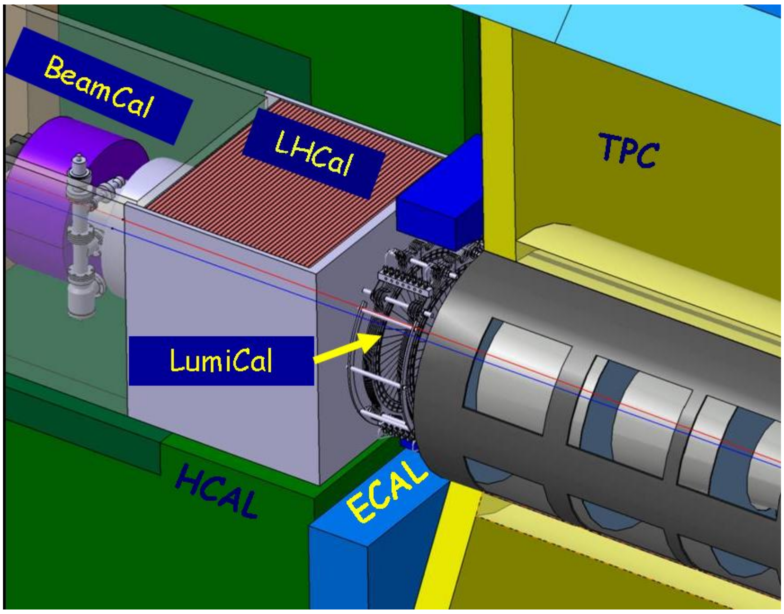

Figure 1.10: The very forward region of the ILD detector.

for the separation of clusters generated by nearby charged and neutral particles in calorimeters. The iron yoke, instrumented with scintillator strips or RPCs, returns the magnetic flux of the solenoid, and at the same time, serves as a muon filter, muon detector and tail catcher. Figure 1.11 shows the cross section of ILD magnet.

- Data Acquisition System (DAQ) is the system to process and store the data recorded by detectors. It has to fulfill the the needs of a high luminosity, high precision experiment, which can only be achieved by a substantially large number of readout channels. Details of DAQ system are presented in the LoI of ILD [3].

1.2.2 Performance of ILD

ILD detector concept can meet the requirements for an ILC detector [3]:

- **Track reconstruction:** The ILD tracking system provides highly efficiency track reconstruction ($\sim 99.5\,\%$), even in a dense multi-jet environment.
- **Momentum resolution:** When hits in the TPC are combined with those in Si tracking detectors, the asymptotic value of the momentum resolution is $\sigma_{1/p_T} \approx 2 \times 10^{-5}\,\mathrm{GeV}^{-1}$, as required.
- **Impact parameter resolution:** For either option for the VTX layout, the required impact parameter resolution is achieved, with asymptotic values of $\sigma_{r\phi} = 2\,\mu$m and $\sigma_{rz} = 5\,\mu$m.
- **Particle flow performance:** A jet energy resolution of $< 3.8\,\%$ is achieved for jets in the energy range $40 - 400\,$GeV. For the range of energies typical of

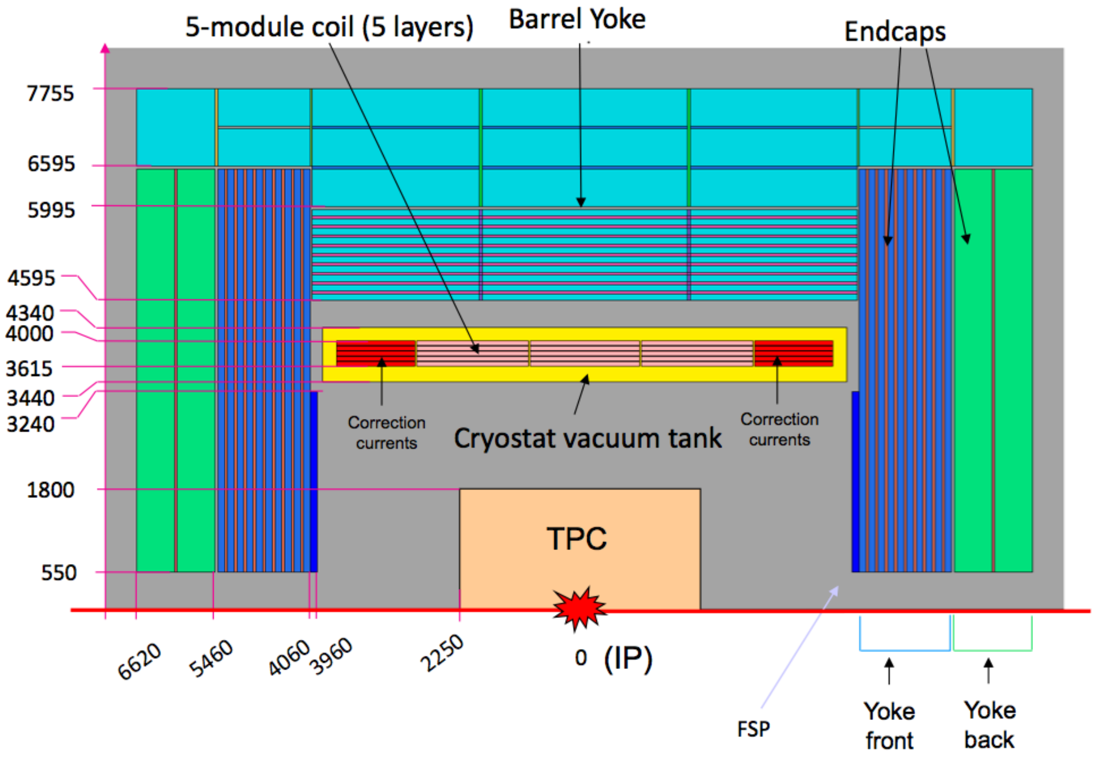

Figure 1.11: Cross section of the ILD magnet.

much of the ILC physics, 80 − 200 GeV the jet energy resolutions is ≈3 %. The performance does not depend strongly on the polar angle of the jet, except in the very forward region.

Chapter 2

Electroweak Standard Model and Higgs Self-Couplings

In the past more than 2000 years, people never stop thinking about "what are the basic constitutes of our universe, how do they constitute the very different kinds of matter?". We've been very impressed by the Atomic Theory of Democritus, the famous ancient Greek philosopher, and the Theory of Five Elements in ancient China. In the modern science, the knowledge of these questions are well represented by the Dalton's Atomic Theory and Mendeleev's Periodic Table of Elements. Then from about one century ago, people become more and more close to the answer of elementary particles and their fundamental interactions, from the discovery of electron by J. J. Tomoson in 1897 to the discovery of top quark by Fermi Lab in 1995. The proposed ILC is exactly on the road to quest the ultimate answers.

In this chapter, a brief introduction to the Standard Model (SM) of the electroweak interaction and to the Higgs mechanism of electroweak symmetry breaking will be presented. Then the motivation of Higgs self-coupling study and the experimental approach to measure the Higgs self-coupling at the future International Linear Collider are discussed. In the final section, the structure of this thesis is given.

2.1 Standard Model

The Standard Model of strong and electroweak interactions is so far the most successful theory of elementary particles [27] [28], established between the late 60s and early 70s of last century. In the SM, there are three generations of leptons $(e, \mu, \tau, \nu_e, \nu_\mu, \nu_\tau)$ and quarks (u, d, c, s, t, b), to constitute all of the matter, four gauge bosons (γ, W, Z, g), to mediate the strong and electroweak interactions, and one scalar particle (Higgs), to break the electroweak symmetry and give masses to all of the elementary particles. The SM of strong interactions, known as Quantum Chromodynamics (QCD) [27], is a $\mathrm{SU(3)_C}$ gauge theory of colors of quarks. And the SM of electroweak interactions, known as Glashow-Weinberg-Salam Model [28], is a $\mathrm{SU(2)_L \times U(1)_Y}$ gauge theory of weak left-handed isospin and hypercharge of quarks and leptons. Detailed discussions of the SM could be found in the report [29] and in the review [30], and in the references therein.

2.1.1 Electroweak SM

The electroweak standard model is based on the gauge group $\mathrm{SU(2)_L} \times \mathrm{U(1)_Y}$, with the gauge fields W_μ^a, $a = 1, 2, 3$, and B_μ for the $\mathrm{SU(2)_L}$ and $\mathrm{U(1)_Y}$ factors, respectively, and the corresponding generators are T^a, $a = 1, 2, 3$ and Y.

$$T^a = \frac{1}{2}\tau^a; \quad \tau_1 = \begin{pmatrix} 0 & 1 \\ 1 & 0 \end{pmatrix}, \ \tau_2 = \begin{pmatrix} 0 & -i \\ i & 0 \end{pmatrix}, \ \tau_3 = \begin{pmatrix} 1 & 0 \\ 0 & -1 \end{pmatrix} \tag{2.1}$$

The gauge coupling constants for $\mathrm{SU(2)_L}$ and $\mathrm{U(1)_Y}$ are g and g'. The left-handed fermion fields of the i^{th} generation fermion transforms as doublet $L_i = \begin{pmatrix} \nu_i \\ l_i^- \end{pmatrix}$ for leptons and $Q_i = \begin{pmatrix} u_i \\ d_i' \end{pmatrix}$ for quarks under $\mathrm{SU(2)_L}$, where $d_i' \equiv \sum_j V_{ij} d_j$, and V is the Cabibbo-Kobayashi-Maskawa mixing matrix [31]. The right handed fermion fields are $\mathrm{SU(2)_L}$ singlets, e_{Ri} for lepton, and u_{Ri}, d_{Ri} for up and down type quarks. Before spontaneous symmetry breaking, the Lagrangian for electroweak SM is

$$\begin{aligned} \mathscr{L} \ &= \ -\frac{1}{4}W_{\mu\nu}^a W_a^{\mu\nu} - \frac{1}{4}B_{\mu\nu}B^{\mu\nu} \\ &\quad + \bar{L}_i i D_\mu \gamma^\mu L_i + \bar{e}_{Ri} i D_\mu \gamma^\mu e_{Ri} \\ &\quad + \bar{Q}_i i D_\mu \gamma^\mu Q_i + \bar{u}_{Ri} i D_\mu \gamma^\mu u_{Ri} + \bar{d}_{Ri} i D_\mu \gamma^\mu d_{Ri} \end{aligned} \tag{2.2}$$

where the covariant derivative D_μ is defined by

$$D_\mu = \partial_\mu - i(g T_a W_\mu^a + g' \frac{Y}{2} B_\mu) \tag{2.3}$$

and $W_{\mu\nu}^a$, $B_{\mu\nu}$ are defined by

$$W_{\mu\nu}^a = \partial_\mu W_\nu^a - \partial_\nu W_\mu^a - g\epsilon^{abc} W_\mu^b W_\nu^c \tag{2.4}$$

$$B_{\mu\nu} = \partial_\mu B_\nu - \partial_\nu B_\mu \tag{2.5}$$

This Lagrangian is invariant under the local gauge transformation for fermion fields and gauge boson fields:

$$\begin{cases} L(x) \to L'(x) = e^{i\alpha_a(x)T^a + i\beta(x)Y} L(x) \\ R(x) \to R'(x) = e^{i\beta(x)Y} R(x) \\ \vec{W}_\mu(x) \to \vec{W}_\mu(x) - \frac{1}{g}\partial_\mu \vec{\alpha}(x) - \vec{\alpha}(x) \times \vec{W}_\mu(x) \\ B_\mu(x) \to B_\mu(x) - \frac{1}{g'}\partial_\mu \beta(x) \end{cases} \tag{2.6}$$

The interaction between fermions and gauge bosons is specified by the minimal coupling item in Eqn. 2.2

$$\mathscr{L}_I = \bar{\psi}_f i D_\mu \gamma^\mu \psi_f, \tag{2.7}$$

here ψ_f represents fermion field.

Because the gauge boson mass term $\frac{1}{2}M_V^2 W_\mu W^\mu$ and fermion mass term $-m_f \bar{\psi}_f \psi_f$, which are not invariant under the gauge transformation in Eqn. 2.6, will violate the local $\mathrm{SU(2)_L} \times \mathrm{U(1)_Y}$ gauge symmetry, up to now we have to keep all the gauge boson fields and fermion fields massless. However, from the fact that the weak interaction is a very short distance interaction, the mediated gauge boson should be very heavy; this is just the opposite of the case for the electromagnetic interaction, which is a long distance interaction with the mediated gauge boson being the massless photon. And experimentally we indeed measured the masses of fermions and gauge bosons. So there should be some mechanism to break the $\mathrm{SU(2)_L \times U(1)_Y}$ gauge symmetry and give masses to the fermion fields and gauge boson fields.

2.1.2 The Higgs Mechanism and Electroweak Symmetry Breaking

The simplest choice for this breaking is to use the so-called Higgs mechanism, where the $\mathrm{SU(2)_L \times U(1)_Y}$ electroweak gauge symmetry is spontaneously broken by introducing a complex $\mathrm{SU(2)_L}$ doublet of scalar field Φ

$$\Phi = \begin{pmatrix} \phi^+ \\ \phi^0 \end{pmatrix} \tag{2.8}$$

with hypercharge $Y_\phi = +1$. Then we need to add the scalar field part to the electroweak SM Lagrangian (Eqn. 2.2)

$$\mathscr{L}_\Phi = (\mathrm{D}^\mu \Phi)^\dagger (\mathrm{D}_\mu \Phi) - \mu^2 \Phi^\dagger \Phi - \lambda (\Phi^\dagger \Phi)^2 \tag{2.9}$$

which is invariant under the locale gauge transformation in Eqn. 2.6. The first term of Eqn. 2.9 is kinetic, and the potential part is

$$V(\Phi) = \mu^2 \Phi^\dagger \Phi + \lambda (\Phi^\dagger \Phi)^2 \tag{2.10}$$

Here, $\lambda > 0$ is required to make potential bounded from below. If $\mu^2 > 0$, the potential has a minimum at $< 0|\Phi^\dagger\Phi| >= 0$, leading to a vacuum state which is still symmetric and which will not break the electroweak symmetry. In turn, if $\mu^2 < 0$, the potential has a minimum at

$$< \Phi^\dagger \Phi >_0 \equiv < 0|\Phi^\dagger \Phi|0 > = \frac{-\mu^2}{2\lambda} \tag{2.11}$$

Though this constraint for vacuum is $\mathrm{SU(2)_L \times U(1)_Y}$ symmetric, once one vacuum state is chosen, the Lagrangian 2.2 is not symmetric anymore. This is called spontaneous symmetry breaking. After the breaking the neutral part of scalar field Φ obtains a non vanishing vacuum expectation (we need still keep charged part having no vacuum expectation to preserve the $U(1)_Q$ symmetry of electromagnetic interaction)

$$< \Phi >_0 \equiv < 0|\Phi|0 > = \begin{pmatrix} 0 \\ \frac{v}{\sqrt{2}} \end{pmatrix}, \quad \text{with } v = \sqrt{\frac{-\mu^2}{\lambda}} \tag{2.12}$$

By choosing the unitary gauge, we can write the scalar field

$$\Phi = \frac{1}{\sqrt{2}} \begin{pmatrix} 0 \\ v + H(x) \end{pmatrix} \tag{2.13}$$

The $H(x)$ is called Higgs field.

We will see that, by introducing this scalar field to the kinetic term of Eqn. 2.9, the gauge boson will obtain mass. From Eqn. 2.3

$$\begin{aligned} \mathrm{D}_\mu\Phi &= (\partial_\mu - igT_aW^a_\mu - g'\frac{Y}{2}B_\mu)\Phi \qquad (2.14)\\ &= \frac{1}{\sqrt{2}}\begin{pmatrix} \partial_\mu - \frac{i}{2}(gW^3_\mu + g'B_\mu) & -\frac{ig}{2}(W^1_\mu - iW^2_\mu) \\ -\frac{ig}{2}(W^1_\mu + iW^2_\mu) & \partial_\mu + \frac{i}{2}(gW^3_\mu - g'B_\mu) \end{pmatrix}\begin{pmatrix} 0 \\ v+H(x) \end{pmatrix} \end{aligned}$$

then

$$\begin{aligned} (\mathrm{D}^\mu\Phi)^\dagger(\mathrm{D}_\mu\Phi) &= \frac{1}{2}(\partial_\mu H)^2 \qquad (2.15)\\ &\quad +\frac{g^2}{8}(v+H)^2|W^1_\mu - iW^2_\mu|^2 + \frac{1}{8}(v+H)^2|gW^3_\mu - g'B_\mu|^2. \end{aligned}$$

define the new fields $W^\pm_\mu$, Z_μ and A_μ

$$W^\pm_\mu = \frac{W^1_\mu \mp W^2_\mu}{\sqrt{2}}, \quad Z_\mu = \frac{gW^3_\mu - g'B_\mu}{\sqrt{g^2+g'^2}}, \quad A_\mu = \frac{gW^3_\mu + g'B_\mu}{\sqrt{g^2+g'^2}} \qquad (2.16)$$

there are terms in Eqn. 2.15

$$\frac{g^2v^2}{4}W^+_\mu W^{-\mu}, \quad \frac{1}{8}v^2(g^2+g'^2)Z_\mu Z^\mu \qquad (2.17)$$

where W and Z have acquired masses, leaving A massless.

$$M_W = \frac{1}{2}gv, \quad M_Z = \frac{1}{2}v\sqrt{g^2+g'^2}, \quad M_A = 0. \qquad (2.18)$$

By introducing the scalar field to the potential Eqn. 2.10,

$$\begin{aligned} V(\Phi) &= \mu^2\Phi^\dagger\Phi + \lambda(\Phi^\dagger\Phi)^2 \qquad (2.19)\\ &= \frac{1}{2}\mu^2(V+H)^2 + \frac{1}{4}\lambda(v+H)^4 \\ &= \lambda v^2H^2 + \lambda vH^3 + \frac{\lambda}{4}H^4 - \frac{\lambda v^4}{4} \end{aligned}$$

A scalar particle Higgs (H) is predicted, with mass $M_H^2 = 2\lambda v^2 = -2\mu^2$. The generation of fermion masses can be achieved by introducing the $\mathrm{SU(2)_L \times U(1)_Y}$ invariant Yukawa Lagragian

$$\mathscr{L}_F = -\sum_i \lambda_{ei}\bar{L}_i\Phi e_{Ri} - \sum_i \lambda_{di}\bar{Q}_i\Phi d_{Ri} - \sum_i \lambda_{ui}\bar{Q}_i\tilde{\Phi}u_{Ri} + h.c. \qquad (2.20)$$

where $\tilde{\Phi} = i\tau_2\Phi^*$ and λ_{ei}, λ_{ui}, λ_{di} are Yukawa couplings respectively to leptons, up- and down-type quarks. Take the electron part as example

$$\begin{aligned} \mathscr{L}_F &= -\lambda_e\bar{L}\Phi e_R + h.c. \qquad (2.21)\\ &= -\frac{\lambda_e}{\sqrt{2}}(\bar{\nu}_e \ \ \bar{e}_L)\begin{pmatrix} 0 \\ v+H(x) \end{pmatrix} e_R + h.c. \\ &= -\frac{\lambda_e}{\sqrt{2}}(v+H)\bar{e}_L e_R + h.c. \end{aligned}$$

And we know for fermion mass term

$$\begin{aligned} m\bar{\phi}_f\phi_f &= m\bar{\phi}_f(\frac{1-\gamma^5}{2}+\frac{1+\gamma^5}{2})\phi_f && (2.22)\\ &= m\bar{\phi}_R\phi_L+m\bar{\phi}_L\phi_R && (2.23)\end{aligned}$$

So in the Lagragian Eqn. 2.21, the electron has acquired the mass $m_e = \frac{\lambda_e v}{\sqrt{2}}$. In the same way, quarks acquired the masses $m_u = \frac{\lambda_u v}{\sqrt{2}}$, $m_d = \frac{\lambda_d v}{\sqrt{2}}$.

The Higgs filed vacuum expectation value v is precisely determined through the measurement of μ lifetime $\mu^- \to e^-\bar{\nu}_e\nu_\mu$, which is a weak decay process, mediated by W boson. The mass of the W boson can be determinde from the Fermi constant G_μ [32] measured in this process

$$M_W = (\frac{\sqrt{2}g^2}{8G_\mu})^{1/2}. \tag{2.24}$$

On the other hand, the W boson mass is related to the Higgs field vacuum expectation value v from Eqn. 2.17, then we can extract the v

$$v = \frac{1}{(\sqrt{2}G_\mu)^{1/2}} \approx 246\text{GeV} \tag{2.25}$$

Up to now, by introducing the Higgs Mechanism, gauge bosons W, Z and all fermions have acquired masses. The electroweak $\mathrm{SU(2)_L \times U(1)_Y}$ gauge symmetry is broken to $\mathrm{U(1)_Q}$ gauge symmetry of electromagnetic interaction with conserved charged $Q = T_3 + \frac{Y}{2}$. Under the unitary gauge, the three goldstone bosons generated in the spontaneous breaking are has been replaced by the physical bosons $W^\pm$, Z as longitudinal polarization degree of freedom. No additional particles are introduced except one scalar particle Higgs, which is the untested part in SM. For the end of this section, parts of the Lagrangian of electroweak SM after spontaneous symmetry breaking are given.

- For the fermion fields, including the interactions with gauge bosons and Higgs

$$\begin{aligned}\mathscr{L}_F &= \sum_i \bar{\psi}_i(\gamma^\mu\partial_\mu - m_i - \frac{gm_iH}{2M_W})\psi_i && (2.26)\\ &-\frac{g}{2\sqrt{2}}\sum_i \bar{\psi}_i\gamma^\mu(1-\gamma^5)(T^+W_\mu^+ + T^-W_\mu^-)\psi_i\\ &-e\sum_i q_i\bar{\psi}_i\gamma^\mu\psi_i A_\mu\\ &-\frac{g}{2cos\theta_W}\sum_i \bar{\psi}_i\gamma^\mu(g_V^i - g_A^i\gamma^5)\psi_i Z_\mu\end{aligned}$$

where $\theta_W \equiv tan^{-1}\frac{g'}{g}$ is the Weinberg angle, $T^\pm$ are the weak isospin raising and lowering operators, $e = \sin\theta_W$ is the positron electric charge, and the g_V^i, g_A^i are vector and axial vector couplings

$$\begin{aligned} g_V^i &= t_{3L}(i) - 2q_i\sin\theta_W && (2.27)\\ g_A^i &= t_{3L}(i) && (2.28)\end{aligned}$$

where $t_{3L}(i)$ is the weak isospin of ϕ_i ($+\frac{1}{2}$ for u_i and ν_i, $-\frac{1}{2}$ for d_i and e_i), q_i is charge of ϕ_i in units of e.

- For the Higgs field, and the couplings to fermions and gauge bosons

$$\begin{aligned}\mathscr{L}_H &= \frac{1}{2}(\partial_\mu H)^2 - \frac{1}{2}M_H^2 H^2 - \lambda v H^3 - \frac{\lambda}{4}H^4 \\ &\quad -\sum_i \frac{g m_i}{2M_W} H\bar{\psi}_i\psi_i \\ &\quad +\frac{g^2 v}{2} H W_\mu^+ W^{-\mu} + \frac{(g^2+g'^2)v}{4} H Z_\mu Z^\mu \\ &\quad +\frac{g^2v^2}{4} H^2 W_\mu^+ W^{-\mu} + \frac{(g^2+g'^2)v^2}{8} H^2 Z_\mu Z^\mu.\end{aligned} \tag{2.29}$$

- For the gauge bosons

$$\begin{aligned}\mathscr{L}_B &= M_W W_\mu^+ W^{-\mu} + \frac{1}{2} Z^\mu Z_\mu \\ &\quad + \text{kinetic terms of gauge fields} \\ &\quad + \text{trilinear interactions terms involving } AW^+W^-, ZW^+W^- \\ &\quad + \text{quadrilinear interactions terms involving } AAW^+W^-, \\ &\qquad AZW^+W^-, ZZW^+W^-, W^+W^-W^+W^-.\end{aligned} \tag{2.30}$$

2.2 Higgs Self-Couplings

There are two pillars in Standard Model, one is the gauge symmetry and the other is symmetry breaking and mass generation. The first pillar is well established by the precision measurements done at SLC, LEP and Tevatron in the last decade of last century. However, the second pillar is still untested. The running accelerators Tevatron and LHC would give some clues to this pillar. But they are not enough to fully understand the nature of electroweak symmetry breaking, to achieve which we need measure the precise profiles of Higgs boson once it is discovered. Among these profiles, we are especially interested in:

- the precise Higgs mass, width and spin,
- the Yukawa couplings of Higgs to different fermions, especially top Yukawa coupling,
- the couplings between Higgs and gauge bosons,
- the Higgs self-couplings,
- the CP property of Higgs.

The capabilities of LHC and ILC in covering these profiles will be completely complementary summarized in the report by LHC/LC study group [33]. One aspect of these profiles, the Higgs self-coupling, is the topic of this thesis. In this section, we will give an introduction to the Higgs self-coupling in the SM, then follow by the experimental approach of Higgs self-coupling measurement at LHC and ILC.

2.2.1 Higgs Potential in SM

As introduced in the previous section, the Higgs Potential is given as part of the SM Lagrangian in Eqn. 2.29

$$V(H) = \frac{1}{2}M_H H^2 + \lambda v H^3 + \frac{1}{4}\tilde{\lambda} H^4 \tag{2.31}$$

where H is the physical Higgs field and in the SM we have $\lambda = \tilde{\lambda} = \frac{M_H^2}{2v^2}$, which could be different in other models. Measuring the shape of Higgs potential is a decisive demonstration of Higgs Mechanism, which is responsible for the electroweak symmetry breaking. There are three terms in the Higgs potential, the first is Higgs mass term; the second term is a trilinear Higgs self interaction; the third term is a quartic Higgs self interaction. Considering that all the interactions discovered up to now are gauge interactions, the second and third terms predict non-gauge interactions, which would be a completely new type of interaction. To fully understand the shape of Higgs potential, we need to measure these three terms respectively. The mass term is possible to first be measured at LHC and then precisely determined at ILC. The quartic Higgs self-coupling turns out to very difficult to be measured at both LHC and ILC due to the very small cross section of three Higgs bosons production (less than 0.001 fb). So it becomes very important to investigate the possibilities of measuring the trilinear Higgs self-coupling.

On the other hand, the Higgs Mechanism in the Standard Model is the simplest choice achieving the spontaneous symmetry breaking. There exist several extended Higgs theories, such as the Two Higgs Doublet Model (THDM), or the Minimal Supersymmetric extension of Standard Model (MSSM). However, the trilinear Higgs self-coupling in these models could be very different [34]. A large deviation in the trilinear Higgs self-coupling from the SM value can be a common feature of the Higgs sector with the strong first order electroweak phase transition [35], which is required for a successful scenario of electroweak baryogenesis [36]. Therefore, the measurement of the trilinear Higgs self-coupling at collider experiments can be an important probe into such a cosmological scenario. The oneloop contributions to the trilinear Higgs self-coupling can also be very large in the model with sequential fourth generation fermions [37]. Thus the precision measurement of trilinear Higgs self-coupling could directly reveal the nature of extend Higgs sector.

At LHC, the possibilities of measuring Higgs self-couplings have been studied in several papers [38]. Recalling the conclusion, for the Higgs mass > 140 GeV, W^+W^- being the main decay mode of the Higgs, it is possible to measure the trilinear Higgs self-coupling to the precision of 30% taking advantage of the semi-leptonic decay of the W. However, for a light Higgs of mass below 140 GeV, Higgs mainly decays into $b\bar{b}$, it is impossible to make a sensible trilinear Higgs self-coupling measurement with the huge background from QCD processes at LHC.

2.2.2 Measuring the Higgs self-coupling at ILC

At ILC, benefitting from the much cleaner background, it would be possible to measure the Higgs self-coupling, for a light Higgs, to a sensitive level assuming a reasonable integrated luminosity. The measurement of trilinear Higgs self-coupling can be carried out at ILC through two leading processes: double Higgs-strahlung process $e^+ + e^- \to$ ZHH [39] and WW fusion process $e^+ + e^- \to \nu\bar{\nu}$HH [40], which are shown in Figure 2.2 and Figure 2.3. The former is expected to be dominant around the center of mass energy of 500 GeV and the latter to take over at higher energy. Figure 2.1 shows the cross sections of these two processes as a function of the center of mass energy. However, in both cases, as shown in Figure 2.2 and Figure 2.3, there exist the irreducible Feynman diagrams which have the same final-state particles which don't contain the Higgs self-coupling. The interferences between the interested Higgs self-coupling related diagrams and these irreduciable diagrams make the measurement of Higgs self-coupling more complicated. The cross sections of $e^+ + e^- \to$ ZHH and $e^+ + e^- \to \nu\bar{\nu}$HH as a function of the Higgs self-coupling, can be formulated as $\sigma = a\lambda^2 + b\lambda + c$, where constant a comes from the contribution of Higgs self-coupling diagram, c comes from the contribution of the irreducible diagrams, b comes from the contribution of the interference between them, σ is the cross section and λ is the Higgs self-coupling. These functions are shown in Figure 2.4 assuming the Higgs mass of $M_H = 120$ GeV. At the value of standard model Higgs self-coupling, its precision is determined to be 1.8 times of the precision of $e^+ + e^- \to$ ZHH cross section at 500 GeV,

$$\frac{\delta\lambda}{\lambda} = 1.8\frac{\delta\sigma}{\sigma}. \tag{2.32}$$

The factor will be 0.85 in case of $e^+ + e^- \to \nu\bar{\nu}$HH at 1 TeV,

$$\frac{\delta\lambda}{\lambda} = 0.85\frac{\delta\sigma}{\sigma}. \tag{2.33}$$

In this thesis, we focus on the double Higgs-strahlung process $e^+ + e^- \to$ ZHH at the center of mass energy of $\sqrt{s} = 500$ GeV and WW fusion process $e^+ + e^- \to \nu\bar{\nu}$HH at $\sqrt{s} = 1$ TeV assuming the Higgs mass of $M_H = 120$ GeV and the integrated luminosity 2 ab^{-1}. For $e^+ + e^- \to$ ZHH , depending on the different decay modes of Z and H, which are shown in Figure 2.5, there are several methods to identify the signal ZHH events. Table 2.2.2 shows several most promising combinations of decay modes for $e^+ + e^- \to$ ZHH and their branching ratios. The full simulation of the first three search modes are covered in chapters 4 – 6. Chapter 7 gives the combined result of the full simulation. For $e^+ + e^- \to \nu\bar{\nu}$HH , there are two most promising search modes. One is when both Higgs decay into $b\bar{b}$, the other is when one Higgs decays into $b\bar{b}$ and the other decays into WW^*. The fast simulation of former is covered in chapter 8. Brief conclusions are presented in Chapter 9.

Table 2.1: Most promising modes for $e^+ + e^- \to$ ZHH

Decay Mode	$Z \to$	$H_1 \to$	$H_2 \to$	Branching Ratio
1	ll	$b\bar{b}$	$b\bar{b}$	3%
2	$\nu\bar{\nu}$	$b\bar{b}$	$b\bar{b}$	9%
3	$q\bar{q}$	$b\bar{b}$	$b\bar{b}$	31%
4	$q\bar{q}$	$b\bar{b}$	WW^*	13%

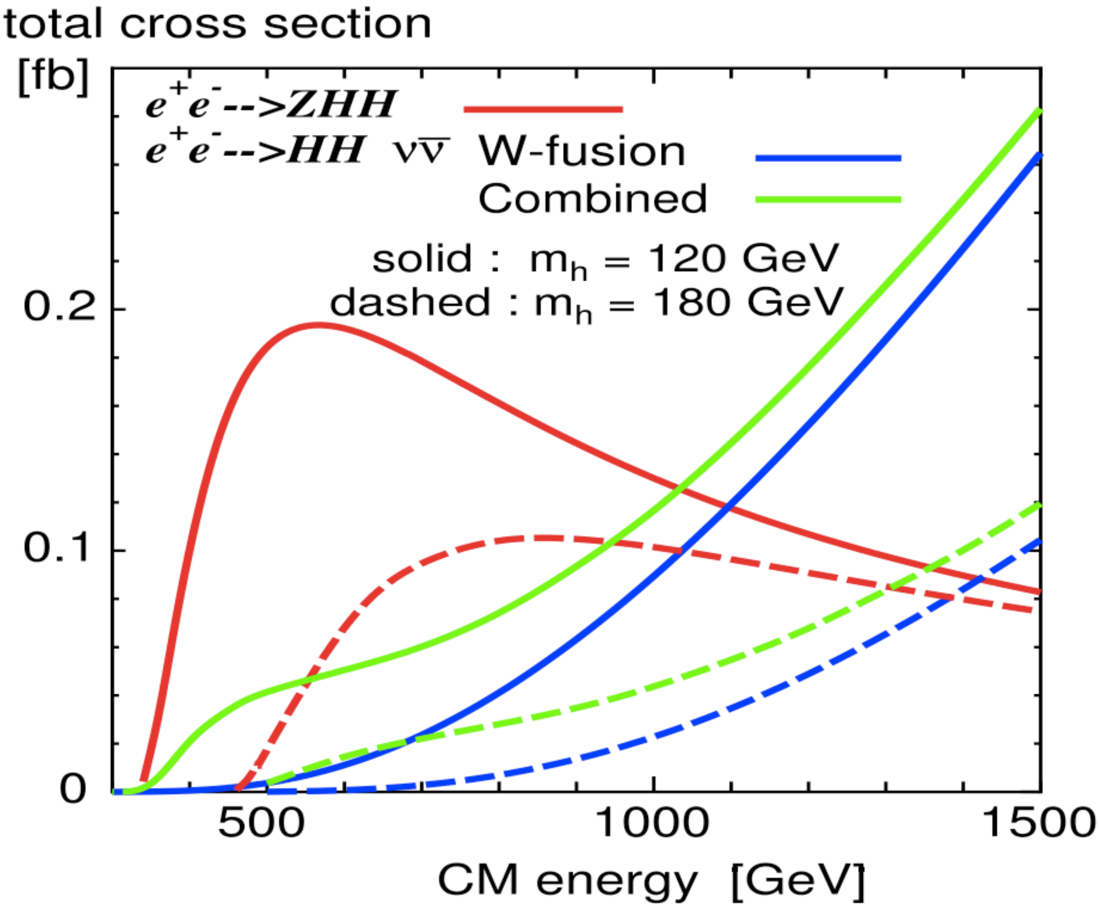

Figure 2.1: The separate and combined production cross sections for the ZHH and $\nu\bar{\nu}$HH processes as a function of the center of mass energy [41]. The red line is for the ZHH process, the blue line is for the $\nu\bar{\nu}$HH fusion process and the green line is for the combined result. The solid line is for the Higgs mass of 120 GeV and the dashed line is for 180 GeV.

2.2.3 Previous Simulation Studies of the Higgs Self-coupling Measurement at the e^+e^- Linear Collider

There are several simulation studies performed on ZHH channel [43] [44] [45][46] and $\nu\nu$HH channel [47]. The analyses in these references have all used fast simulations except [45], which used full simulation based on the LDC detector concept. For the double Higgs strahlung process at 500 GeV, the analysis in [43] investigated both qqHH and llHH decay modes of ZHH and obtained a precision of 10% on the ZHH cross section and 18% on the Higgs self-coupling, assuming an integrated luminosity 2 ab^{-1}. The analysis in [44] studied the qqHH mode of ZHH and obtained about 32% precision on the Higgs self-coupling, assuming 2 ab^{-1}. However the error would double if the final state gluon radiation is considered. The analysis [45] is a more realistic simulation of the qqHH decay mode of ZHH, where much worse precision on the ZHH cross section was obtained, about 180% assuming integrated luminosity 500 fb^{-1}, corresponding to 90% for 2 ab^{-1}. For the WW fusion process at 1 TeV, analysis [47] obtained 12% precision on the Higgs self-coupling assuming 1 ab^{-1}

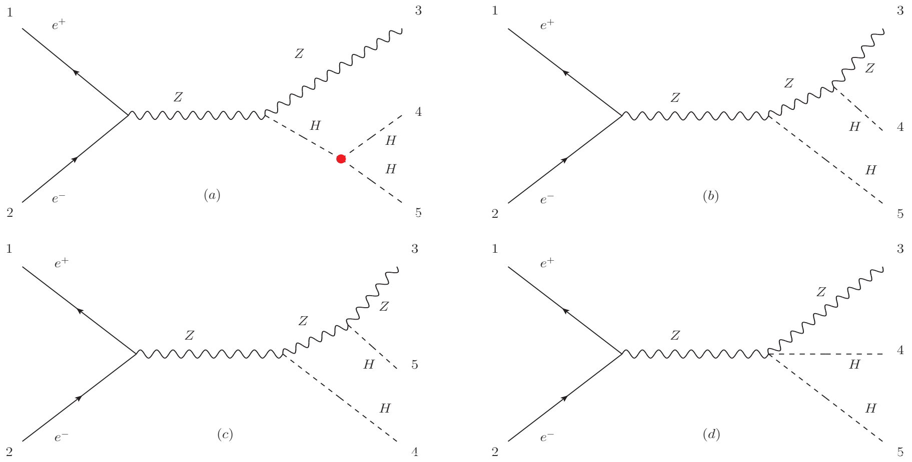

Figure 2.2: Feynman diagrams for double Higgs strahlung process $e^+ + e^- \rightarrow$ ZHH . (a): involving trilinear Higgs self-coupling; (b), (c), (d): the irreducible diagrams.

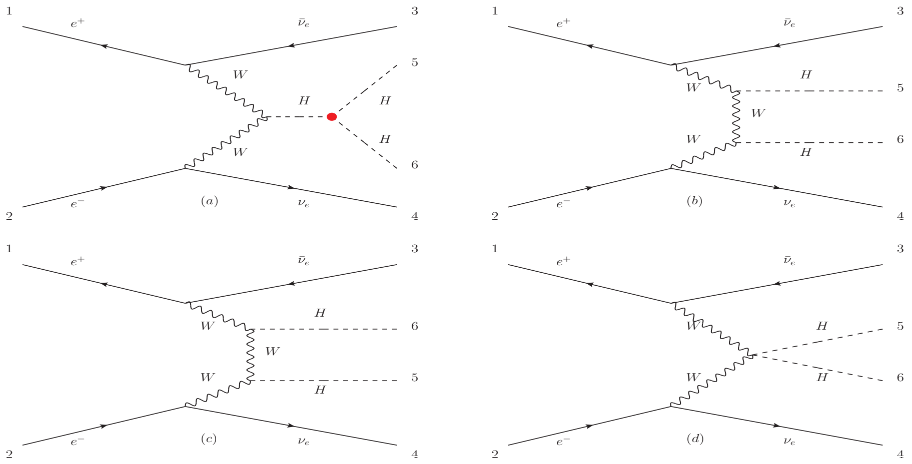

Figure 2.3: Feynman diagrams for WW fusion process $e^+ + e^- \rightarrow \nu\bar{\nu}$HH . (a): involving trilinear Higgs self-coupling; (b), (c), (d): the irreducible diagrams.

integrated luminosity.

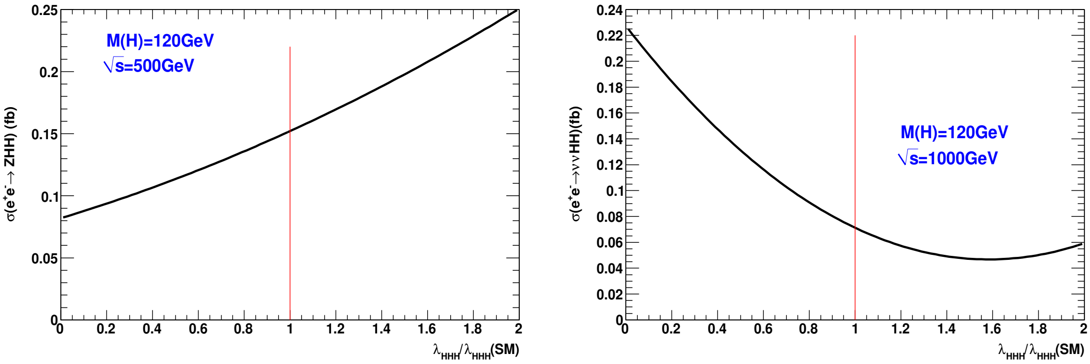

Figure 2.4: The evaluation of cross section as a function of the Higgs self-coupling. left: for $e^+ + e^- \to$ ZHH at 500 GeV; right: for $e^+ + e^- \to \nu\bar{\nu}$HH at 1 TeV. The g_{HHH} stands for the Higgs trilinear self-coupling and $g_{HHH}(SM)$ stands for the standard model value, which is denoted by the vertical line.

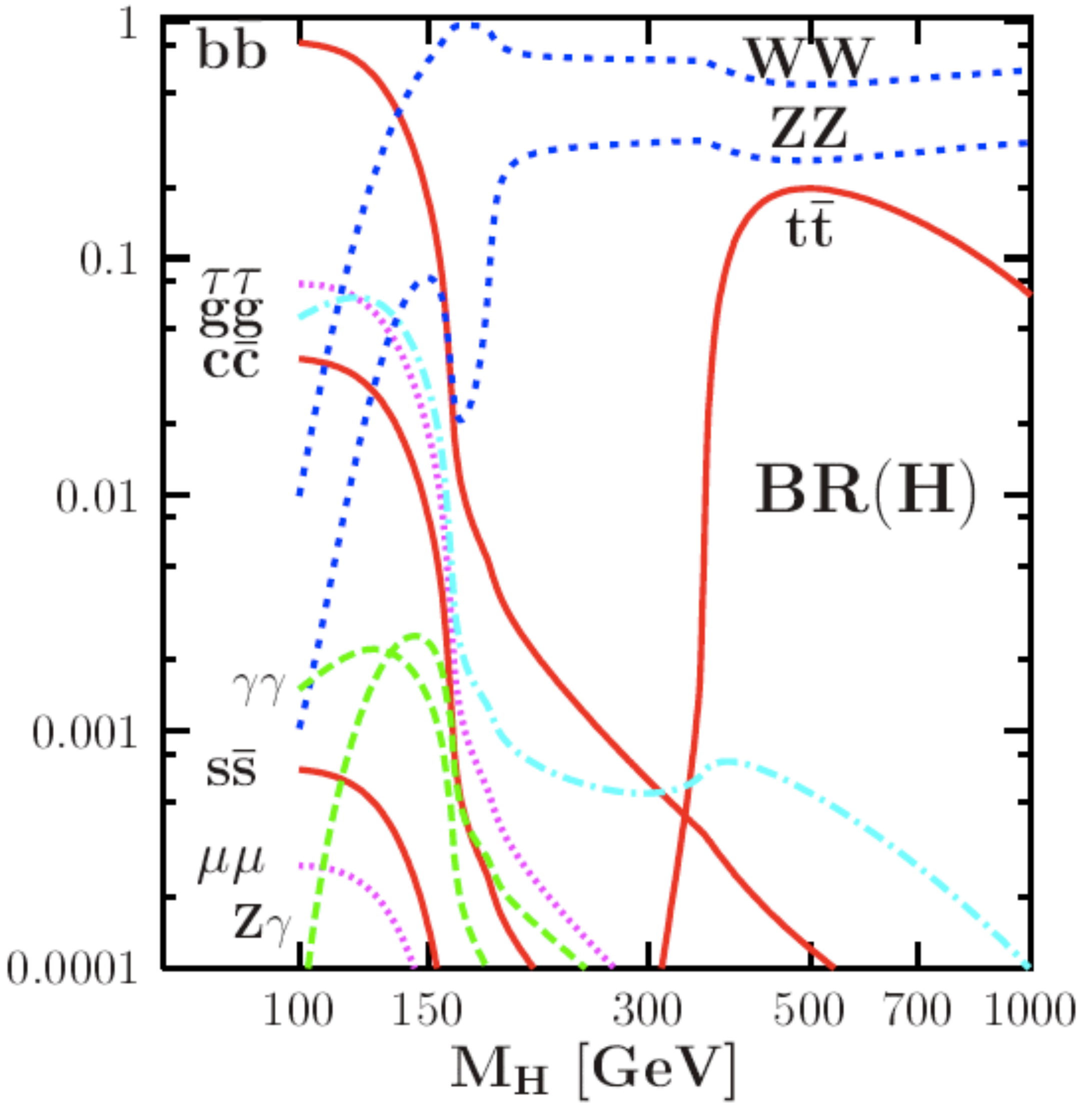

,

Figure 2.5: The decay branching ratio of SM Higgs as a function of its mass, from Refs. [42]

Chapter 3

Framework of Simulation and Reconstruction

A simulation study can be divided into three main steps. First is the preparing of generator, where the truth content of four momentum and helicity information is given for all the initial and final particles. Second is the detector simulation, where the effects of the detector on the final particles are presented. Third is the event reconstruction, where the information of an event is reconstructed. Usually, there are two types of simulation studies. One is called fast simulation, the other is called full simulation. The main difference between them is the step of detector simulation. In fast simulation, the interactions between detector and particles are not really simulated; the true information of each particle is smeared with the detector resolution. While in full simulation, each particle is followed through each sub-detector where detailed signals are generated. These signals are input to the reconstruction program in which the four momentum of each particle is estimated.

In this chapter, different frameworks used for full simulation and fast simulation are introduced. The core tools in each framework are presented.

3.1 Full Simulation

Mokka [48] and Marlin [49] are the framework used in full simulation, which are implemented with C++. The main components are as follows:

- Data Framework. STHEP [50] format is used as the output of generator and input of detector simulation, which is a common output format for Monte Carlo events in high energy physics, using the Particle Data Group numbering scheme. LCIO [51] format is used by the following detector simulation, event reconstruction and analysis. It is a persistency framework and event data model for linear collider detector studies, organizing the information of an event to several collections which can be accessed by all the simulation and reconstruction algorithms.

- Generator. Most of the studies use Whizard [52] as the generator, which is a program system designed for the efficient calculation of multi-particles scattering process cross sections and simulated event samples. Tree-level matrix elements are calculated by calling three alternative external programs, O'Mega [53], MadGraph [54] and CompHEP [55]. In this thesis, O'Mega is used by default. The phase space integration is handled by VAMP [56], where multi-channel parameterization is implemented. Parton showering is handled by PYTHIA [57]. Beam width, beamstrahlung and initial state radiation are considered in Whizard.

- Detector Simulator. Mokka is the detector simulator based on GEANT4 [58], which is a toolkit for simulation of the passage of particles through matter. A complete description of the ILD detector concept is implemented in Mokka. The interactions between particles and each sub-piece of ILD are fully simulated.
- Reconstruction and Analysis. Marlin is the modular application framework for reconstruction and analysis. Every computing task is implemented as a processor (module) in Marlin that analyzes data in an event and creates additional output collections that are added into the event. MarlinReco [59] is a software package of many different processors, such as track finding, cluster reconstruction. Among all, three processors are especially important, particle flow algorithm, flavor tagging and jet clustering.

3.1.1 Particle Flow Algorithm

At ILC, the separation of W and Z is an important part of the event selection for many physics analyses. This requires that the di-jet mass resolution should be comparable to the natural width of W and Z, $\sigma_m/m < 2.7\% \approx \Gamma_Z/m_Z \approx \Gamma_W/m_W$. In terms of jet energy resolution this requirement approximately corresponds to $\sigma_E/E < 3.8\%$. For a typical jet with energy of $80 \sim 350$ GeV, this sets requirement on the calorimetric performance $\sigma_E/E \approx 30\%/\sqrt{E}$, where E is in units of GeV. The traditional approach, where jet energy is obtained from the sum of energies deposited in ECAL and HCAL, results a jet energy resolution usually greater than $60\%/\sqrt{E}$. At LEP, the best jet resolution was achieved by ALEPH equivalent to $\sigma_E/E \approx 65\%/\sqrt{E}$ using the Energy Flow [60] algorithm, whereby the energies deposited in the calorimeters are removed according to the momentum of charged particle track. This is still a factor of two worse than that required for ILC.

The ILD concept is designed based on the belief that particle flow calorimetry provides the best way of achieving the jet energy resolution. The Particle Flow approach extends the concepts of Energy Flow to a highly granular detector. In contrast to a purely calorimetric measurement, Particle Flow calorimetry requires the reconstruction of the four momentum of all visible particles in an event. The reconstructed jet energy is the sum of energies of the individual particles. According to the jet fragmentation information measured at LEP [61], on average, roughly 60% of the jet energy is carried by charged particles (mainly hadrons), around 30% by photons and about 10% by neutral hadrons (n, $\bar{n}$ and K_L). The momenta of charged particles are measured in the tracking detectors, while the energy measurements for photons and neutral hadrons are obtained from the calorimeters. In this manner, the HCAL is used to measure only ~ 10% of the energy in the jet. The momentum resolution of tracking system and energy resolution of ECAL are much better than HCAL. It is therefore possible to achieve the jet resolution requirement for ILC physics.

Though there are several particle flow algorithms developed for ILC [62], PandoraPFA [63] is the most sophisticated and best performing algorithm, and is used for ILD detector concept. Figure 3.1 shows the jet energy resolution for $Z \to q\bar{q}$ $(q = u, d, s)$ events plotted against the cosine of the polar angle of the generated $q\bar{q}$ pair, $\cos\theta_{q\bar{q}}$, for four different values of jet energy. Figure 3.2 shows the reconstructed W and Z invariant masses, respectively from samples of $W^+W^- \to u\bar{d}\mu^-\bar{\nu}_\mu$ and $ZZ \to d\bar{d}\nu\bar{\nu}$ at $\sqrt{s}$ = 500 GeV. The output of PandoraPFA is a collection of individual particles, each of which is called Particle Flow Object (PFO). This collection is the basis of all the analysis.

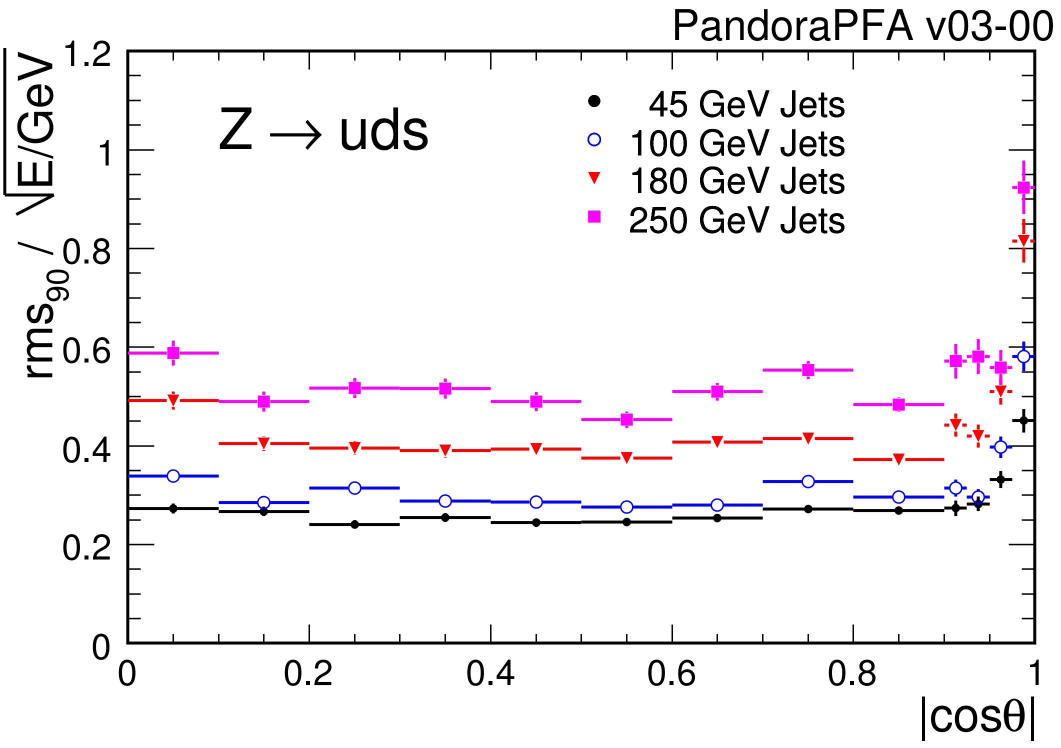

Figure 3.1: The jet energy resolution, defined as the α in $\sigma_E/E = \alpha\sqrt{E/\mathrm{GeV}}$, plotted versus $\cos\theta_{q\bar{q}}$ for four different jet energies [63].

3.1.2 Flavor Tagging Algorithm

Physics at ILC is expected to be rich in final states with heavy flavor jets. It is very important to be able to distinguish b-jets from c-jets and light quarks (u, d, s) jets. In a typical b jet containing a B hadron decay 5 mm from the interaction point, resulting in a D hadron that decays, e.g., 3 mm further away, it is often possible to reconstruct all three vertices from the tracks in the jet. So crucial for flavor tagging is the high precision measurement of the tracks of charged particles in the inner

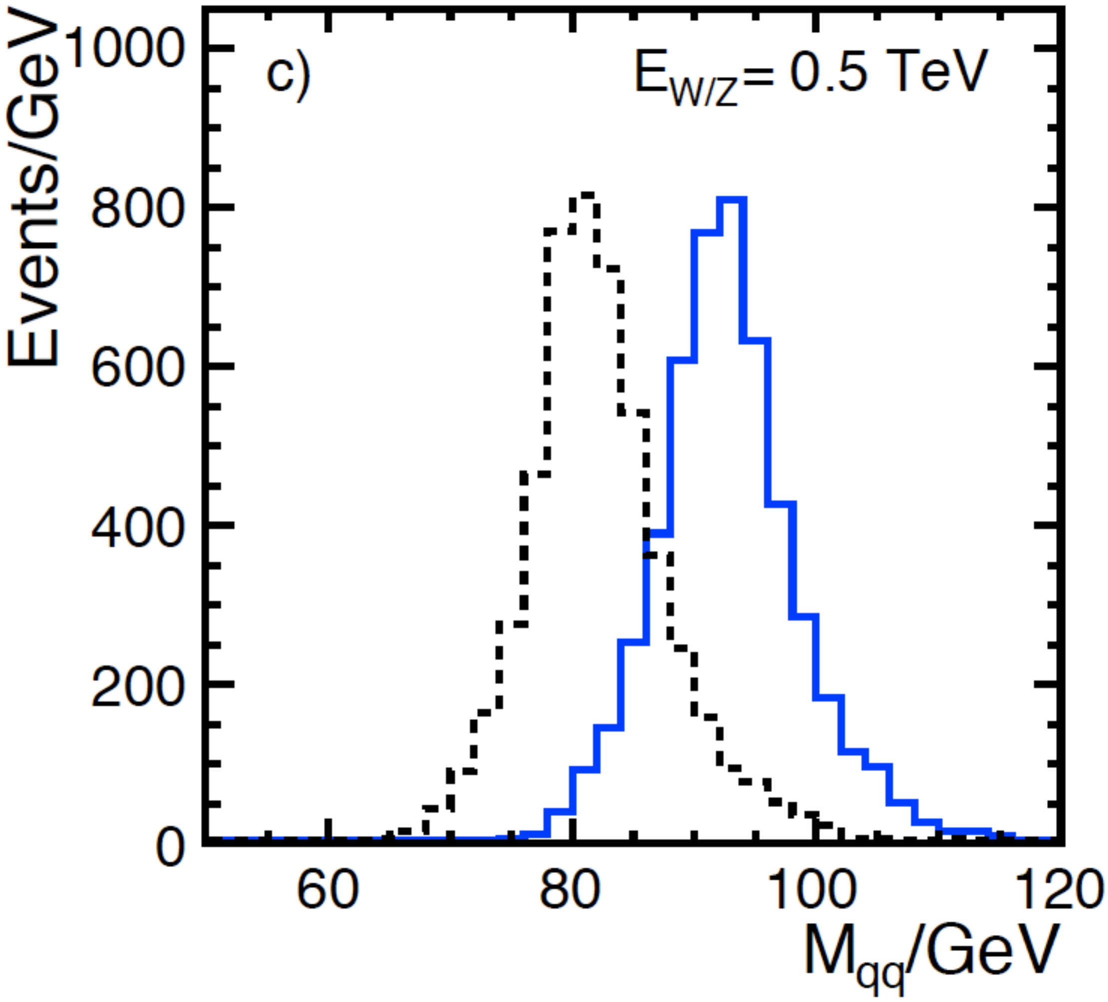

Figure 3.2: Reconstructed invariant mass distributions for simulated $ZZ \to d\bar{d}\nu\bar{\nu}$ (blue solid) and $W^+W^- \to u\bar{d}\mu^-\bar{\nu}_\mu$ (black dashed) events as simulated in ILD detector model, from Refs. [63].

most detector system, the Vertex Detector, permitting reconstruction of the decay vertices of heavy flavor hadrons.

The LCFIVertex [64] package implements the algorithms for vertex finding, flavor tagging and vertex charge identification. Nine artificial neural-nets (ANN) are used to identify the flavour of jets: three ANN are used to tag b-jets depending whether one, two or three or more vertices were found in a jet; another set of three ANN are dedicated to tag c-jets also depending on the number of vertices found in the jet; the last set of three ANN serves to tag c-jets in the presence of backgrounds containing only b-quarks. The outputs of these neural-nets are respectively called b-likeness, c-likeness and bc-likeness; typical results are shown in Figure 3.3. The flavour tagging performance of ILD is studied through $Z \to q\bar{q}$ events. Two vertex geometries are considered, three double-sided ladders (VTX-DL) and five single-sided (VTX-SL) ladders (see Figure 1.5); results are shown in Figure 3.4.

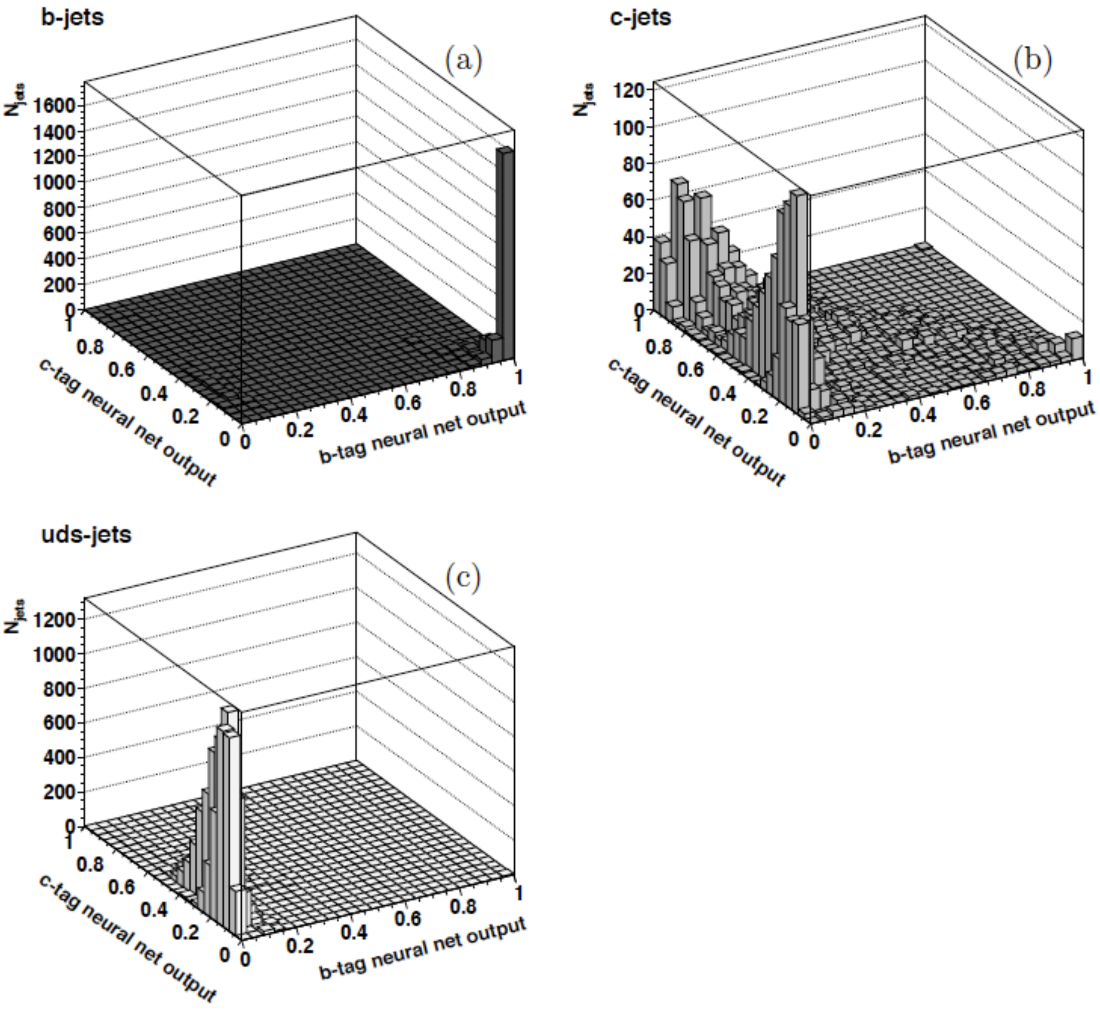

Figure 3.3: c tagging versus b tagging neural-net outputs for input samples consisting purely of (a) b-jets, (b) c-jets and (c) light quark jets, from Refs. [64].

3.1.3 Jet Clustering

Based on the PandoraPFOs collection, a jet clustering algorithm is used to combine all the particles into several jets. Such algorithm is iterative, beginning with a list of jets that are just all the particles:

1. List of current jets.

2. For each pair of jets i and j, calculate the variable Y_{ij}, where $Y_{ij} = M^2(i,j)/s$, where $M(i,j)$ is the invariant mass of jets i and j, $\sqrt{s}$ is the center of mass energy.

3. The pair i and j with the smallest value of Y_{ij} is combined as one jet. The four momentum of the jet equals sum of the four momentum of jets i and j, $P^\mu = P^\mu_i + P^\mu_j$.

4. Repeat the first step. When Y_{ij} is smaller than the pre-defined value Y_{cut},

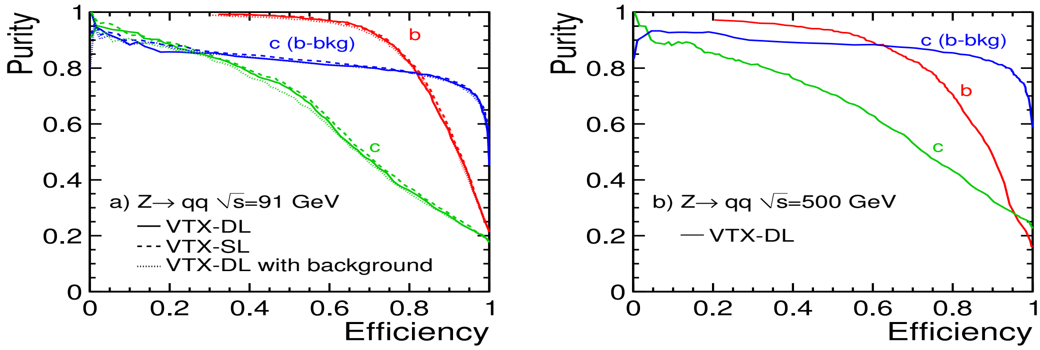

Figure 3.4: a) Flavour tagging performance of the ILD detector for 91 GeV $Z \to q\bar{q}$ events for both the three double-sided ladders (VTX-DL) layout and with five single-sided ladder layout (VTX-SL). Also shown for the VTX-DL is the impact of background on the flavour tagging performance. b) Flavour tagging performance of the ILD detector for 500 GeV $Z \to q\bar{q}$ events for the VTX-DL layout. In all cases the acceptance corresponds to $|\cos\theta_{\text{jet}}| < 0.95$, from Refs. [3].

$Y_{ij} < Y_{cut}$, or the number of current jets N_j is equal to the pre-defined number of jets N_0, $N_j = N_0$, the iteration stops.

The Y_{ij} is a dimensionless variable and the above definition is commonly used, named JadeE jet clustering algorithm. Another two definitions of Y_{ij} are also widely used. One is called JADE jet clustering algorithm[65], where

$$Y_{ij} = \frac{2E_iE_j(1-\cos\theta_{ij})}{s} \tag{3.1}$$

the other is is called Durham jet clustering algorithm [66], where

$$Y_{ij} = \frac{2Min(E_i^2, E_j^2)(1-\cos\theta_{ij})}{s}. \tag{3.2}$$

E_i and E_j are the energies of jets i and j, θ_{ij} is the angle between them, $Min(E_i^2, E_j^2)$ is the smaller one of E_i^2 and E_j^2.

Durham jet clustering is used in the full simulation part, by forcing an event to the fixed number of jets. Figure 3.5 shows the typical distribution of Y value for four partons process $\nu\nu bbbb$ and two partons process $\nu\nu bb$, where $Y_{4\to3}$ is the Y value obtained when combining four jets to three jets, indicating that Y value can offer discriminative power to events with different number of partons.

3.2 Fast Simulation

Fast simulation is based on the framework of JSF [67]. The Generator implemented is Physsim [68], where helicity amplitudes are calculated by the HELAS library [69], and the phase space integration is handled by BASES/SPRING [70]. Beam width, beamstrahlung and initial state radiation are considered in Physsim. Parton showering and hadronization are also carried out by PYTHIA. The detector simulation is

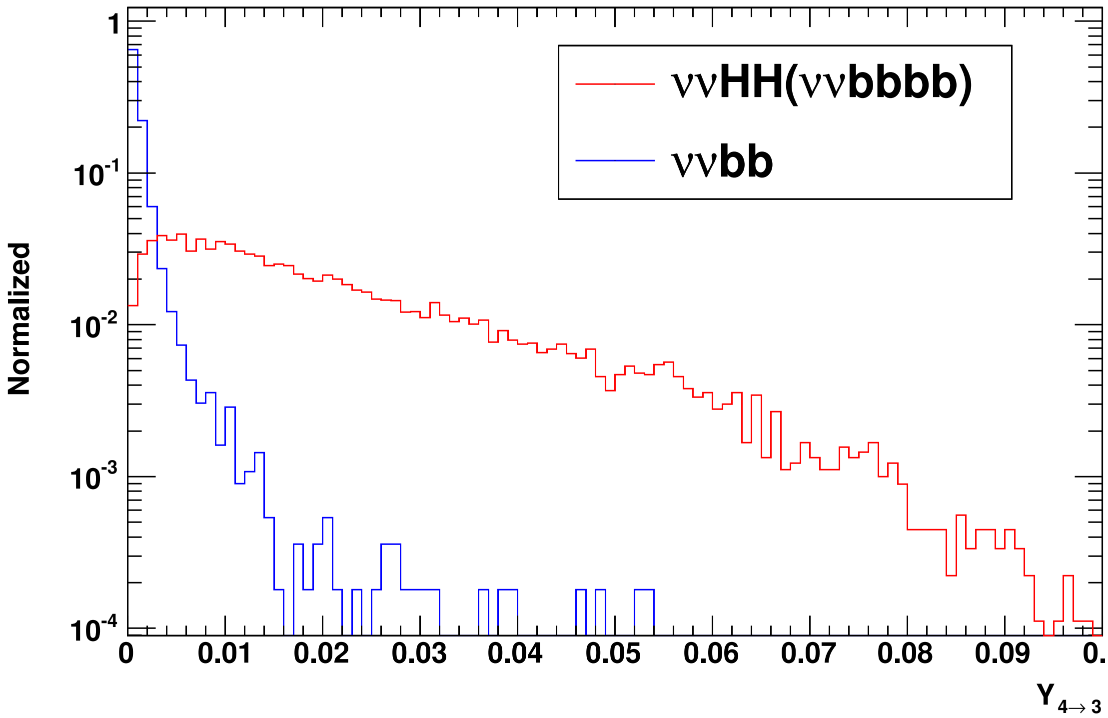

Figure 3.5: The Y value output by Durham jet clustering algorithm, from four jets to three jets. Red histogram denotes for $\nu\nu bbbb$ events and blue one denotes for $\nu\nu bb$ events.

done by JSFQuickSimulator [71], where the geometry and performance of detector concept GLD are implemented. For the reconstruction and analysis, the JadeE jet clustering algorithm where $Y_{ij} = M^2(i,j)/s$ is used. B tagging is implemented by a very simple algorithm, where the off-vertex tracks are counted as the flavour tagging information.

Chapter 4

Full Simulation of $e^+ + e^- \to l^+l^-\mathrm{HH} \to l^+l^-b\bar{b}b\bar{b}$ at 500 GeV

4.1 Signal and Backgrounds

In this search mode, the final state of a candidate signal event contains two isolated charged leptons and four b quarks segmenting into four jets. In order to avoid the complication of tau (τ) decays, only the electron (e) and muon (μ) modes are considered for the charged leptons. Most of the signal events come from the $e^+ + e^- \to \mathrm{ZHH}$ process with a small fraction from the $e^+e^-\mathrm{HH}$ events through the ZZ fusion. At 500 GeV, the cross section of $e^+ + e^- \to l^+l^-\mathrm{HH}$ without the initial beam polarization is 10.6 ab, assuming a Higgs mass of 120 GeV. This cross section is so small that almost every kind of background could contaminate the signal. Though we assume a very high integrated luminosity of 2 ab^{-1}, the expected number of the signal $l^+l^-\mathrm{HH}$ events is only 21.2, of which 9.5 events lead to $l^+l^-b\bar{b}b\bar{b}$ final states.

Because the b flavor tagging is very discriminative and there are four b jets in a signal event, the backgrounds which have less than two b jets can be neglected. We hence consider essentially all the standard model backgrounds having two or more b jets. The cross section of all the considered background processes and the expected number of events assuming the integrated luminosity of 2 ab^{-1} are shown in Table 4.1. The corresponding numbers of generated MC events are also shown there. In the table, all the processes are labeled by the parton level final states, where u, d, c, s, t and b denote the six species of quarks, q means the quarks lighter than c, l means the charged lepton, ν means the neutrino. Notice that anti-quarks are denoted by the same symbol as their corresponding quarks. Different processes having the same label are merged. For example, the background process $e^+ + e^- \to bbcsdu$ denotes both $e^+ + e^- \to b\bar{b}c\bar{s}d\bar{u}$ and $e^+ + e^- \to b\bar{b}\bar{c}s\bar{d}u$ and $e^+ + e^- \to l\nu bbqq$ denotes $e^+ + e^- \to l^+\nu_l b\bar{b}\bar{c}s$, $e^+ + e^- \to l^-\bar{\nu}_l b\bar{b}c\bar{s}$, $e^+ + e^- \to l^+\nu_l b\bar{b}\bar{u}d$ and $e^+ + e^- \to l^-\bar{\nu}_l b\bar{b}u\bar{d}$. The reason for treating these processes together is that they are very similar and after parton showering and fragmentation, it's very hard to tag the jet if it is from quark or anti-quark, though sometimes we can take advantage of the vertex charge information [72].

After all, the expected number of the signal events is very small while background is huge being about 10^4 times higher. It would be very challenging to suppress the backgrounds effectively without losing too many signal events.

Table 4.1: The cross section and expected number of events for signal and backgrounds without beam polarization at 500 GeV.

Process	Cross Section (fb)	Expected	MC
$e^+ + e^- \to l^+l^-\mathrm{HH}$	0.0106	21.2	39827
$e^+ + e^- \to bbcsdu$	115	230600	405727
$e^+ + e^- \to bbuddu$	58.1	116200	231600
$e^+ + e^- \to bbcssc$	57.8	115600	230701
$e^+ + e^- \to bbbbbb$	0.0034	6.9	19998
$e^+ + e^- \to bbbb$	11.8	23900	103401
$e^+ + e^- \to qqbb$	91.8	183768	353715
$e^+ + e^- \to qqcc$	51.7	103400	20672
$e^+ + e^- \to llbb$	158	316000	2520954
$e^+ + e^- \to llcc$	717	1434800	1611287
$e^+ + e^- \to l\nu bbqq$	239	477600	397602
$e^+ + e^- \to llbbbb$	0.0128	25.6	10924
$e^+ + e^- \to llbb\mathrm{H}$	0.0101	20.1	24000
$e^+ + e^- \to llqq\mathrm{H}$	0.0363	72.7	12000

4.2 Pre-selction

For the pre-selction, we first require there are two isolated oppositely charged leptons and then force all the PFOs other than the two selected leptons to four jets and pair the four jets to two Higgs boson candidates.

4.2.1 Isolated Lepton Selection

As mentioned in Chapter 3, an event is reconstructed as a collection of PFOs. From these PFOs, isolated electrons and muons are identified. Each PFO contains the information from different sub-detectors, such as energies deposited in the ECAL and HCAL. An electron deposits almost all the energy in ECAL while a muon deposits very small fraction of its energy in both ECAL and HCAL. Other charged particles, being mainly hadrons, deposit most of their energy in HCAL. These pieces of information are used for electron and muon identification. The following two quantities are checked for each PFO. One is the $\frac{\mathrm{E(ecal)}}{\mathrm{E(total)}}$ ratio, the other is the $\frac{\mathrm{E(total)}}{\mathrm{P}}$ ratio, where $\mathrm{E(total)} = \mathrm{E(ecal)} + \mathrm{E(hcal)}$, E(ecal) and E(hcal) are the energies deposited in ECAL and HCAL and P is the momentum.

- For electron identification, two samples of PFOs from the process $e^+ + e^- \to e^+e^-\mathrm{HH}$ are investigated by using MC truth information. One is the real prompt charged electrons, and the other is all the charged PFOs other than the two prompt charged leptons. Figure 4.1 shows the distributions of the above two quantities for these two samples, where the red histogram is for the prompt electrons and the blue is for non-prompt charged PFOs. Since the red and blue distributions are very different it is straightforward to find conditions to these two quantities

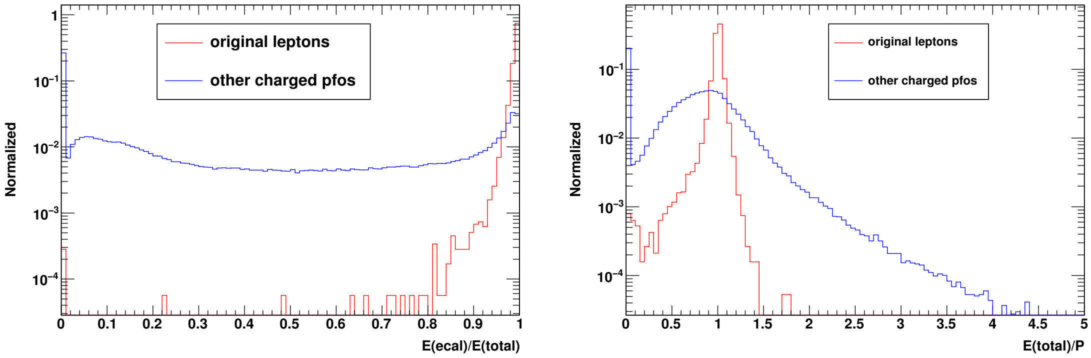

Figure 4.1: The distribution of $\frac{\mathrm{E(ecal)}}{\mathrm{E(total)}}$ (left) and $\frac{\mathrm{E(total)}}{\mathrm{P}}$ (right) for PFOs in sample $e^+ + e^- \to e^+e^-\mathrm{HH}$. The red histogram is for prompt electrons and the blue one is for other charged non-original PFOs.

$$e : \begin{cases} \frac{E(ecal)}{E(total)} > 0.9 \\ 0.8 < \frac{E(total)}{P} < 1.2 \end{cases} \tag{4.1}$$

After these requirements, the mis-identified electrons are mainly from: (i) charged pions, which become neutral pions through charge exchange interaction with the nuclei inside ECAL, decaying into photons which deposit almost all of their energies in ECAL; (ii) electrons from weak decays of b or c quarks, such as $b \to cW^- \to ce^-\bar{\nu}_e$; (iii) electrons from a Higgs boson decaying into WW^* followed by a semi-leptonic W decay. Type (i) and (ii) mis-identified PFOs usually have smaller momenta and more PFOs around them due to parton showering and fragmentation than the prompt electrons. It is hence possible to further reduce the mis-identification by using the cone energy. For each PFO, define a cone with angle θ, around the momentum of that PFO as shown in Figure 4.2, and sum up the energies of the other PFOs which are inside this cone. This energy sum is called the cone energy. If only the charged PFOs are considered, then the sum is called the charged cone energy. The effect of bremsstrahlung tends to give the prompt electrons a sizable cone energy. This makes the charged cone energy more discriminative to separate the prompt electrons from the other PFOs. Figure 4.3 shows a scatter plot of charged cone energy versus momentum of the PFOs from these two samples, where the red points denote prompt electrons and the blue points denote the remaining mis-identified non-prompt charged PFOs. By using Fisher classification, we decided to impose

$$P - 0.25E_{\mathrm{cone}} > 12.6 \text{ GeV} \tag{4.2}$$

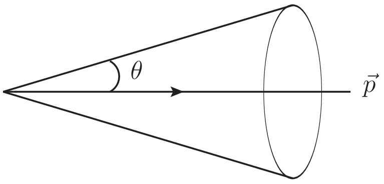

Figure 4.2: Schematic view of a cone around a particle with momentum $\vec{p}$. The cone angle is θ.

where E_{cone} is the charged cone energy and P is the momentum. To evaluate the performance of electron identification, we defined the efficiency and purity

$$\text{Efficiency} = \frac{N_{\text{true}\bigcap\text{id}}}{N_{\text{true}}}, \quad \text{Purity} = \frac{N_{\text{true}\bigcap\text{id}}}{N_{\text{id}}}, \tag{4.3}$$

where N_{true} is the number of prompt electrons, N_{id} is the number of PFOs which are identified as electrons, and $N_{\text{true}\bigcap\text{id}}$ means the number of prompt electrons passing the identification. The efficiency and the purity after each requirement are shown in Table 4.2.

Table 4.2: Efficiency and Purity of electron identification after each requirement.

	N_{true}	Efficiency (%)	Purity (%)
no cut	18846	100	4.16
$\frac{E(ecal)}{E(total)} > 0.9$	18788	99.7	10.6
$0.8 < \frac{E(total)}{P} < 1.2$	18375	97.5	26.3
$P - 0.25E_{\text{cone}} > 12.6$ GeV	18024	95.6	89.3

- For muon identification, the strategy is very similar to the electron identification. Samples for prompt muons and the other charged PFOs are from the $e^+ + e^- \to \mu^+\mu^-\mathrm{HH}$ process. The distributions of $\frac{\mathrm{E(ecal)}}{\mathrm{E(total)}}$ and $\frac{\mathrm{E(total)}}{\mathrm{P}}$ are shown in Figure 4.4. The requirements to these two quantities are

$$\mu : \begin{cases} \frac{E(ecal)}{E(total)} < 0.5 \\ \frac{E(total)}{P} < 0.3 \end{cases} \tag{4.4}$$

In this case, the mis-identified muons are mainly from: (i) charge pions which have small momentum and do not reach HCAL, thereby having small energy deposits in ECAL and HCAL; (ii) and (iii) are similar to the electron case, namely from weak decays of b, c quarks and from Higgs decaying into WW^*. Also, the charged cone energy and momentum can be used to further reduce the mis-identification. A scatter plot of the charged cone energy versus momentum for the samples of prompt muons and the other non-prompt PFOs are shown in Figure 4.5. We require

$$P - 0.1E_{\text{cone}} > 17.1 \text{ GeV}. \tag{4.5}$$

The efficiency and the purity after each requirement are shown in Table 4.3.

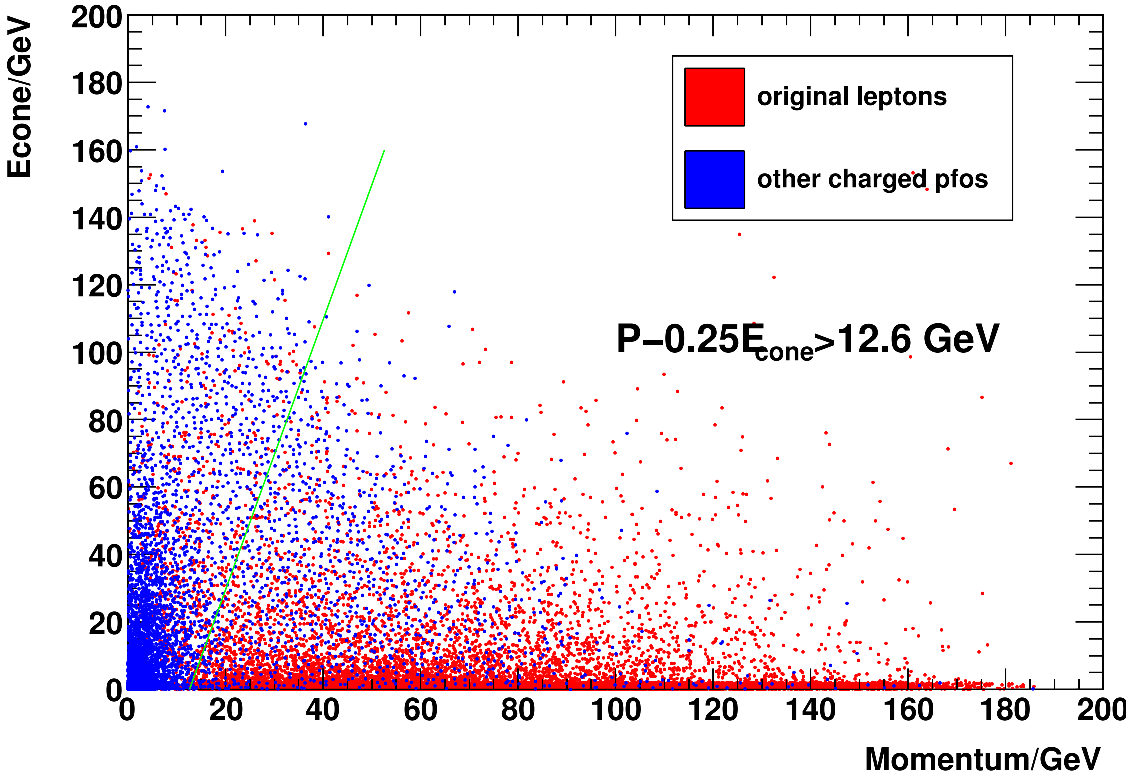

Figure 4.3: Scatter plot of charged cone energy versus momentum for PFOs in sample $e^+ + e^- \to e^+e^-\text{HH}$. Red points denote original electrons and blue ones denote other charged non-original PFOs.

The angle of the cone in Figure 4.2 is expected to affect the performance of charged lepton selection. To minimize the mis-identification, the value of the cone angle θ is scanned from $\cos\theta = 0.8$ to $\cos\theta = 1$. At each value, while fixing the efficiency for the prompt lepton identification to 98%, we looked at the efficiency of the other charged PFOs being identified. The result is shown in Figure 4.6. The optimized cone angle $\cos\theta = 0.98$ giving the minimal mis-identification efficiency is adopted.

For each event, at least two oppositely charged PFOs are required to be both identified as electron or muon. If there are more than two PFOs identified, we look at all the pairs which have opposite charge. The pair of which the invariant mass is the nearest to the mass of Z, $M(Z) = 91.18$ GeV, is selected as the two prompt charged leptons, effectively suppressing type (iii) mis-identification. As a

Table 4.3: Efficiency and Purity of muon identification after each requirement.

	N_{true}	Efficiency (%)	Purity (%)
no cut	19498	100	4.26
$\frac{E(ecal)}{E(total)} < 0.5$	18975	97.3	8.21
$\frac{E(total)}{P} < 0.3$	18715	96.0	17.1
$P - 0.1E_{\text{cone}} > 17.1$ GeV	18359	94.2	91.6

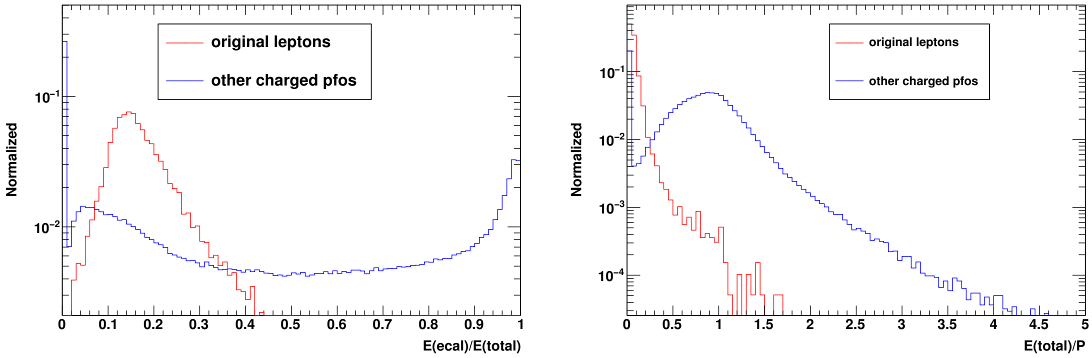

Figure 4.4: The distribution of $\frac{\mathrm{E(ecal)}}{\mathrm{E(total)}}$ (left) and $\frac{\mathrm{E(total)}}{\mathrm{P}}$ (right) for PFOs in the $e^+ + e^- \to \mu^+\mu^-\mathrm{HH}$ sample. The red histogram is for prompt muons and the blue one is for the other charged PFOs.

loose requirement, the invariant mass of the two selected charged leptons $M(l^+l^-)$ should satisfy

$$|M(l^+l^-) - M(Z)| < 40 \text{ GeV}. \tag{4.6}$$

The distribution of $M(l^+l^-)$ for the signal events after the above selection is shown in Figure 4.7, where the Z resonance is clearly seen as expected. There are tails in the low mass end for both electron and muon modes, due to the final state radiations from the two charged leptons from a Z decay. The slight shift of the mass distribution for the electron mode comparing to that of the muon mode is due to bremsstrahlung from the electrons in the detector materials, though overwhelmed by the final state radiation.

4.2.2 Jet Clustering and Jet Pairing

After the two charged leptons are selected, all the other PFOs are forced to four jets by using the Durham jet algorithm. Then the four jets j_1, j_2, j_3 and j_4 are combined to two pairs, each of which contains two jets. Among all the possible combinations, the one which minimizes the χ^2 is selected. The χ^2 is defined by

$$\chi^2 = \frac{(M(j_1, j_2) - M(H))^2}{\sigma_H^2} + \frac{(M(j_3, j_4) - M(H))^2}{\sigma_H^2} \tag{4.7}$$

where $M(j_1, j_2)$ is the invariant mass of jets j_1 and j_2, $M(H)$ is the nominal Higgs mass, and σ_H is the Higgs mass resolution, which doesn't affect the combination here. The two jets pairs are reconstructed as two Higgs bosons. The order of the two Higgs bosons are determined by the order of jets output from the jet clustering algorithm. Usually a jet output earlier has a relatively larger momentum. While pairing, $M(j_1, j_2)$ and $M(j_3, j_4)$ are required to satisfy loose cuts:

$$|M(j_1, j_2) - M(H)| < 80 \text{ GeV}, \quad |M(j_3, j_4) - M(H)| < 80 \text{ GeV}. \tag{4.8}$$

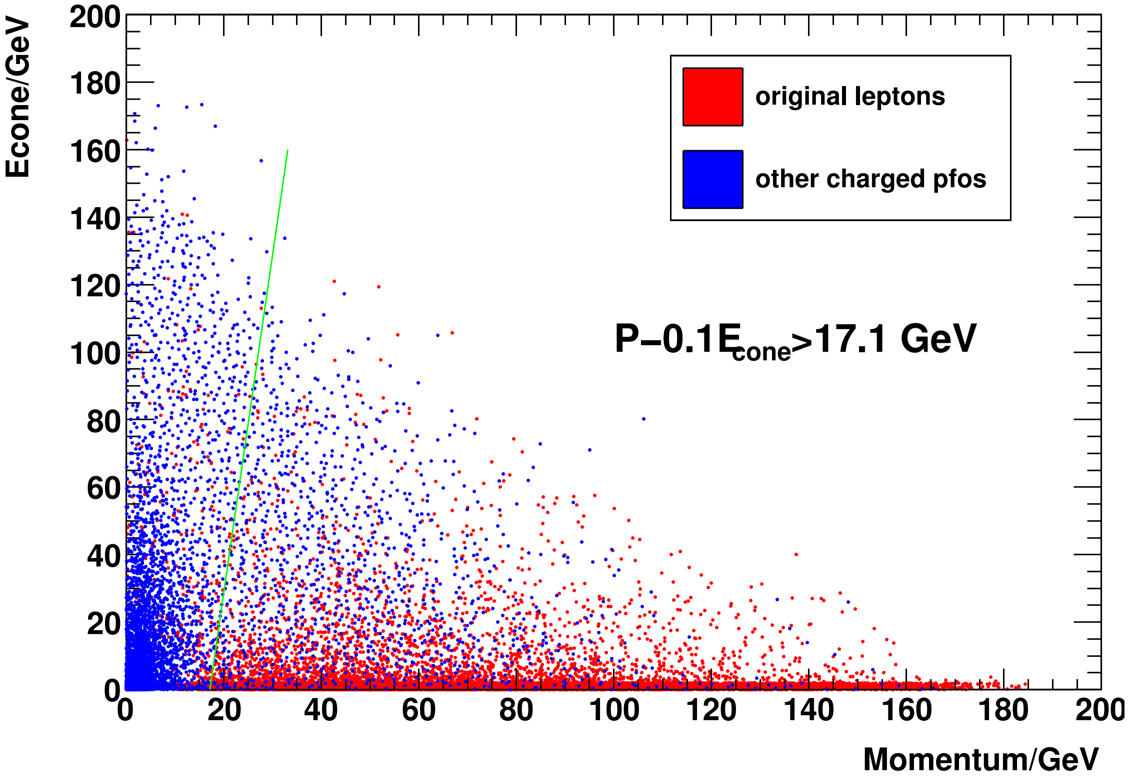

Figure 4.5: Scatter plot of charged cone energy versus momentum for PFOs in the $e^+ + e^- \to \mu^+\mu^-\mathrm{HH}$ sample. Red points denote prompt muons and blue ones denote the other charged PFOs.

4.3 Final Selection

The remaining signal and background events after the pre-selection are shown in Table 4.4. All the backgrounds can be grouped into four: first one, called full hadronic background, such as *bbcsdu*, *bbuddu*, *bbcssc* and *bbbb*, without leptons in the parton level final states; second one, called jets-poor background, such as *llbb* and *llcc*, only two partons with two leptons in the parton level final states; third one, called semi-leptonic background, such as $l\nu bbqq$, with one charged lepton, one missing neutrino and four partons in the parton level final states; the last one, called the most signal-like background, such *llbbbb* and *llbb*H, with two charged leptons and four partons in the parton level final states. Since the event topologies and the amounts of contamination from these four groups are very different, it is not very efficient if we use only one multivariate classification for the whole backgrounds. Actually it is almost impossible to find any global minimum if we put together the backgrounds with very different topologies and very different weights, considering the limited MC statistics. Instead of one multivariate classification, the strategy adopted is to use a separate multivariate classification to suppress the backgrounds in each group.

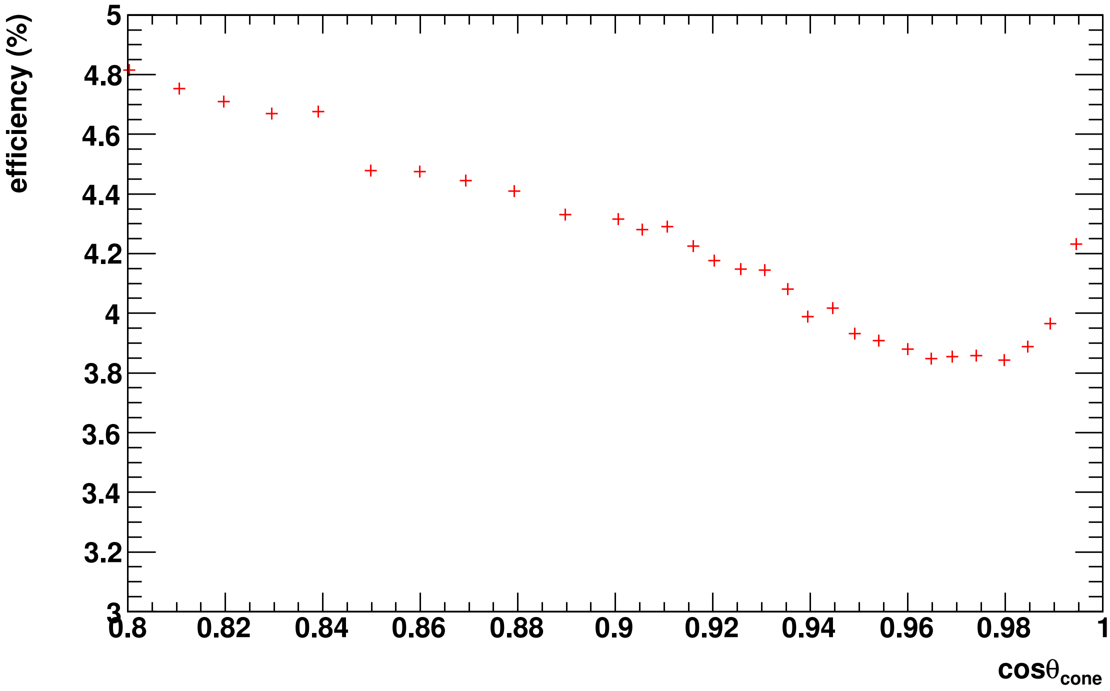

Figure 4.6: Optimization of cone angle using PFOs in the $e^+ + e^- \to e^+e^-\mathrm{HH}$ sample.

4.3.1 Full Hadronic Backgrounds

The full hadronic backgrounds, which mainly come from $e^+ + e^- \to t\bar{t}$, WWZ and ZZ, are significantly suppressed by the pre-selection mainly due to the requirement of two charged leptons. Even though, the number of remaining events is still much larger than that of the signal. For these backgrounds, the selected charged leptons must have come from the hadronization and decay, as a result of which the momenta of the charged leptons should relatively be smaller and the cone energy relatively larger. A natural strategy to further suppress them is to apply tighter cuts on the cone energy and momenta of the two selected charged leptons. Figure 4.8 shows the scatter plot of the total cone energy ($E_{\mathrm{cone}}12$) versus the total charged cone energy ($E_{\mathrm{cone}}\mathrm{Charge}12$) of the two leptons, and the distribution of the total momentum ($p\mathrm{Lep}_1 + p\mathrm{Lep}_2$). Tighter requirements are imposed to further suppress the full hadronic backgrounds, which is denoted as Cut1:

$$\mathrm{Cut1}: \left\{ \begin{array}{l} E_{\mathrm{cone}}12 + 4E_{\mathrm{cone}}\mathrm{Charge}12 < 60\ \mathrm{GeV} \\ p\mathrm{Lep}_1 + p\mathrm{Lep}_2 > 80\ \mathrm{GeV} \end{array} \right. \tag{4.9}$$

After these tighter requirements, the full hadronic backgrounds are almost completely eliminated, as indicated in Table 4.5

4.3.2 Jets-Poor Backgrounds

The jets poor backgrounds $llbb$ and $llcc$, which mainly come from ZZ, ZZ^*, $b\bar{b}Z$ and l^+l^-Z, are the dominant backgrounds after the pre-selection in Table 4.4. Though

Table 4.4: The remaining signal and background events after the pre-selection without beam polarization. The second line of signal llHH in parentheses denotes the contribution of $llbbbb$ decays from llHH.

Process	before selection	pre-selection
$e^+ + e^- \to ll\mathrm{HH}$ ($llbbbb$)	21.2 (9.5)	17.4 (7.81)
$e^+ + e^- \to bbcsdu$	230600	328.5
$e^+ + e^- \to bbuddu$	116200	158
$e^+ + e^- \to bbcssc$	115600	167
$e^+ + e^- \to bbbbbb$	6.9	0.034
$e^+ + e^- \to bbbb$	23900	99.4
$e^+ + e^- \to qqbb$	183768	236
$e^+ + e^- \to qqcc$	103400	40.0
$e^+ + e^- \to llbb$	316000	12961
$e^+ + e^- \to llcc$	1434800	12511
$e^+ + e^- \to l\nu bbqq$	477600	8614
$e^+ + e^- \to llbbbb$	25.6	8.75
$e^+ + e^- \to llbb\mathrm{H}$	20.1	17.0
$e^+ + e^- \to llqq\mathrm{H}$	72.7	61.2

Table 4.5: The remaining signal and full hadronic background events after tighter cuts on the cone energy and momenta of charged leptons (as denoted by Cut1).

Process	before selection	pre-selection	Cut1
$e^+ + e^- \to ll\mathrm{HH}$ ($llbbbb$)	21.2 (9.5)	17.4 (7.81)	16.0 (7.15)
$e^+ + e^- \to bbcsdu$	230600	328.5	0
$e^+ + e^- \to bbuddu$	116200	158	0
$e^+ + e^- \to bbcssc$	115600	167	0
$e^+ + e^- \to bbbbbb$	6.9	0.034	0
$e^+ + e^- \to bbbb$	23900	99.4	0.23
$e^+ + e^- \to qqbb$	183768	236	0
$e^+ + e^- \to qqcc$	103400	40.0	0

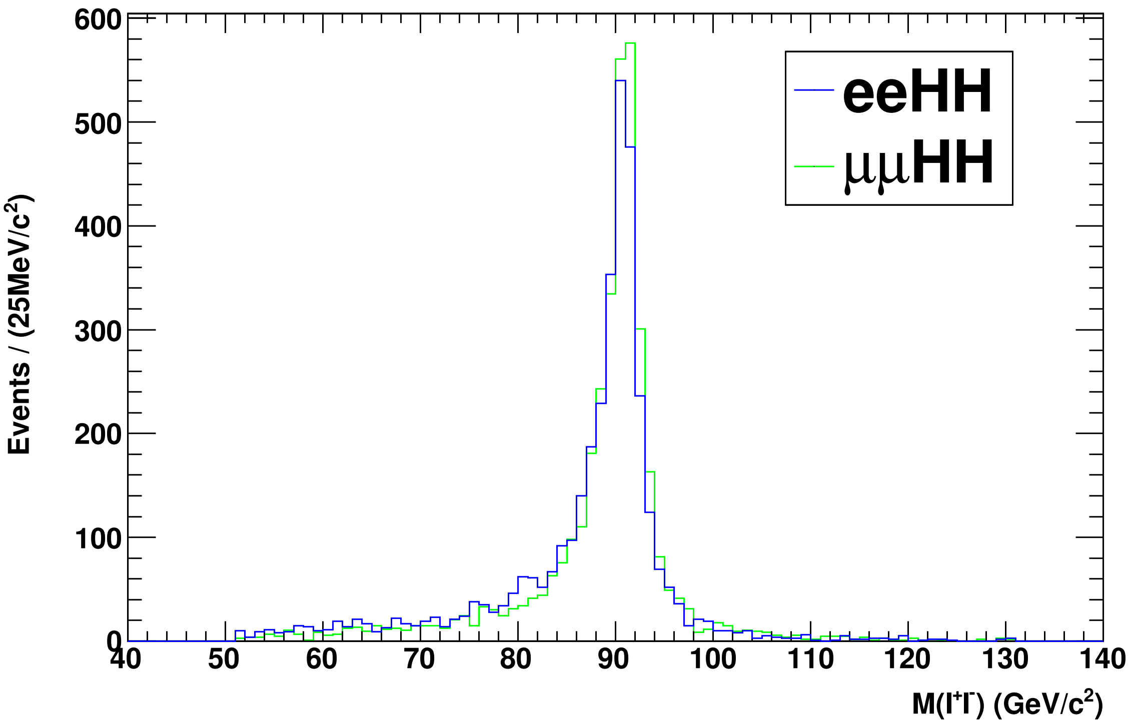

Figure 4.7: Invariant mass of the two selected charged leptons. Blue histogram is for the electron mode of the signal $e^+ + e^- \to e^+e^-\mathrm{HH}$ process; Green one is for the muon mode of the signal $e^+ + e^- \to \mu^+\mu^-\mathrm{HH}$ process.

there are only two partons in their parton level final states, due to the imperfection of the jet clustering algorithm, they can be clustered to four jets and some of them survived the mass constraints in Eqn. 5.3. To suppress these backgrounds while keeping as many signal events as possible, one of the multivariate data analysis methods, neural-net is used. The following discriminative quantities are included for the neural-net training:

- Y value, which is given by the jet clustering algorithm, as introduced in Chapter 3. Because there are only two partons for these jets poor backgrounds, their Y values are relatively smaller than that of the signal events. Among all the Y values, $Y_{4\to3}$ and $Y_{3\to2}$ turned out to be the most discriminative. The distributions of $Y_{4\to3}$ and $Y_{3\to2}$ are shown in Figure 4.9, respectively denoted by "yminus"and "yplus2".
- Thrust, which is derived from the quantity

$$p = \frac{\sum_i |\vec{p}_i \cdot \vec{n}|}{\sum_i |\vec{p}_i|} \tag{4.10}$$

where $\vec{p}_i$ is the momentum of a PFO, $\vec{n}$ is any possible unit vector $|\vec{n}| = 1$ and the summation is over all the PFOs in each event. The thrust is defined to be the maximum of p, and the corresponding $\vec{n}$ is called the axis of the event. The thrust value reflects the anisotropy of an event, indicating if there is any

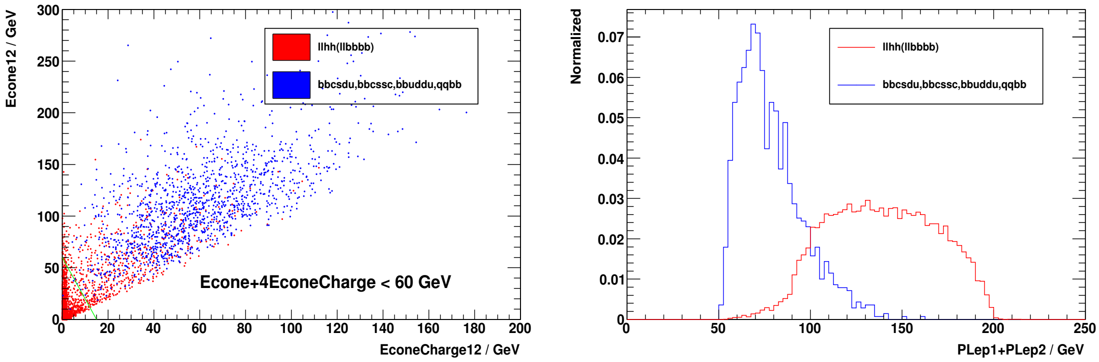

Figure 4.8: The scatter plot of $E_{\mathrm{cone}}12$ versus E_{cone}Charge12(left) and the distribution of $p\mathrm{Lep}_1 + p\mathrm{Lep}_2$ (right). Red denotes signal and blue denotes full hadronic backgrounds.

special direction favored by this event. Because these jets poor backgrounds are mainly from two-body t-channel processes, most of the PFOs in each event are very forward or backward. Their thrust is much closer to 1 than that of the signal, which is from a three-body process. The axis of these backgrounds is much closer to the beam direction than that of the signal. The distributions of the thrust value and the polar angle of the thrust axis are shown in Figure 4.9, respectively denoted by “pthrust” and “cosaxis”.

- Reconstructed Z mass. Some of these backgrounds are from ZZ, Zγ, or $\gamma\gamma$ fusion processes and from s-channel processes, where two charged leptons in the final states are not from a Z decay. In this case, the reconstructed Z mass does not peak at the nominal Z mass, as indicated by the flat part in the distribution of the reconstructed Z mass in Figure 4.9, denoted by “mz”.

- The total number of PFOs. For this background, the total number of PFOs is much smaller than that of the signal, because there are only two partons. The distribution of this quantity is shown in Figure 4.10, denoted by “npfos”.

- The smallest number of PFOs in a jet. For the same reason, the smallest number of PFOs in a jet is much smaller than that of the signal. The distribution of this quantity is shown in Figure 4.10, denoted by “npfomin”.

- The largest jet momentum when reconstructed as two jets. If we force the PFOs other than the two selected charged leptons to two jets, the momenta of these jets for the background will be relatively larger than signal. The Distribution of this quantity is shown in Figure 4.10, denoted by “pjmaxjets2”.

- The largest angle between the reconstructed Z and the other two jets. Some of these backgrounds come from $e^+ + e^- \to b\bar{b}Z$, where Z is radiated from one of the two b partons. In this case, the Z is very close to one of the two b jets. The distribution of this quantity is shown in Figure 4.9, denoted by “cosjzmax2”.

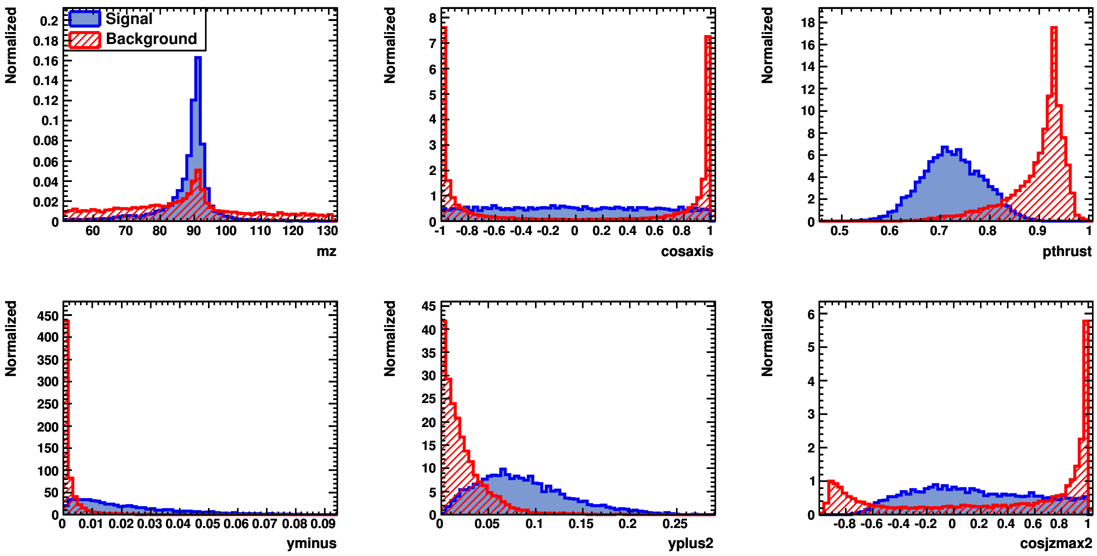

Figure 4.9: Discriminative quantities for the signal (blue) and the jets-poor backgrounds $llbb$ (red). The variable names are explained in the text.

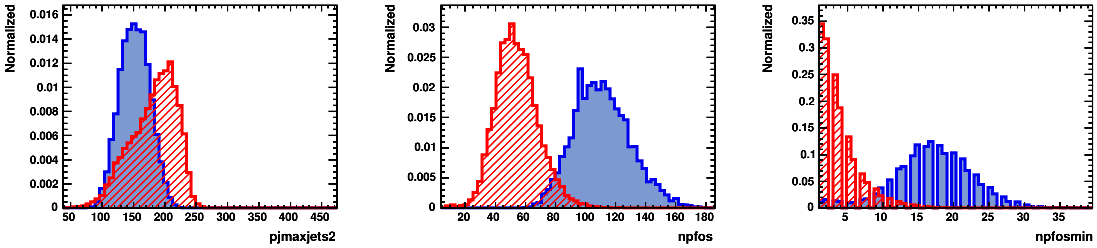

Figure 4.10: Discriminative quantities for the signal (blue) and the jets-poor backgrounds $llbb$ (red). The variable names are explained in the text.

These quantities are used as input variables by the MLP method in the TMVA package [73]. A neural-net is trained for the signal and the $llbb$ background. For the neural-net training, additional statistically independent signal $e^+e^-\mathrm{HH}$, $\mu^+\mu^-\mathrm{HH}$ and background $llbb$ samples are used. The weights for different processes are normalized to the corresponding cross sections. The statistics of the training samples are higher than 2 ab^{-1} for both the signal and the background. The neural-net outputs and cut efficiencies for the signal and the background are shown in Figure 4.11. The $llbb$ background is well separated by the neural-net output (MLP$_{llbb}$). A cut, MLP$_{llbb} > 0.62$, is imposed to suppress the $llbb$ background, denoted by MLP1. Though the neural-net is trained for the $llbb$ background, another jets-poor background $llcc$ is also significantly suppressed by this cut.

4.3.3 Semi-leptonic Backgrounds

The semi-leptonic backgrounds such as $e^-\bar{\nu}b\bar{b}\bar{c}s$, $e^-\bar{\nu}b\bar{b}\bar{u}d$, and their corresponding muon or tau modes, together with their conjugate modes, are mainly from $t\bar{t}$ and

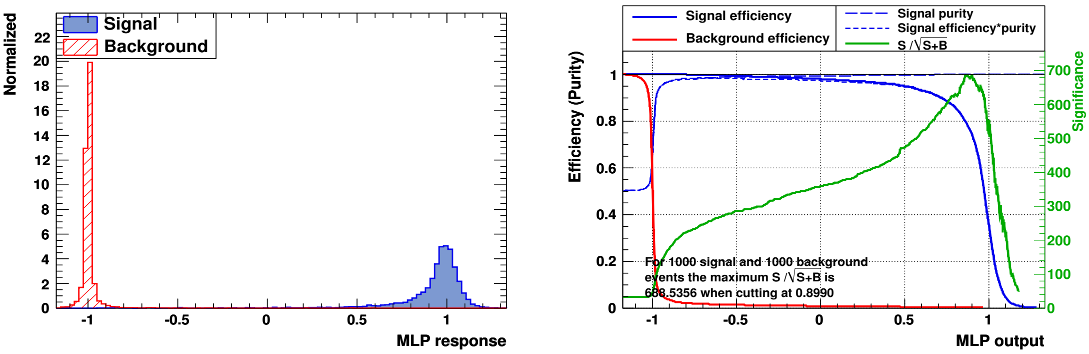

Figure 4.11: (left): The neural-net output for the signal versus the $llbb$ background, where the blue histogram is for the signal and the red one is for $llbb$. (right): The cut efficiencies for the signal and background at different cut values on neural-net output, where the solid blue curve is for the signal and the red one is for $llbb$.

W^+W^-Z. After the pre-selection, they are the second dominant backgrounds, being hundreds times more than the signal events. Unlike the jets-poor backgrounds, these semi-leptonic backgrounds have four quarks, but only one prompt charged leptons. We trained another neural-net to suppress these backgrounds by using the following quantities:

- Visible energy and missing P_t. Because there's one prompt neutrino in the backgrounds, the visible energy is smaller and the missing P_t is larger for the backgrounds than for the signal. The distributions of these two quantities are shown in Figure 4.12, respectively, denoted by “evis” and “mpt”.

- Cone energy and momentum of the lower momentum selected charged lepton. Because there's only one prompt charged lepton in the backgrounds, the other selected charged lepton must have originated from hadronization and decay, which has larger charged cone energy and smaller momentum. The distributions of these two quantities are shown in Figure 4.12, respectively, denoted by “econec2” and “plmin”.

- Reconstructed Z mass. The invariant mass of the two selected charged leptons should be very different for the backgrounds, as indicated in Figure 4.13, denoted by “mz”.

- The total number of PFOs. During parton showering, a b quark usually results in more particles than light quarks. So the total number of PFOs for the backgrounds is smaller than that of the signal. This information is independent of the b tagging algorithm. The distribution of this quantity is shown in Figure 4.13, denoted by “npfos”.

- Reconstructed W mass. The four jets are ordered from the largest b-likeness to the smallest. The backgrounds contain two b quark jets and two light quark jets. The two light quarks are from a W decay. The invariant mass of the 3rd and 4th jets are reconstructed as the W mass. The distribution of this quantity is shown in Figure 4.12, denoted by “massb34”.

- Angle between two b jets. A large fraction of these backgrounds come from $t\bar{t}$, where the angle between two prompt b jets is relatively large. The angle between 1st and 2nd jets are reconstructed as the angle between the two prompt b jets. The distribution of this quantity is shown in Figure 4.12, denoted by “cosbmax”.

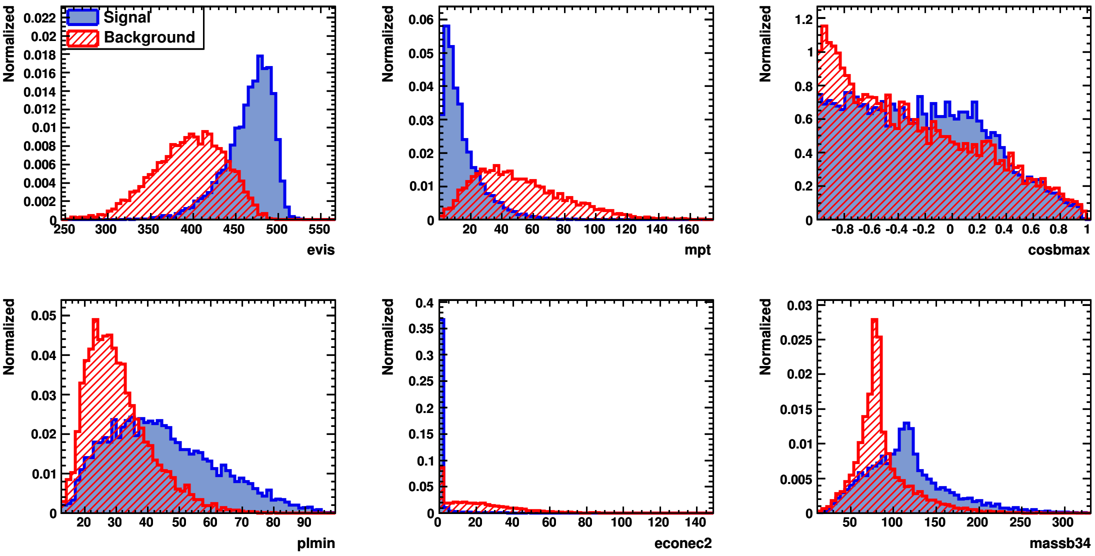

Figure 4.12: Discriminative quantities for the signal (blue) and the semi-leptonic backgrounds *lvbbqq* (red). The variable names are explained in the text.

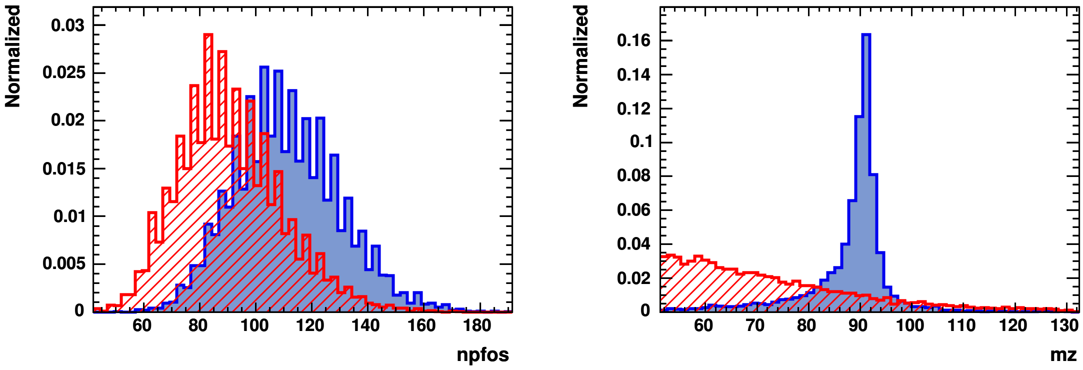

Figure 4.13: Discriminative quantities for the signal (blue) and the semi-leptonic backgrounds *lvbbqq* (red). The variable names are explained in the text.

Statistically independent *ll*HH signal sample and the *lvbbqq* background samples are used for the neural-net training. The statistics are higher than 2 ab^{-1} for both the signal and the background. The neural-net outputs and cut efficiencies for signal and background are shown in Figure 4.14. The *lvbbqq* background can well be separated by the neural-net output (MLP_{lvbbqq}). A cut, $\mathrm{MLP}_{lvbbqq} > 0$, is applied to suppress the *lvbbqq* background, denoted by MLP2.

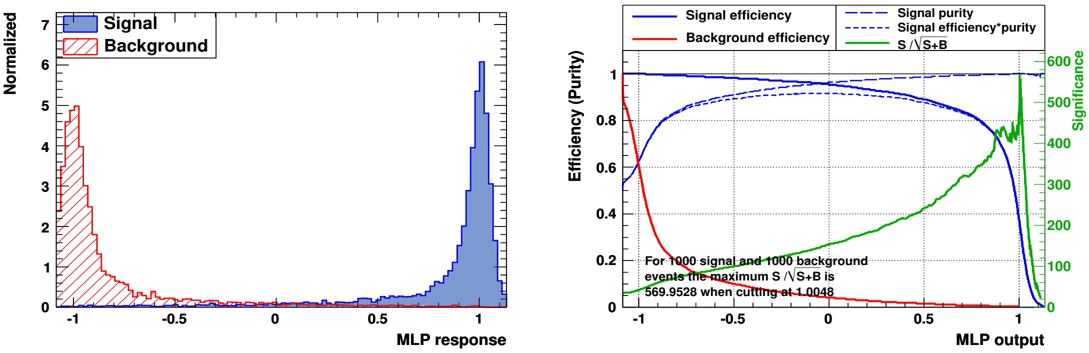

Figure 4.14: (left): The neural-net output for the signal versus the $lvbbqq$ background, where the blue histogram is for the signal and the red one is for $lvbbqq$. (right): The cut efficiencies of the signal and background at different cut values of the neural-net output, where the solid blue curve is for the signal and the red one is for $lvbbqq$ background.

4.3.4 Backgrounds with Same Final States

These backgrounds including $llbbbb$ and $llbbH$ mainly come from ZZZ and ZZH. Though their cross sections are not as large as the previous backgrounds, they have the same parton level final states as the signal, and, consequently, are more difficult to suppress. The quantities used in the previous neural-nets are of little use, requiring quantities related to the invariant mass and angular distributions to suppress them. For this purpose yet another neural-net is trained using the following quantities:

- Reconstructed Higgs mass. The two Higgs bosons masses should be the most discriminative to separate these backgrounds. The distributions of these two quantities are shown in Figure 4.16, respectively, denoted by "mh1" and "mh2".

- Reconstructed Z, H and Z, Z masses. In order to take maximal use of the mass information, in addition to the two Higgs boson masses reconstructed as from the signal process, the four jets are also paired as from the l^+l^-ZH and l^+l^-ZZ processes. The reconstructed Z and Higgs masses in the case of l^+l^-ZH pairing, though correlated with the two Higgs masses in the case of l^+l^-HH pairing, can offer some additional discriminative power to suppress the $llbbH$ background. The distributions of these reconstructed Z and Higgs masses are shown in Figure 4.16, respectively, denoted by "mzzh" and "mhzh". Similarly, the reconstructed two Z masses in the case of l^+l^-ZZ pairing are useful to suppress the $llbbbb$ background, distributions of which are shown in Figure 4.16, respectively, denoted by "mz1zz" and "mz2zz".

- t-channel characteristics. The processes $e^+ + e^- \to ZZZ$ and $e^+ + e^- \to ZZH$ are dominated by diagrams stem from the t-channel process $e^+ + e^- \to ZZ$, with one more Z strahlung from the electron line or one more Higgs strahlung from a Z, as shown in Figure 4.15. This feature makes the two Zs from emitted from the electron line ZZ move very fast and very forward. To effectively use this information, each event is re-reconstructed as from ZZZ or ZZH, and the boson candidate with the largest momentum among the three is identified for the both hypotheses. The largest momentum and its polar angle reflect the t-channel characteristics, distributions of which are shown in Figure 4.17, respectively, denoted by “p1zzz” and “cos1zzz”in case of ZZZ, “p1zzh” and “cos1zzh”in case of ZZH.

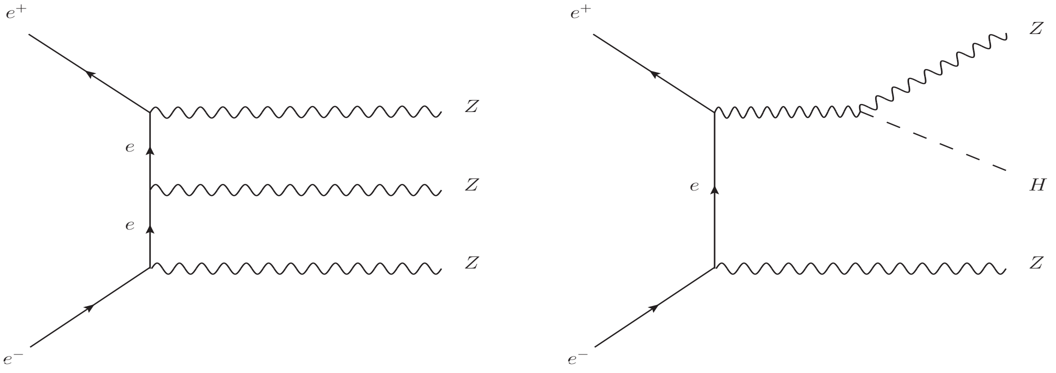

Figure 4.15: Typical Feynman diagrams for $e^+ + e^- \to ZZZ$ (left) and $e^+ + e^- \to ZZH$(right).

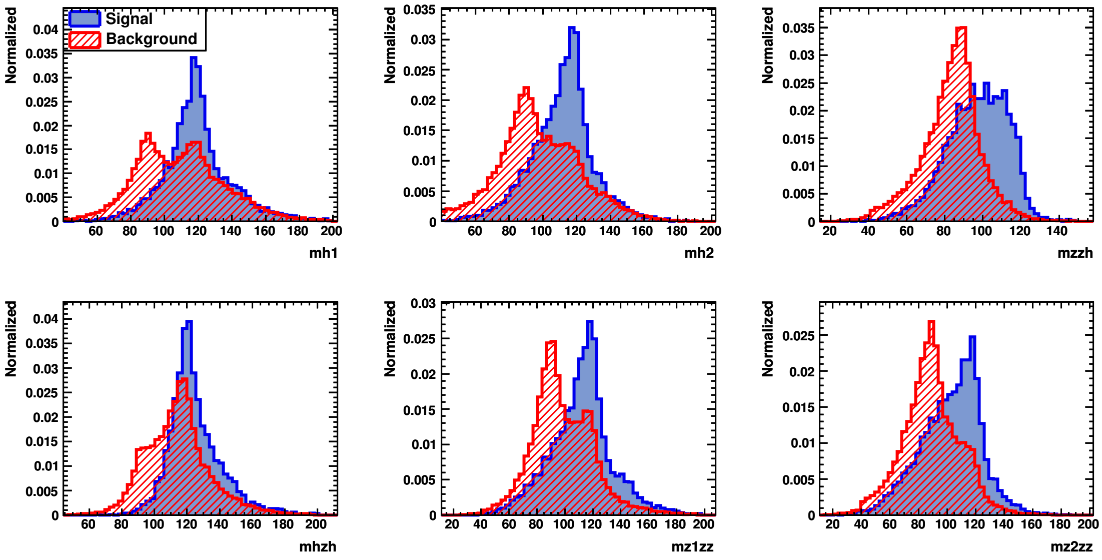

Figure 4.16: The discriminative quantities for the signal (blue) and the same final states backgrounds $llbbbb$, $llbbH$ (red). The variable names are explained in the text.

For the neural-net training, statistically independent llHH signal samples and the $llbbbb$ and $llbbH$ background samples are used, with each sample having statistics higher than 2 ab^{-1}. The neural-net outputs and cut efficiencies for the signal and backgrounds are shown in Figure 4.18. The $llbbbb$ and $llbbH$ backgrounds are not

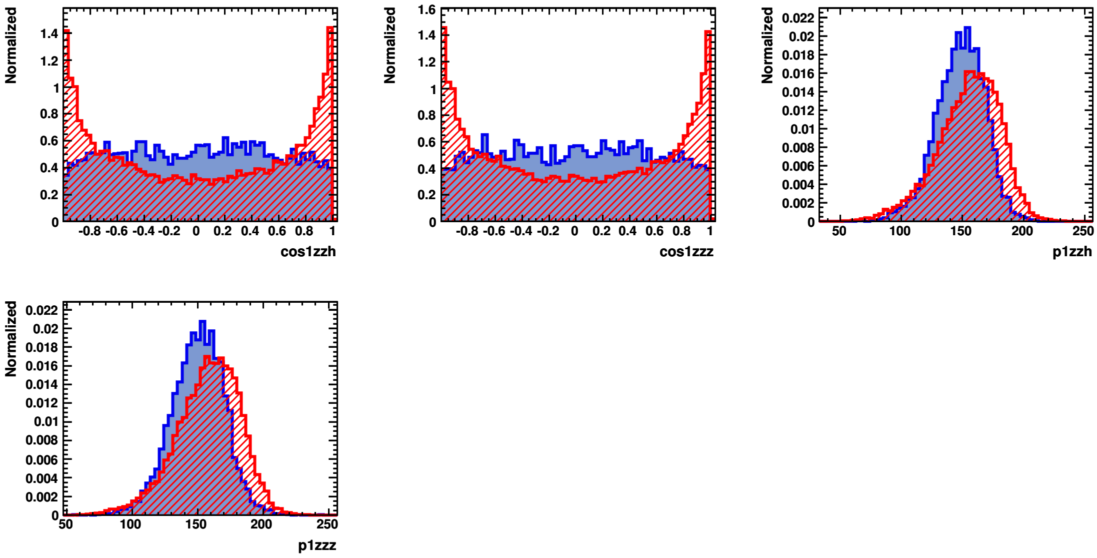

Figure 4.17: The discriminative quantities for the signal (blue) and the same final states backgrounds $llbbbb$, $llbbH$ (red). The variable names are explained in the text.

as well separated as the previous two backgrounds. A requirement to the neural-net output MLP$_{llbbbb} > -0.52$ is imposed to suppress the same final states background, denoted by MLP3. Because the two Higgs masses are the most discriminative quantities in this neural-net, this cut is also effective to suppress all the other backgrounds.

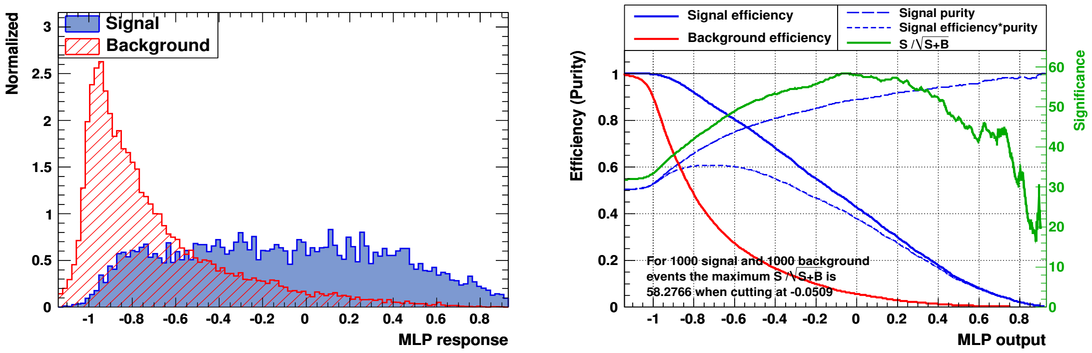

Figure 4.18: (left): The neural-net outputs for the signal and the $llbbbb$, $llbbH$ backgrounds, where the blue histogram is for the signal and the red one is for $llbbbb$ and $llbbH$. (right): The cut efficiencies for the signal and the background at different cut values on the neural-net output, where the solid blue curve is for the signal and the red one is for $llbbbb$, $llbbH$.

4.3.5 B tagging

Though the jets-poor backgrounds and the semi-leptonic backgrounds are significantly suppressed by the neural-net, the number of remaining background events is still much larger than that of the signal. On the other hand, so far we have only considered the backgrounds which contain at least two b quarks in the parton level final states. Information of flavour tagging can be used to eliminate the backgrounds with less than two b quarks, and further suppress the jets-poor and the semi-leptonic backgrounds.

As introduced in Chapter 3, the flavor tagging is handled by the LCFIVertex package. For each jet, three outputs (b-likeness, c-likeness and bc-likeness) are calculated. The signal mode is supposed to have four b jets. The b-likeness of the four jets are investigated. To make the difference between the signal and the background more significant, the four jets are ordered by the b-likeness from the largest to the smallest. The distributions of the four b-likeness values are shown in Figure 4.19, denoted by Bmax1, Bmax2, Bmax3 and Bmax4, where Bmax1 > Bmax2 > Bmax3 > Bmax4. One can see that Bmax1 is usually large and Bmax4 is usually small for both the signal and the backgrounds. Bmax2 and Bmax3 turn out to have the most discriminative power. The following cuts on Bmax2 and Bmax3, denoted by B tagging, are applied to suppress the backgrounds:

$$\text{Bmax2} > 0.62, \quad \text{Bmax3} > 0.24. \tag{4.11}$$

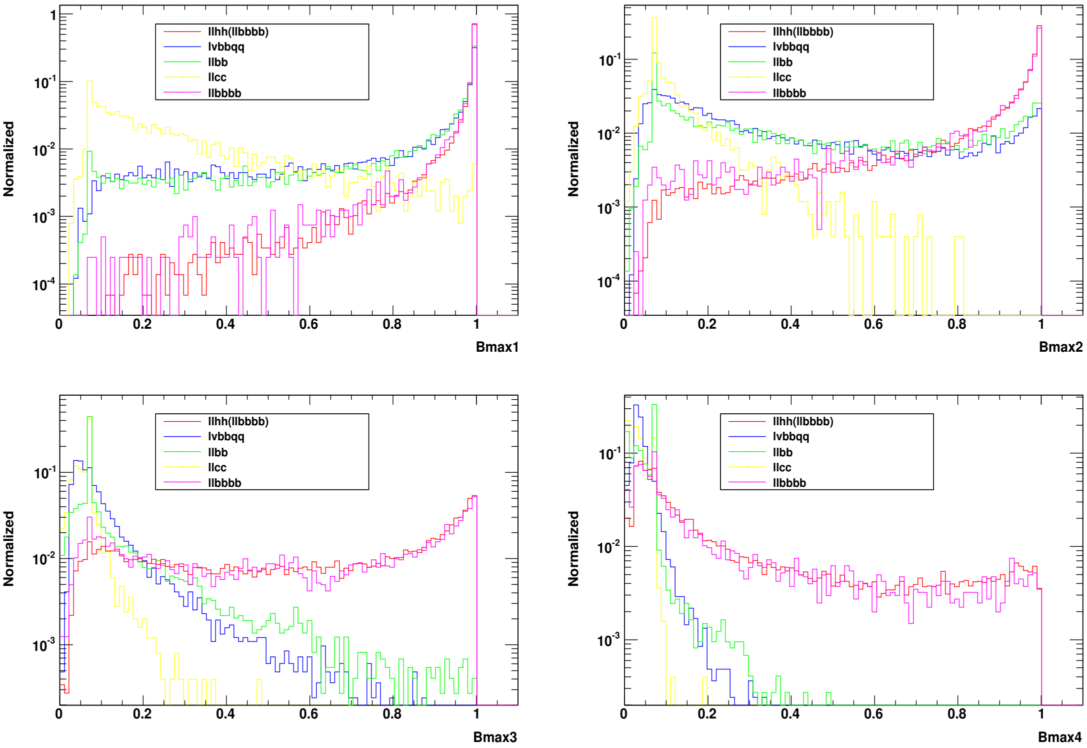

Figure 4.19: Distributions of the four b-likeness values, top left for Bmax1, top right for Bmax2, bottom left for Bmax3 and bottom right for Bmax4. Red histograms are for the signal, blue ones for the semi-leptonic background $lvbbqq$, the green and the yellow ones for the jets-poor backgrounds $llbb$ and $llcc$, and pink ones for the same final states background $llbbbb$.

4.4 Results

The number of the signal and background events remained after the final selection are shown in the reduction table 4.6 in the case of no beam polarization. As indicated, most of the backgrounds are eliminated, such as full hadronic backgrounds, semi-leptonic backgrounds and background without b parton, *llcc*. The remaining backgrounds are from *llbb*, *llbbbb*, *llqqH* and *llbbH*, and 3.8 events in total. This is to be compared with the 4.2 signal events that survived the final selection, with 3.9 events coming from *ll*HH → *llbbbb*.

Table 4.6: The reduction table for the signal and backgrounds after the final selection. The cuts names are explained in text.

Process	before selection	pre-selection	Cut1	MLP1	MLP2	B tagging	MLP3
*ll*HH (*llbbbb*)	21.2 (9.50)	17.4 (7.81)	16.0 (7.15)	11.8 (6.67)	11.4 (6.54)	5.40 (4.96)	4.24 (3.92)
bbcsdu	230600	328.5	0	0	0	0	0
bbuddu	116200	158	0	0	0	0	0
bbcssc	115600	167	0	0	0	0	0
bbbbbb	6.9	0.034	0	0	0	0	0
bbbb	23900	99.4	0.23	0	0	0	0
qqbb	183768	236	0	0	0	0	0
qqcc	103400	40.0	0	0	0	0	0
llbb	316000	12961	7423	38.7	36.8	1.51	0.52
llcc	1434800	12511	7012	105	104	0	0
$l\nu bbqq$	477600	8614	975	554	70.1	1.00	0
llbbbb	25.6	8.75	7.57	4.56	4.54	3.35	0.63
*llbb*H	20.1	17.0	15.9	12.0	11.7	7.14	2.04
*llqq*H	72.7	61.2	57.4	38.5	37.8	2.02	0.65

4.4.1 Significance

Given the expected numbers of the signal and backgrounds events, $N_S = 4.2$ and $N_B = 3.9$, the question is "what is the signal significance?"To be more precise, there are two questions to ask and hence two kinds of signal significance. One is how significantly we can observe the ZHH events, and the other is how significantly we can observe the Higgs self interaction, or what precision we can get on the Higgs trilinear self-coupling. For this *ll*HH mode, the first question is going to be answered. The second question will be discussed in Chapter 7, where three decay modes of ZHH are combined.

The two kinds of signal significances can be defined as follows:

(i) excess significance. Assuming there's only background, the p value is defined as the probability of observing events equal to or more than the number of the expected events, $N_S + N_B$:

$$p = \int_{N_S+N_B}^{\infty} f(x; N_B)\mathrm{d}x \tag{4.12}$$

where $f(x; N_B)$ is the probability density function for the number of observed events when only the background exists, with the expected number N_B. Here, the number of observed events is a Poisson random variable $f(n; N_B) = \frac{e^{-N_B}N_B^n}{n!}$, the p value is calculated as

$$p = \sum_{n=N_S+N_B}^{\infty} f(n; N_B) = 0.043 \tag{4.13}$$

corresponding to the significance:

$$1 - p = \int_{-\infty}^{s\sigma} N(x; 0, 1)\mathrm{d}x \tag{4.14}$$

where $N(x; 0, 1)$ is the normal gaussian probability density function. The significance $s\sigma$ is obtained 1.7σ. This definition of significance is called "excess significance". In the large statistics limit where if $f(x)$ becomes gaussian, this definition leads to the familiar significance formula $\frac{N_S}{\sqrt{N_B}}$.

(ii) measurement significance. Assuming both signal and background exist, the p value is defined as the probability of observing events equal to or less than the expected number of background events:

$$p = \int_{-\infty}^{N_B} f(x; N_B + N_S)\mathrm{d}x. \tag{4.15}$$

In this case, $p = 0.089$, corresponding to the significance of 1.3σ. This definition of significance is called "measurement significance". In the large statistics limit where if $f(x)$ becomes gaussian, this definition leads to the familiar significance formula $\frac{N_S}{\sqrt{N_S+N_B}}$.

4.4.2 Effects of Beam Polarization

As described in chapter 1, the electron beam can be polarized to 80% and the positron beam can be polarized to 30% at ILC. The different beam polarizations can enhance or suppress cross sections. The result shown above is in the case of no beam polarization. Additional two cases of beam polarization are checked to see the effect on signal significance: left handed polarization combination $\mathrm{P}(e^-, e^+) = (-80\%, +30\%)$, which enhances the signal cross section, and right handed polarization combination $\mathrm{P}(e^-, e^+) = (80\%, -30\%)$, which suppresses some background cross sections. The results of the three beam polarization cases are shown in Table 4.7. It turns out that the left handed polarization has the largest significances, benefiting from the enhanced signal cross section.

4.4.3 Cut Optimization

The cuts used above on the neural-net outputs and b-likeness are optimized jointly, to maximize signal significance, as shown in Figure 4.20. The third largest b-likeness and the neural-net output for the same final state backgrounds are the most sensitive to the significance.

Table 4.7: The remaining signal and background events for the three different polarization cases.

Final selection	no polarization	left handed	right handed
llHH	4.24	6.39	4.14
Background	3.84	6.74	3.00
significance (i)	1.7σ	2.1σ	1.9σ
significance (ii)	1.3σ	1.7σ	1.4σ
$llbb$	0.52	1.22	0.30
$llbbbb$	0.63	1.23	0.31
$llbb$H	2.04	3.25	1.80
$llqq$H	0.65	1.07	0.59

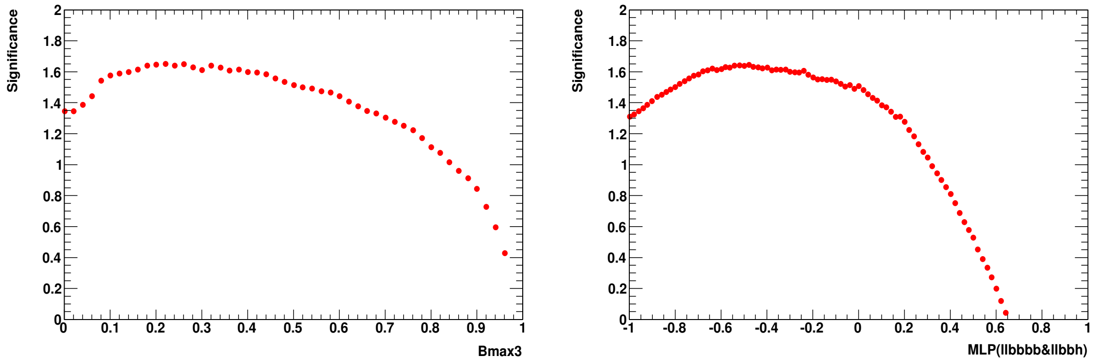

Figure 4.20: (left): The optimization of the cut on the third largest b-likeness Bmax3, denoted in the figure by “bmax3”. (right): The optimization of the cut on the neural-net output for the same final state backgrounds $llbbbb$ and $llbbH$.

4.4.4 Error on the expected numbers of signal and background events

Due to the limitation of MC statistics, there remain errors on the expected number of signal and background events after the final selection. For each process, let us assume the numbers of MC generated events before any selection and after the final selection are M_0 and M, and the expected number of events for that process is N_0. After the final selection, the expected number of observed events is $N = \frac{N_0 M}{M_0}$, and hence the error on N is $\delta N = \frac{N_0}{M_0}\delta M = \frac{N_0}{M_0}\sqrt{M} = \sqrt{\frac{N_0}{M_0}}\sqrt{N}$. The relative error is

$$\frac{\delta N}{N} = \sqrt{\frac{N_0}{M_0}}\frac{1}{\sqrt{N}}. \tag{4.16}$$

The relative error decreases as the square root of the MC sample size M_0. For instance, if $N = 5$ and we want a relative error $\frac{\delta N}{N} = 10\%$, then we need $M_0 = 20N_0$, that means the MC size should be 20 times of the expected number. However, for full simulation, it is not trivial to generate big enough MC samples. Typically, to generate a fully simulated event, it takes 1.5 minutes for detector simulation and another half minute for reconstruction. Table 4.8 shows the current errors on the expected numbers of signal and background events in the case of the left handed polarization, where the largest error comes from $llbb$.

Table 4.8: The expected numbers of the remaining signal and background events with errors in the case of the left handed polarization.

Final selection	left handed
llHH	6.39 ± 0.10
Background	6.74 ± 0.35
$llbb$	1.22 ± 0.32
$llbbbb$	1.23 ± 0.10
$llbb$H	3.25 ± 0.09
$llqq$H	1.07 ± 0.04

4.4.5 Summary of the llHH mode

In the search mode $e^+ + e^- \to l^+l^-$HH, assuming a Higgs mass of 120 GeV and an integrated luminosity of 2 ab^{-1} with the left handed beam polarization, it is expected to observe 6.4 signal events with 6.7 backgrounds events, corresponding to a ZHH excess significance of 2.1σ and a ZHH cross section measurement significance of 1.7σ.

Chapter 5

Full Simulation of $e^+ + e^- \to \nu\bar{\nu}HH \to \nu\bar{\nu}b\bar{b}b\bar{b}$ at 500 GeV

5.1 Signal and Backgrounds

In this search mode, the final state of a candidate signal event contains two missing neutrinos and four b quarks fragmenting into four jets. The three types of neutrinos ν_e, ν_μ and ν_τ are considered together. Most of the signal events come from the $e^+ + e^- \to$ ZHH process with only a small fraction of $\nu_e\bar{\nu}_e$HH events from the WW fusion process. At 500 GeV, the cross section of $e^+ + e^- \to \nu\bar{\nu}$HH without beam polarization is 33.8 ab, assuming the Higgs mass of 120 GeV. Though this cross section is about three times that of the llHH mode, it is still much smaller than those of most background processes. Corresponding to the integrated luminosity of 2 ab^{-1}, the expected number of signal $\nu\bar{\nu}$HH events is 67.7, of which 30.2 events lead to the $\nu\bar{\nu}b\bar{b}b\bar{b}$ final states.

Backgrounds having at least two b quarks are considered. The cross sections of all the considered background processes and the expected numbers of events assuming the integrated luminosity of 2 ab^{-1} are shown in Table 5.1. The corresponding numbers of generated MC events are also shown there. All the processes are labeled by their parton level final states.

5.2 Pre-selction

As for the pre-selction, conversely to the llHH mode, we first require there be no isolated charged leptons and then force all the PFOs to four jets and pair the four jets to two Higgs boson candidates.

5.2.1 Isolated Lepton Identification

The criteria for electron and muon identification are the same as used in Eqn. 4.1 and 4.4. However, the criteria of isolation requirements are slightly different from

Table 5.1: The cross sections and expected numbers of events for the signal and backgrounds without beam polarization at 500 GeV.

Process	Cross Section (fb)	Expected	MC
$e^+ + e^- \to \nu\bar{\nu}$HH	0.0338	67.7	45000
$e^+ + e^- \to bbcsdu$	115	230600	405727
$e^+ + e^- \to bbuddu$	58.1	116200	231600
$e^+ + e^- \to bbcssc$	57.8	115600	230701
$e^+ + e^- \to bbbb$	11.8	23900	414165
$e^+ + e^- \to qqbb$	91.8	183768	353715
$e^+ + e^- \to llbb$	158	316000	610502
$e^+ + e^- \to \nu\nu bb$	75.0	150000	30001
$e^+ + e^- \to e\nu bbqq$	79.6	159200	242851
$e^+ + e^- \to \mu\nu bbqq$	79.6	159200	241777
$e^+ + e^- \to \tau\nu bbqq$	79.6	159200	1815503
$e^+ + e^- \to \nu\nu bbbb$	0.0252	50.5	30000
$e^+ + e^- \to \nu\nu bb$H	0.0300	60.0	23670

Eqn 4.2 and 4.5. In this search mode, the isolated lepton rejection is mainly used to suppress the semi-leptonic backgrounds $l\nu bbqq$. So the electron and muon isolation requirements here are optimized to discard $e\nu bbqq$ and $\mu\nu bbqq$ events, respectively, as shown in Figure 5.1 and 5.2. The isolation requirement for electron is

$$P - 0.55E_{\text{cone}} > 19.8 \text{ GeV} \tag{5.1}$$

and that for muon is

$$P - 0.24E_{\text{cone}} > 22.3 \text{ GeV}. \tag{5.2}$$

Together with the requirements Eqn. 4.1 for electron and Eqn. 4.4 for muon, about 80% of prompt electrons from $e\nu bbqq$ and prompt muons from $\mu\nu bbqq$ are identified, while about 10% of the signal $\nu\nu$HH events are left with one or more isolated charged leptons. After the requirement that there should be no isolated charged lepton, 80% of the $e\nu bbqq$ and $\mu\nu bbqq$ events are eliminated with 90% of the signal events kept.

5.2.2 Jet Clustering and Jet Pairing

Following the no-isolated-charged-lepton requirement, all the PFOs are forced to four jets by using the Durham jet clustering algorithm. Then the four jets j_1, j_2, j_3 and j_4 are combined to two pairs. Among all the possible combinations, the one which minimizes the χ^2 (Eqn. 4.7) is selected. The two jet-pairs are reconstructed as two Higgs bosons, respectively, with invariant masses $M(j_1, j_2)$ and $M(j_3, j_4)$. In pairing, loose cuts on the $M(j_1, j_2)$ and $M(j_3, j_4)$ are applied:

$$|M(j_1, j_2) - M(H)| < 80 \text{ GeV}, \quad |M(j_3, j_4) - M(H)| < 80 \text{ GeV}. \tag{5.3}$$

5.2.3 B tagging requirement

In this search mode, a tight b tagging requirement is used in the pre-selection: at least three jets have to have the b-likeness no less than 0.3. Consequently, shown in

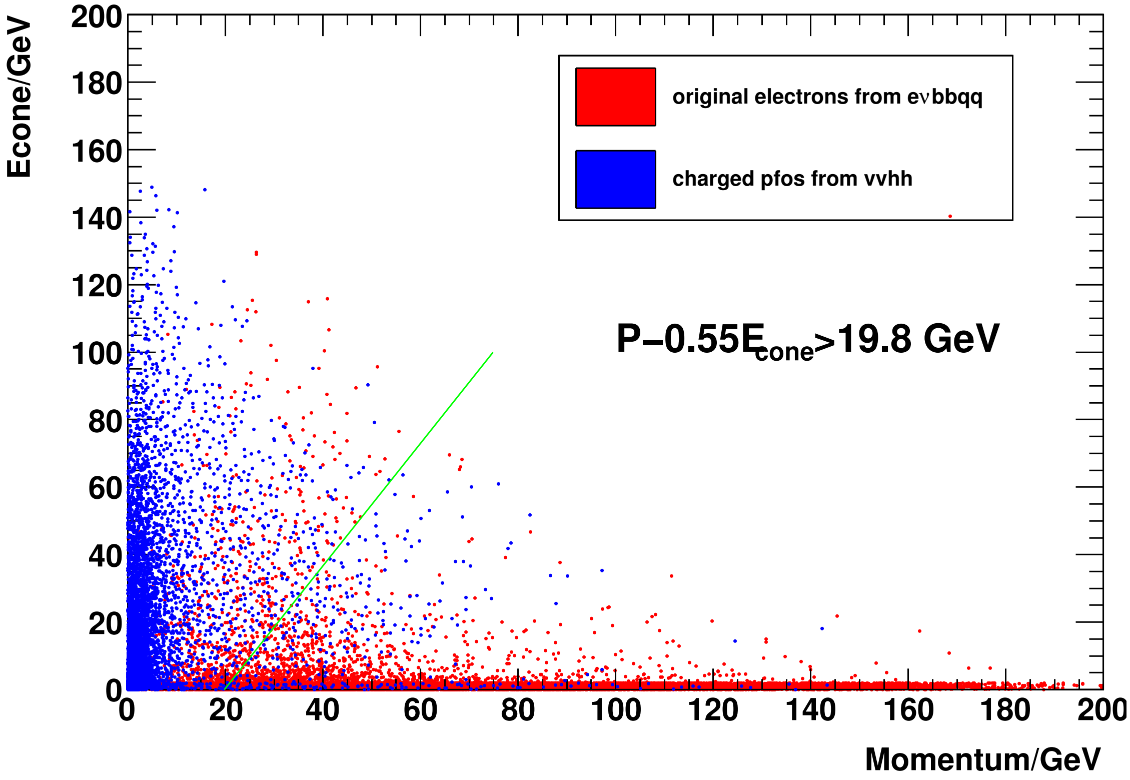

Figure 5.1: Scatter plot of the charged cone energy versus the momentum for PFOs in the $\nu\nu$HH and $e\nu bbqq$ samples. Red points are prompt electrons from $e\nu bbqq$ and blue ones are charged PFOs from $\nu\nu$HH.

Table 5.2, the remaining signal events mainly come from $\nu\nu$HH $\to \nu\nu bbbb$.

5.3 Final Selection

The signal and background events after the pre-selection are shown in Table 5.2. In general, the event selection strategy used for $\nu\nu$HH is similar to that for llHH. The full hadronic backgrounds, such as $bbcsdu$, $bbuddu$ and $bbcssc$ are suppressed by cuts on the missing energy and missing P_t (transverse momentum). However, $bbbb$ might be an important additional background because they are not significantly suppressed by the b tagging. The jets-poor background $\nu\nu bb$ turns out to be not very important due to the tighter b tagging requirement. The $\tau\nu bbqq$ background is dominant, not only because they have missing neutrinos, but also because the secondary vertex of the tau can make the b tagging requirement less effective. The suppression of the same final state backgrounds $\nu\nu bbbb$ and $\nu\nu bbH$ is almost the same as in the llHH mode.

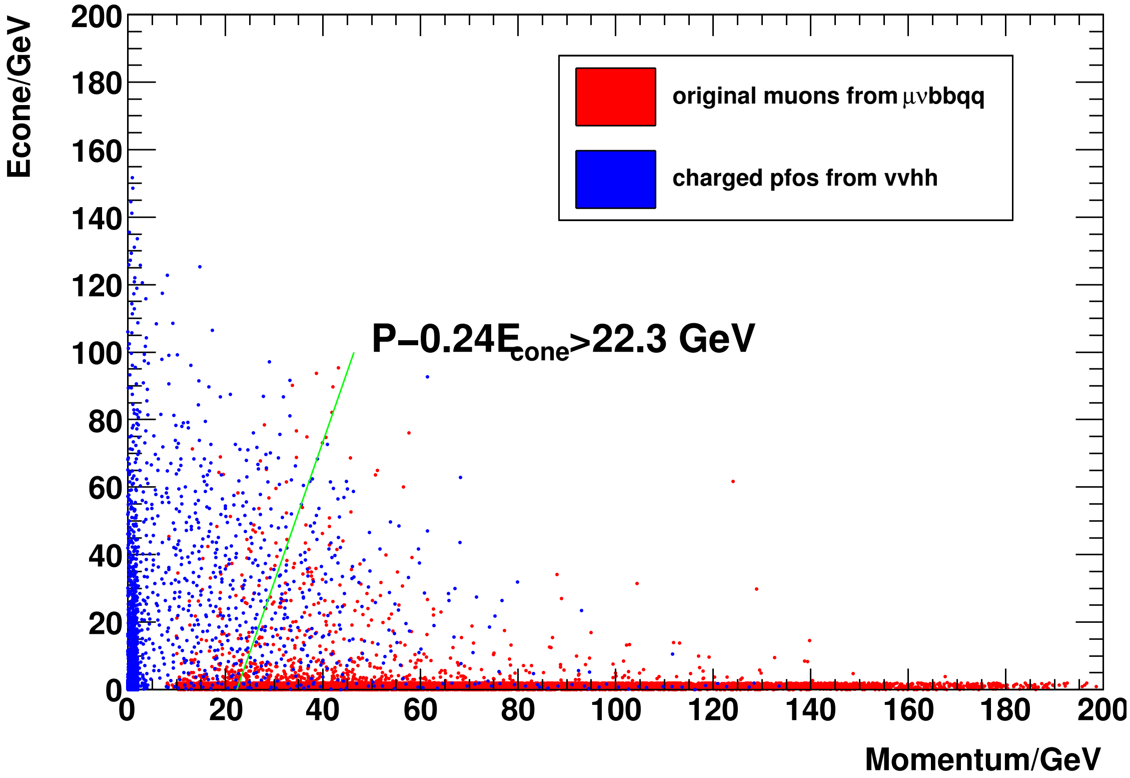

Figure 5.2: Scatter plot of the charged cone energy versus the momentum for PFOs in the $\nu\nu$HH and $\mu\nu bbqq$ samples. Red points are prompt muons from $\mu\nu bbqq$ and blue ones are charged PFOs from $\nu\nu$HH.

5.3.1 Full Hadronic Backgrounds

The full hadronic backgrounds, *bbcsdu*, *bbuddu*, *bbcssc*, *qqbb* and *bbbb*, mostly come from $e^+ + e^- \to t\bar{t}$, WWZ and ZZ. They are not significantly suppressed by the pre-selection other than the b-tagging. Because there are two prompt missing neutrinos in the signal events, the visible energy and missing P_t can offer the discriminative power. Figure 5.3 shows the scatter plot of missing P_t (MissPt) and visible energy (Evis) for the signal and the full hadronic backgrounds. Using Fisher classification, we decided to require

$$\text{Evis} - 0.83\text{MissPt} < 350\ GeV. \tag{5.4}$$

In addition, because the signal event has two missing neutrinos from the Z decay, missing energy is required to be greater than missing momentum, MissE > MissPt. The full hadronic backgrounds are significantly suppressed by these two cuts, which are denoted by Cut1, as shown in Table 5.3. However, the numbers of remaining *bbbb* and *qqbb* background events are still very large. Their further suppression is carried out by a neural-net as described in the following section.

Table 5.2: The numbers of the signal and background events after pre-selection without beam polarization. The second line for the $\nu\nu$HH signal in parentheses show the contribution of $\nu\nu bbbb$ decaying from $\nu\nu$HH.

Process	before selection	pre-selection
$e^+ + e^- \to \nu\nu$HH ($\nu\nu bbbb$)	67.7 30.2	22.9 21.7
$e^+ + e^- \to bbcsdu$	230600	10775
$e^+ + e^- \to bbuddu$	116200	1526
$e^+ + e^- \to bbcssc$	115600	10028
$e^+ + e^- \to bbbb$	23900	13857
$e^+ + e^- \to qqbb$	183768	12546
$e^+ + e^- \to llbb$	316000	3109
$e^+ + e^- \to \nu\nu bb$	150000	4015
$e^+ + e^- \to e\nu bbqq$	159200	1301
$e^+ + e^- \to \mu\nu bbqq$	159200	1289
$e^+ + e^- \to \tau\nu bbqq$	159200	13327
$e^+ + e^- \to \nu\nu bbbb$	50.5	33.2
$e^+ + e^- \to \nu\nu bb$H	60.0	29.4

Table 5.3: The numbers of the signal and the full hadronic background events after requiring Evis – 0.83MissPt < 350 and MissE > MissPt, denoted by Cut1.

Process	before selection	pre-selection	Cut1
$e^+ + e^- \to \nu\nu$HH ($\nu\nu bbbb$)	67.7 30.2	22.9 21.7	21.8 20.7
$e^+ + e^- \to bbcsdu$	230600	10775	120
$e^+ + e^- \to bbuddu$	116200	1526	19.1
$e^+ + e^- \to bbcssc$	115600	10028	139
$e^+ + e^- \to bbbb$	23900	13857	1369
$e^+ + e^- \to qqbb$	183768	12546	1827

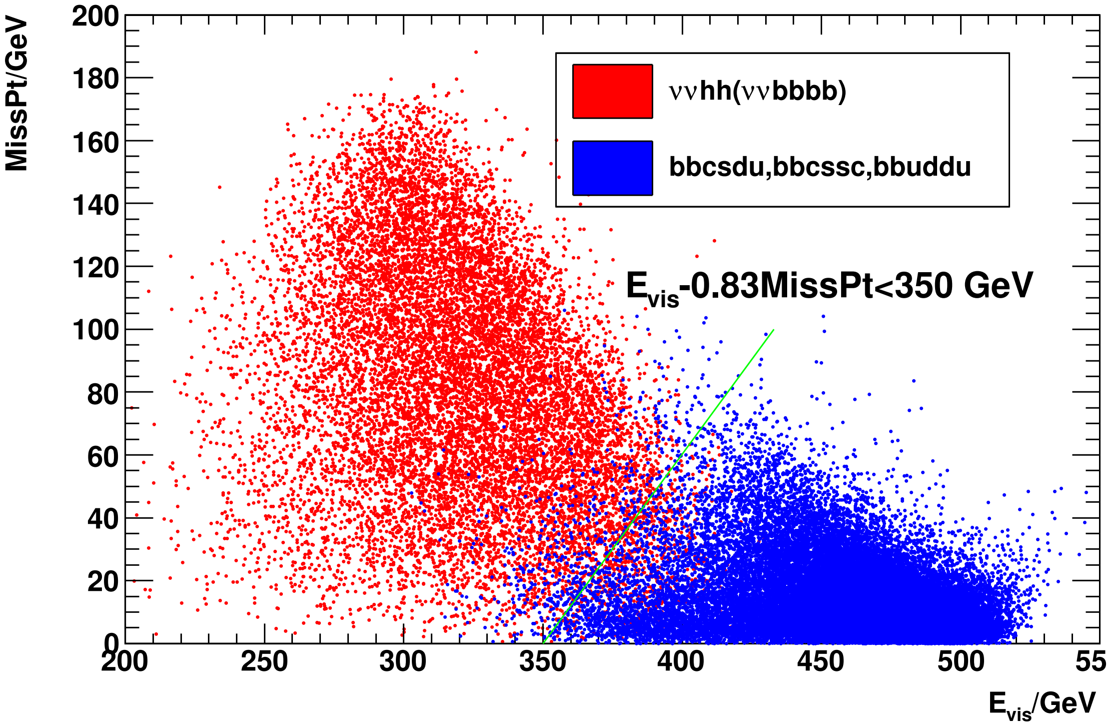

Figure 5.3: Scatter plot of missing P_t versus visible energy for the signal (red) and the full hadronic backgrounds (blue).

5.3.2 Jets-Poor Backgrounds

The jets-poor background here refers to $\nu\nu bb$, which mainly comes from ZZ, ZZ^*, $b\bar{b}Z$ and $\nu\bar{\nu}Z$. Due to the much tighter b tagging in this search mode, the contamination from the $\nu\nu bb$ background is not as significant as from $llbb$ in the llHH mode. Instead of neural-net training, several cuts are employed to suppress this background:

- The number of PFOs in each jet is at least 8, npfosmin >= 8.
- The $Y_{4\to3}$ value is required to be greater than 0.002, $Y_{4\to3} > 0.002$.
- The invariant mass of all the PFOs, equivalent to the invariant mass of two Higgs bosons, denoted by "mhh", is required to be greater than 200 GeV, mhh > 200. This cut is to suppress the $\nu\bar{\nu}Z$ contribution of $\nu\nu bb$, where the invariant mass of all the PFOs should be equal to the mass of the Z boson.

After these three requirements, which are denoted by Cut2, the $\nu\nu bb$ background is significantly suppressed, as shown in Table 5.4.

5.3.3 *bbbb* background

As mentioned above, the *bbbb* background is still very large after the missing energy cut and that the b tagging is ineffective for this background. A neural-net is hence trained to further suppress this, by using the following discriminative quantities:

Table 5.4: The numbers of the signal and the $\nu\nu bb$ background events after Cut2 explained in text.

Process	before selection	pre-selection	Cut1	Cut2
$e^+ + e^- \to \nu\nu$HH	67.7	22.9	21.8	19.5
($\nu\nu bbbb$)	30.2	21.7	20.7	18.8
$e^+ + e^- \to \nu\nu bb$	150000	4015	3920	30.0

- Visible energy and missing P_t. Because the cuts Eqn 5.4 is optimized for $bbcsdu$, $bbuddu$ and $bbcssc$ backgrounds, the information of visible energy and missing P_t can still be usefull. Distributions of these two quantities are shown in Figure 5.4, respectively denoted by "evis" and "mpt".
- Thrust. The $bbbb$ background mainly comes from two body processes. Thrust is much larger than that of the signal, as indicated in Figure 5.4, which is denoted by "pthrust".
- Reconstructed Z mass. The four jets are paired as from ZZ. Reconstructed invariant masses of the two Z bosons are very discriminative. Distributions of these two Z masses are shown in Figure 5.4, denoted by "mz1zz" and "mz2zz". The peaks of invariant masses are not at the true Z mass, because the criterion Eqn 5.4 requires large missing energy, resulting in the shift of the invariant mass toward the low end.
- Largest jet momentum of the four jets. The distribution of this quantity is shown in Figure 5.4, denoted by "pjmax".

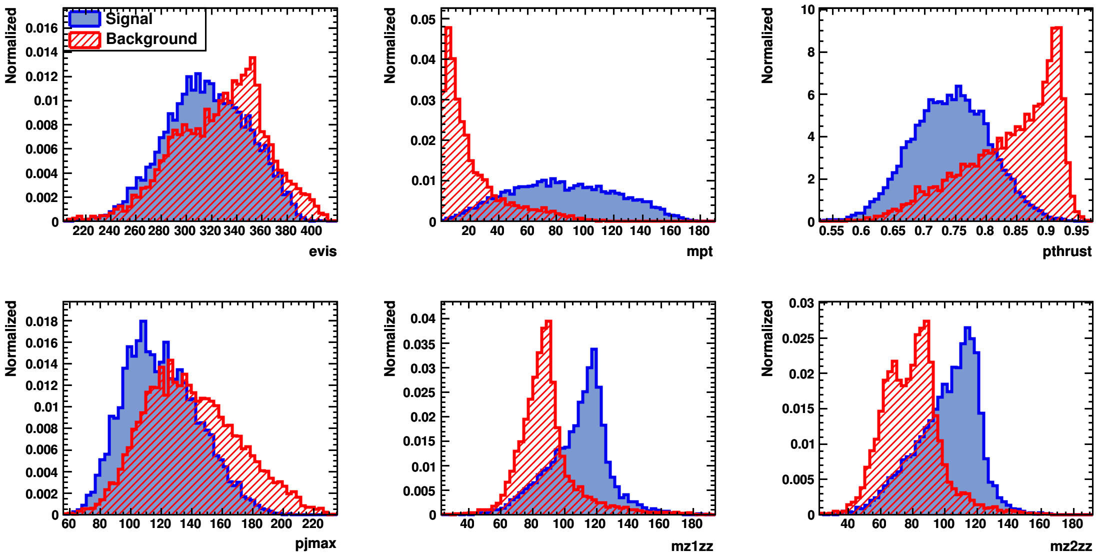

Figure 5.4: Discriminative quantities for the signal (blue) and the $bbbb$ backgrounds (red). The variable labels are explained in the text.

By using these quantities as input variables, a neural-net is trained for the signal and the $bbbb$ background after Cut1. For the neural-net, an additional statistically independent $\nu\bar{\nu}$HH signal sample and *bbbb* background sample with statistics higher than 2 ab^{-1} are used. The neural-net outputs and cut efficiencies for the signal and the background are shown in Figure 5.5. The *bbbb* background is well separated by the neural-net output (MLP$_{bbbb}$). A cut, MLP$_{bbbb} > 0.6$, is applied to further suppress the *bbbb* background, which is denoted as MLP1. Though the neural-net is trained for *bbbb*, the *qqbb* background is also significantly suppressed by MLP1.

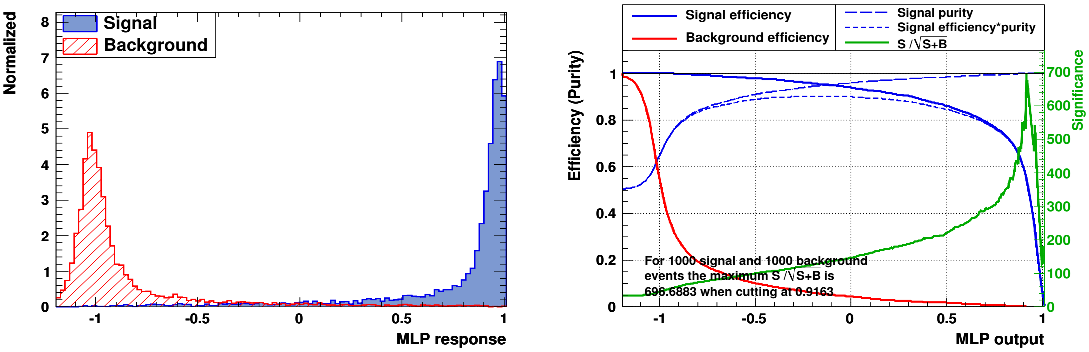

Figure 5.5: (left): The neural-net output for the signal versus the *bbbb* background, where the blue histogram is for the signal and the red one is for *bbbb*. (right): The cut efficiencies of the signal and background at different cut values on the neural-net output, where the solid blue curve is for the signal and the red one is for *bbbb*.

5.3.4 Semi-leptonic Backgrounds

The semi-leptonic backgrounds including $e^-\bar{\nu}b\bar{b}c\bar{s}$, $e^-\bar{\nu}b\bar{b}u\bar{d}$ and corresponding muon and tau modes, and their charge conjugate modes, are mainly from $t\bar{t}$ and W^+W^-Z. The $e\nu bbqq$ and $\mu\nu bbqq$ processes are suppressed by the no-isolated-charged-lepton requirement. However, as mentioned before, the $\tau\nu bbqq$ processes, especially $\tau\nu bbcs$, where the τ and c jets can be mis-tagged as b jets, comprises the dominant background. It is really challenging to suppress them effectively, considering the large cross sections of these backgrounds. Another neural-net is thus trained for the semi-leptonic backgrounds using the following quantities:

- Missing mass. For the signal, the missing invariant mass should be consistent with a Z boson, though the line-shape is skewed by beamstrahlung, initial state radiation and missing neutrinos from decays of heavy flavored hadrons. The distribution of this quantity, denoted by “mz”, is shown in Figure 5.7.
- Largest momentum of charged leptons and its cone energy. After the pre-selection, there are still some backgrounds with isolated electrons or muons that survived Cut1. To use this information, the electrons and muons are identified by the Eqn 4.1 and 4.4 without the isolation requirement and then from all the electrons and muons so identified, the one with largest momentum is selected. The momentum and the cone energy of this lepton can offer some discriminative power to separate the backgrounds from $e\nu bbqq$, $\mu\nu bbqq$ and part of $\tau\nu bbqq$ with the *tau* decaying into e or μ. Distributions of these two

quantities are shown in Figure 5.6, denoted, respectively, by “plmax” and “econlmax”.

- Largest momentum of charged PFOs and its angle to the nearest jet. Complementary to the previous quantities about leptons, because some τ decays into one charged energetic π, it is helpful to find the largest momentum of all the charged PFOs. Such a charged π from τ tends to be isolated from other particles. Distributions of these two quantities are shown in Figure 5.8, denoted, respectively, by “pcmax” and “coscjmax”.
- Angle between two b jets as in the llHH mode. The distribution of this quantity, denoted by “cosbmax”, is shown in Figure 5.7.
- The total number of PFOs as in the llHH mode. The distribution of this quantity, denoted by “npfos”, is shown in Figure 5.8.
- Reconstructed W mass as in the llHH mode. The distribution of this quantity, denoted by “mwtt4j”, is shown in Figure 5.6.
- Two invariant masses of reconstructed Higgs bosons. The distribution of these two masses are shown in Figure 5.7 − 5.8, denoted by “mh1” and “mh2”.
- Quantities obtained by reconstructing the event as five jets from $\tau\nu bbqq$. The jet which has the smallest number of PFOs is regarded as the τ jet, the two out of the remaining four jets with the largest and second largest b-likeness are taken as the two b jets. The left two jets are assumed to be from a W decay. The W candidate and one of the two b jets are combined to form a top, where we have two combinations. The reconstructed W mass, the top mass, the τ mass, and the number of PFOs in the τ jet can offer some discriminative power to separate the $\tau\nu bbqq$ background. Distributions of these quantities are shown in Figure 5.6 − 5.8, respectively, denoted by “mwtt5j”, “mt1tt5j”, “mt2tt5j”, “mjminjets5” and “npminjets5”.

By using these quantities as input variables, yet another neural-net is trained for the signal and the $l\nu bbqq$ background. For the neural-net training, a statistically independent $\nu\bar{\nu}$HH signal sample and the $l\nu bbqq$ background sample with statistics higher than 2 ab^{-1} are used. The neural-net outputs and cut efficiencies for the signal and the background are shown in Figure 5.9. The $lvbbqq$ background is not as well separated as $bbbb$ and hence a tight cut (denoted by MLP1) on the neural-net output (MLP$_{lvbbqq}$) is necessary to significantly suppress the $l\nu bbqq$ background: MLP$_{lvbbqq}$ > 0.42.

5.3.5 Backgrounds with Same Final States

The $llbbbb$ and $llbbH$ backgrounds, coming from ZZZ and ZZH, have the same final states as the signal. The strategy to suppress them is the same as that in the llHH modes. The following quantities are used for the neural-net training, distributions of which are shown in Figure 5.10 − 5.11:

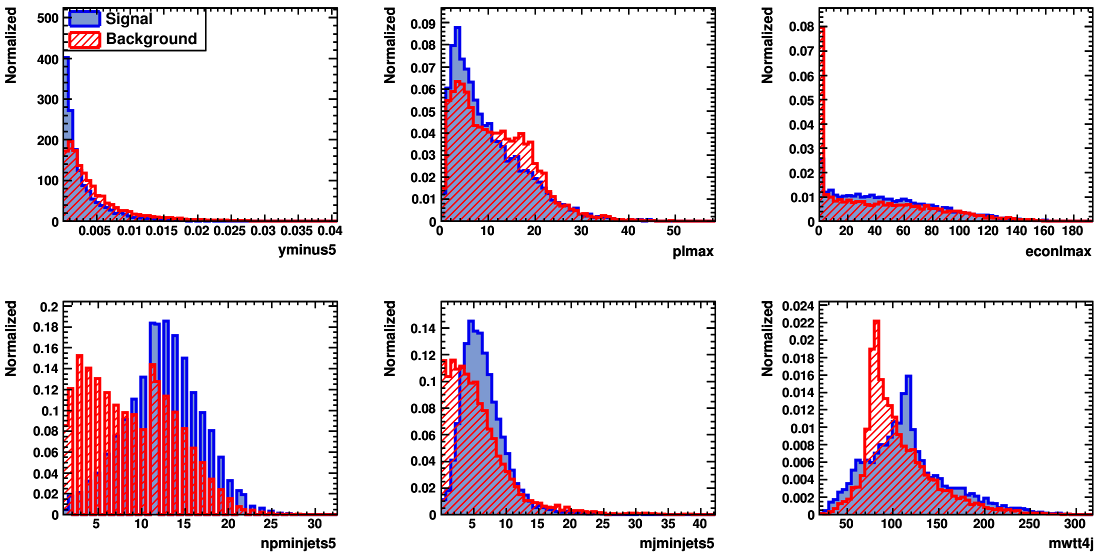

Figure 5.6: Discriminative quantities for the signal (blue) and the semi-leptonic backgrounds $lvbbqq$ (red). The variable names are explained in the text.

- Reconstructed Z and Higgs masses calculated with the $\nu\bar{\nu}ZH$ hypothesis, denoted by “mzzh” and “mhzh”.
- Two reconstructed Z masses with the $\nu\bar{\nu}ZZ$ hypothesis, denoted by “mz1zz” and “mz2zz”.
- Quantities reflecting t-channel characteristics such as the largest momentum of the three bosons reconstructed as from $\nu\bar{\nu}ZH$, where the missing momentum is reconstructed as from one Z boson, and the polar angle of the highest momentum boson, denoted by “p1stzzh” and “cos1stzzh”. Similarly for the $\nu\bar{\nu}ZZ$ hypothesis, we calculate the largest momentum “p1stzzz” and its polar angle “cos1stzzz”.

For the neural-net training, a statistically independent $\nu\nu$HH signal sample and $\nu\nu bbbb$, $\nu\nu bbH$ background samples are used, each with statistics higher than 2 ab^{-1}. The neural-net outputs and the cut efficiencies for the signal and the backgrounds are shown in Figure 5.12. A cut on the neural-net output, denoted by MLP3, $\mathrm{MLP}_{\nu\nu bbbb} > -0.18$ is applied to suppress the same final state backgrounds, .

5.3.6 B tagging

Similar to the b tagging in the llHH mode, the four jets are ordered in the descending order of the b-likeness values: Bmax1, Bmax2, Bmax3 and Bmax4. For the preselection, Bmax3 is required to be no less than 0.3, but now tighter cuts on Bmax3 and Bmax4 are imposed

$$\mathrm{Bmax3} + \mathrm{Bmax4} > 1.15 \tag{5.5}$$

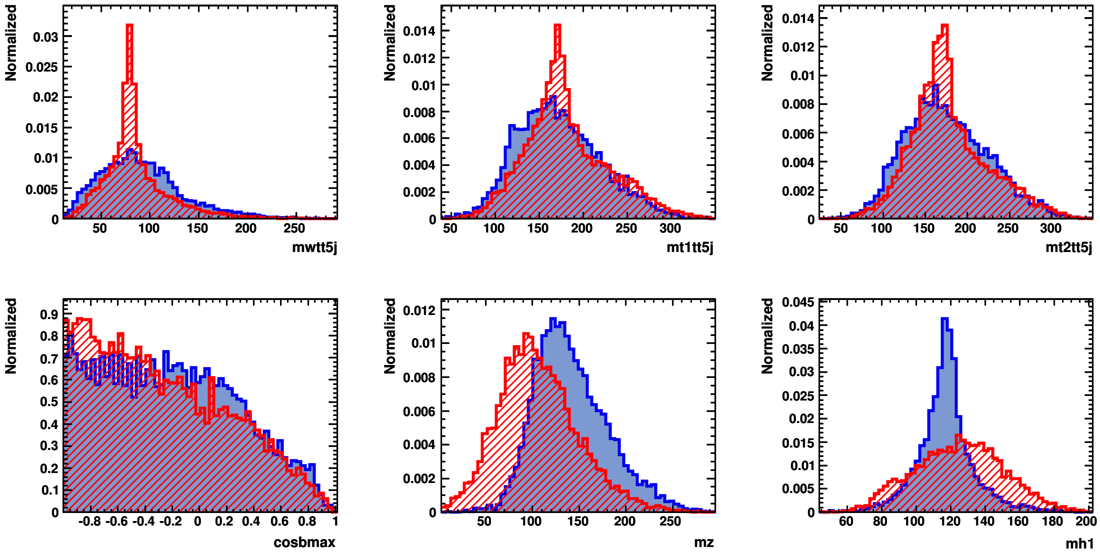

Figure 5.7: Discriminative quantities for the signal (blue) and the semi-leptonic backgrounds $lvbbqq$ (red). The variable names are explained in the text.

5.4 Results

The numbers of the signal and background events remained after the final selection are shown in Table 5.5 in the case of no beam polarization. As indicated, most of the backgrounds, such as the full hadronic backgrounds $bbcsdu$, the jets-poor background $\nu\nu bb$ and the semi-leptonic backgrounds $e\nu bbqq$, are eliminated. The remaining backgrounds are $bbbb$, $\tau\nu bbqq$, $\nu\nu bbbb$, and $\nu\nu bbH$, and amount to 3.5 events. This is to be compared with the 3.3 signal events that survived the final selection, almost all of which come from $\nu\nu$HH decaying into $\nu\nu bbbb$.

5.4.1 Significance and Effects of Beam Polarization

The above result is for no beam polarization. The significance and the result for the left-handed beam polarization are shown in Table 5.6. As with the llHH mode, the left handed beam polarization gives a larger significance.

5.4.2 Cut Optimization

For the left handed beam polarization, the cuts used above on the neural-net outputs and the b tagging are optimized jointly, to maximize the signal significance, as shown in Figure 5.13.

5.4.3 Error on the expected numbers of signal and background events

As with the llHH mode, due to the limitation of MC statistics, there are errors on the expected numbers of the signal and the background events after the final

Table 5.5: Reduction table for the signal and backgrounds after the final selection. The cut names are explained in the text. In the first line, Cut0 means the pre-selection and "Expected"means the expected number of events before any selection.

Process	Expected	Cut0	Cut1	Cut2	MLP1	MLP2	MLP3	B tagging
$\nu\nu$HH	67.7	22.9	21.8	19.5	16.7	9.88	8.09	3.31
($\nu\nu bbbb$)	30.2	21.7	20.7	18.8	16.1	9.66	7.92	3.30
$bbcsdu$	230600	10775	120	119	21.6	5.12	5.12	0
$bbuddu$	116200	1526	19.1	18.1	2.51	0	0	0
$bbcssc$	115600	10028	139	136	23.0	4.00	4.00	0
$bbbb$	23900	13857	1369	1045	12.7	3.80	2.66	0.86
$qqbb$	183768	12546	1827	968	33.8	13.5	13.5	0
$llbb$	316000	3109	145	7.69	0.53	0	0	0
$\nu\nu bb$	150000	4015	3920	30.0	20.0	0	0	0
$e\nu bbqq$	159200	1301	829	678	488	11.0	7.00	0
$\mu\nu bbqq$	159200	1289	967	841	606	19.0	15.0	0
$\tau\nu bbqq$	159200	13327	8942	5865	3892	181	133	1.39
$\nu\nu bbbb$	50.5	33.2	32.5	22.3	13.0	3.91	1.04	0.29
$\nu\nu bb$H	60.0	29.4	28.5	24.9	19.0	6.63	2.54	0.97

Table 5.6: The numbers of the remaining signal and background events for the different beam polarization cases and corresponding significances.

Final selection	no polarization	left handed
$\nu\nu$HH	3.31	5.21
Background	3.51	7.00
significance (i)	1.4σ	1.7σ
significance (ii)	1.1σ	1.4σ
$bbbb$	0.86	1.62
$\tau\nu bbqq$	1.39	3.25
$\nu\nu bbbb$	0.29	0.63
$\nu\nu bb$H	0.97	1.50

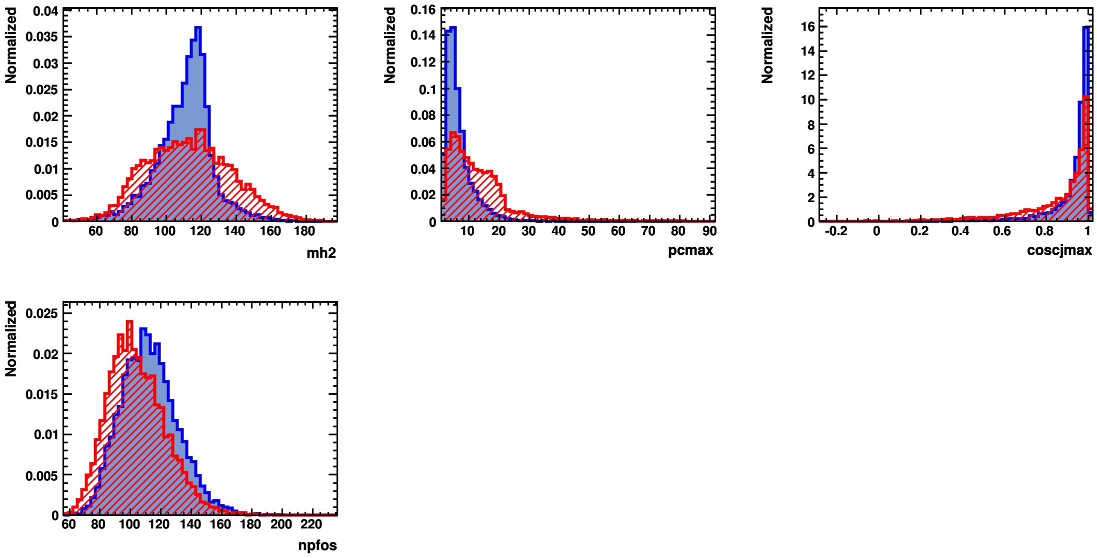

Figure 5.8: Discriminative quantities for the signal (blue) and the semi-leptonic backgrounds $l\upsilon bbqq$ (red). The variable names are explained in the text.

selection, as shown in Table 5.7 for the left handed polarization. The largest error comes from the $\tau\nu bbqq$ and $bbbb$ samples.

Table 5.7: The expected numbers of the remaining signal and background events with errors in the case of the left handed polarization.

Final selection	left handed
$\nu\nu$HH	5.21 ± 0.15
Background	7.00 ± 0.73
$bbbb$	1.62 ± 0.41
$\tau\nu bbqq$	3.25 ± 0.59
$\nu\nu bbbb$	0.63 ± 0.10
$\nu\nu bb$H	1.50 ± 0.08

5.4.4 Summary of the $\nu\nu$HH mode

In the $e^+ + e^- \to \nu\bar{\nu}$HH search mode, assuming the Higgs mass of 120 GeV, the integrated luminosity of 2 ab^{-1}, and the left handed beam polarization, which is favored, it is expected to observe 5.2 signal and 7.0 backgrounds events, corresponding to a ZHH excess significance of 1.7σ and a ZHH cross section measurement significance of 1.4σ.

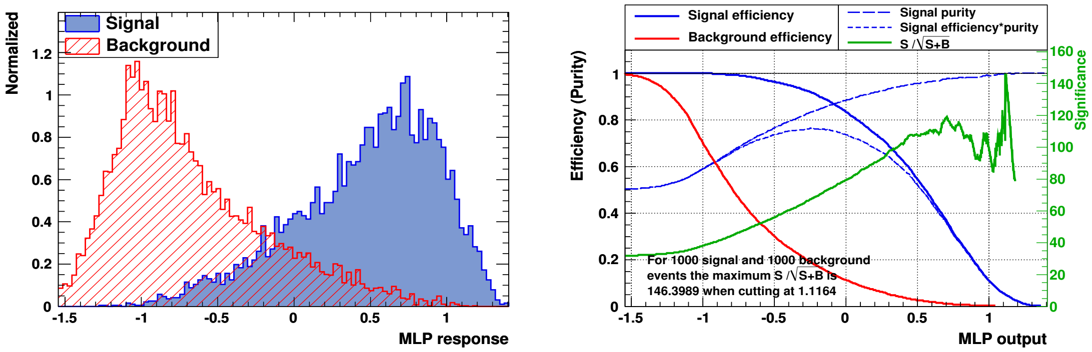

Figure 5.9: (left): The neural-net output for the signal versus the $l\nu bbqq$ background, where the blue histogram is for the signal and the red one is for the $l\nu bbqq$ background. (right): The cut efficiencies of the signal and background at different cut values on the neural-net output, where the solid blue curve is for the signal and the red one is for the $l\nu bbqq$ background.

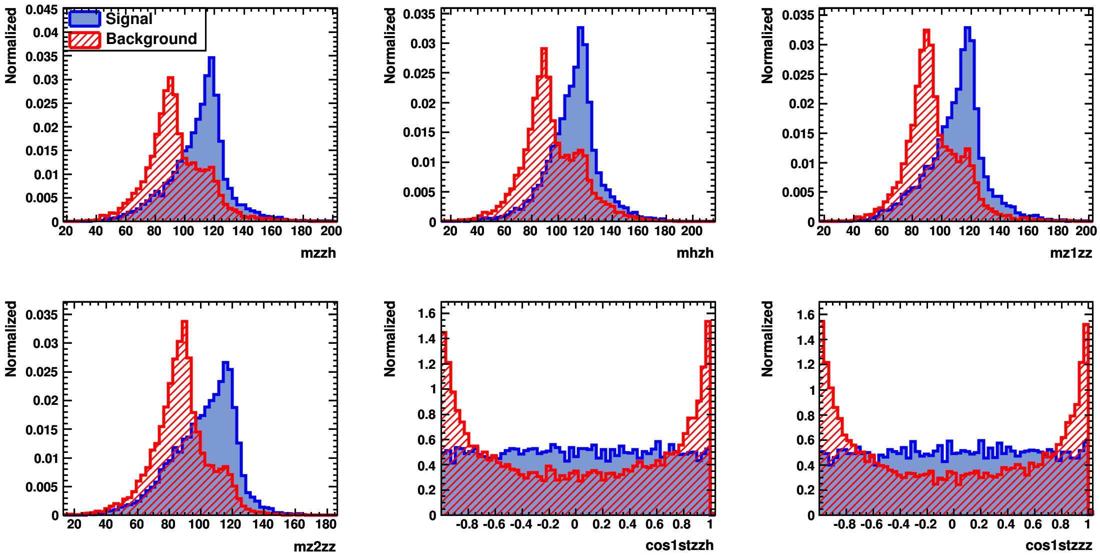

Figure 5.10: Discriminative quantities for the signal (blue) and the same final states backgrounds $\nu\nu bbbb$, $\nu\nu bbH$ (red). The variable names are explained in the text.

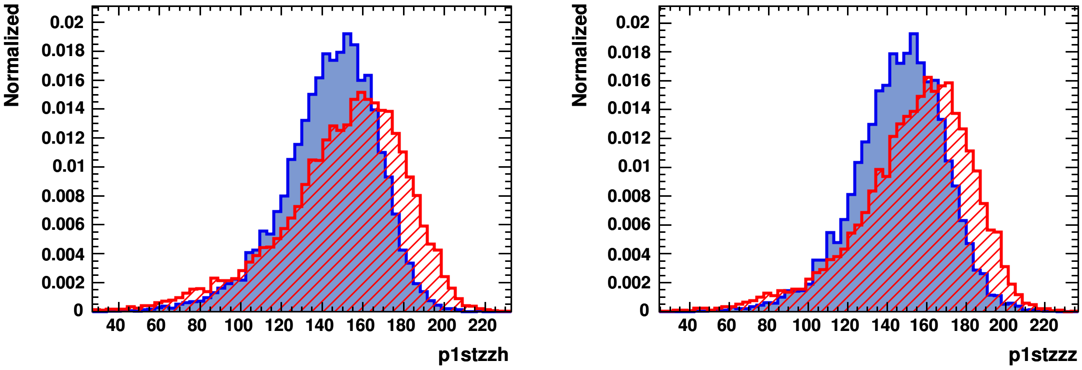

Figure 5.11: Discriminative quantities for the signal (blue) and the same final states backgrounds $\nu\nu bbbb$, $\nu\nu bbH$ (red). The variable names are explained in the text.

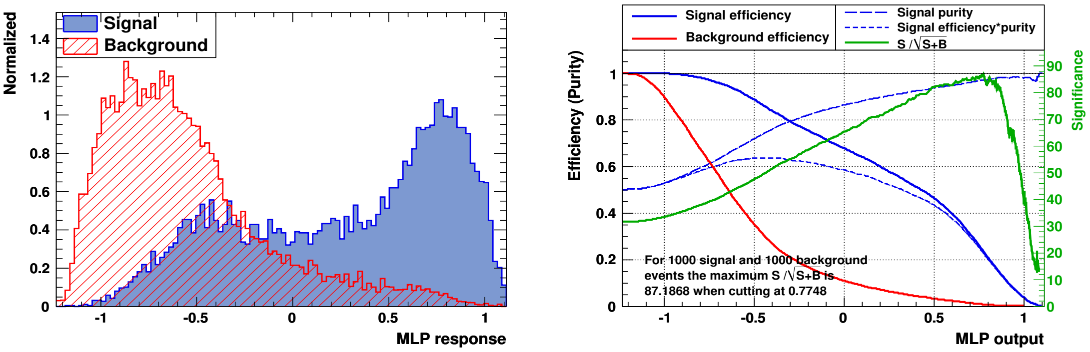

Figure 5.12: (left): The neural-net output for the signal versus the $\nu\nu bbbb$, $\nu\nu bbH$ backgrounds, where the blue histogram is for the signal and the red one is for $\nu\nu bbbb$ and $\nu\nu bbH$. (right): The cut efficiencies for the signal and the backgrounds at different cut values on the neural-net output, where the solid blue curve is for the signal and the red one is for $\nu\nu bbbb$, $\nu\nu bbH$.

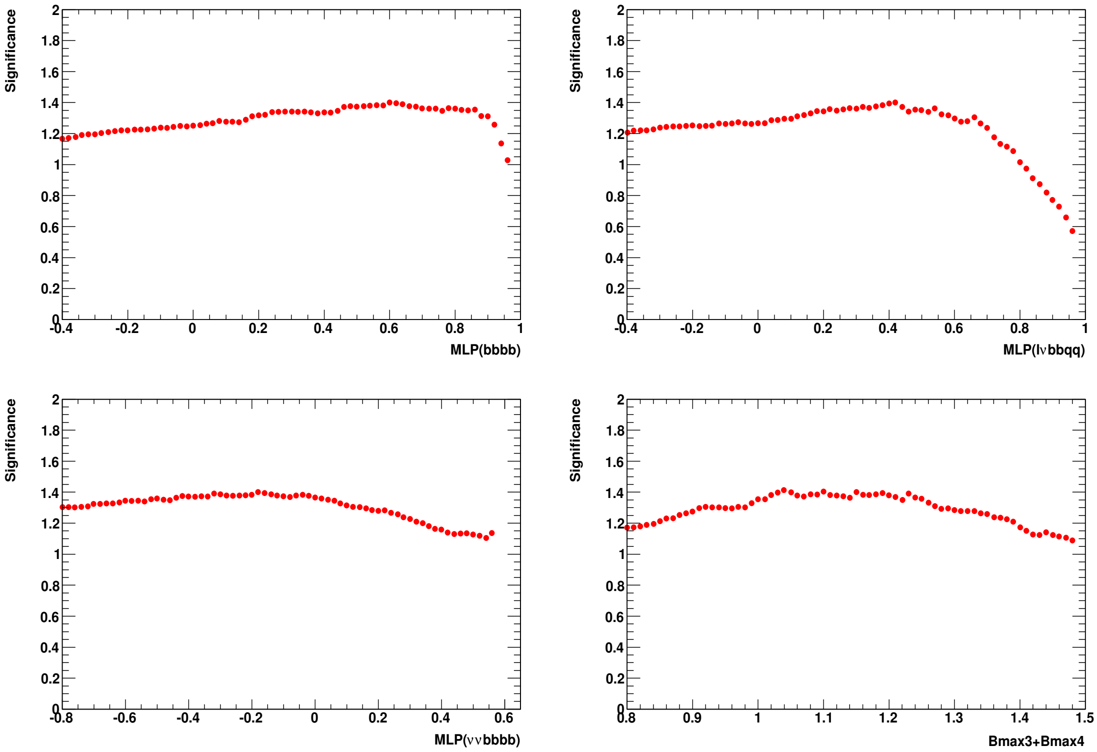

Figure 5.13: The optimization of cuts on the three neural-net outputs and the b-likeness. (top left): MLP1; (top right): MLP2; (bottom left): MLP3; (bottom right): B tagging, the cut names are explained in the text.

Chapter 6

Full Simulation of $e^+ + e^- \to q\bar{q}HH \to q\bar{q}b\bar{b}b\bar{b}$ at 500 GeV

6.1 Signal and Backgrounds

In this search mode, the final state of a candidate signal event contains four of six b quarks each fragmenting into a b jet. All the signal events come from the $e^+ + e^- \to$ ZHH process without contributions from WW and ZZ fusion processes. At 500 GeV, the cross section of the $e^+ + e^- \to q\bar{q}$HH process without beam polarization is 111 ab for the Higgs mass of 120 GeV.With the integrated luminosity of 2 ab^{-1}, the expected number of $q\bar{q}$HH signal events is 222, of which 97.6 events lead to $q\bar{q}b\bar{b}b\bar{b}$ final states.

Processes having four or more quarks, at least two of which are b quarks, are considered as possible backgrounds. The cross sections of all the considered background processes and the expected numbers of events for the integrated luminosity of 2 ab^{-1} are shown in Table 6.1. The corresponding numbers of generated MC events are also shown there. All the processes are labeled by the parton level final states.

6.2 Pre-selction

In the pre-selction for the qqHH search mode, we do not require the absence of isolated charged lepton, since the backgrounds containing isolated charged leptons are not dominant. Nevertheless the information on charged leptons will be used in the final selection. All the PFOs are forced to six jets, which are then paired to form two Higgs bosons and one Z boson.

6.2.1 Lepton Identification

The criteria for electron and muon identification are the same as those used in Eqn 4.1 and 4.4, where no isolation requirement is imposed. Among all the identified

Table 6.1: The cross sections and the expected numbers of events for the signal and the backgrounds in the qqHH search mode, without beam polarization at 500 GeV.

Process	Cross Section (fb)	Expected	MC
$e^+ + e^- \to qq$HH	0.111	222	117173
$e^+ + e^- \to bbcsdu$	115	230600	710285
$e^+ + e^- \to bbuddu$	58.1	116200	109200
$e^+ + e^- \to bbcssc$	57.8	115600	359084
$e^+ + e^- \to bbbb$	11.8	23900	198431
$e^+ + e^- \to ttqq$	0.601	1203	9999
$e^+ + e^- \to l\nu bbqq$	239	477600	797027
$e^+ + e^- \to bbbbbb$	0.0034	6.9	15978
$e^+ + e^- \to qqbbbb$	0.0438	87.6	59994
$e^+ + e^- \to qqqq$H	0.120	241	49702

electrons and muons in each event, the one which has the largest momentum is selected. The momentum and the cone energy of this charged lepton, denoted by “plmax” and “econlmax”, are going to be used in the final selection to suppress the semi-leptonic backgrounds.

6.2.2 Jet Clustering and Jet Pairing

All the PFOs are forced to six jets by using the Durham jet clustering algorithm. The resultant six jets j_1, j_2, j_3, j_4, j_5 and j_6 are combined to form three pairs. Among all the possible combinations, we select the one which minimizes the χ^2 defined by

$$\chi^2 = \frac{(M(j_1,j_2) - M(H))^2}{\sigma_H^2} + \frac{(M(j_3,j_4) - M(H))^2}{\sigma_H^2} + \frac{(M(j_5,j_6) - M(Z))^2}{\sigma_Z^2} \tag{6.1}$$

where the last term is for the Z candidate with M(Z) being the nominal Z boson mass. The resolutions for the Z and Higgs masses as well as those for the W and Top masses, which will be used in the following section, are well studied in [45]. In the jet pairing, we use a very tight b tagging which requires that the b-likeness of each of the four jets from the two Higgs candidates should be no less than 0.3, so that most backgrounds would fail. Jet pair of j_1, j_2 corresponds to the first Higgs, pair j_3, j_4 to the second Higgs and pair j_5, j_6 to the Z boson candidate.

6.3 Final Selection

The numbers of the signal and the background events after the pre-selection are shown in Table 6.2. Though most of the backgrounds are significantly suppressed by the tight b tagging, the remaining backgrounds are still huge, comparing to the signal. Among the remaining backgrounds, the $bbbb$, $bbcsdu$ and $qqbbbb$ backgrounds require special treatment based on neural-net classification. An important strategy used here is to treat the bbHH signal and the light quark qqHH signal with $q =$

u, d, s, c differently, because they have different discriminative power as shown in following sections.

Table 6.2: The expected numbers of events before and after the pre-selection for the signal and the backgrounds in the qqHH search mode, without beam polarization at 500 GeV.

Process	before selection	pre-selection
$e^+ + e^- \to qq$HH ($qqbbbb$)	222 97.6	55.1 43.9
$e^+ + e^- \to bbcsdu$	230600	1258
$e^+ + e^- \to bbuddu$	116200	212
$e^+ + e^- \to bbcssc$	115600	2874
$e^+ + e^- \to bbbb$	23900	4420
$e^+ + e^- \to ttqq$	1203	89.1
$e^+ + e^- \to l\nu bbqq$	477600	7086
$e^+ + e^- \to bbbbbb$	6.9	5.48
$e^+ + e^- \to qqbbbb$	87.6	27.4
$e^+ + e^- \to qqqq$H	241	19.6

6.3.1 B-likeness of jets from Z

For the different quark modes of the qqHH signal, figure 6.1 shows the distribution of probZ1 + probZ2, where probZ1 and probZ2 are the b-likeness values of the two jets from Z. The red histogram is for the bbHH process, the green one for ccHH and the blue one for the qqHH ($q = u, d, s$) processes. In the large probZ1 + probZ2 region, the main contribution comes from the bbHH events, while in the small probZ1 + probZ2 region, each light quark mode of qqHH contributes more or less democratically. Notice that the background contaminations in the two regions are very different. It is hence helpful to use different cuts in the two regions, which is the key point of the strategy for the final selection in this qqHH mode. The two regions are defined to be Part A: probZ1 + probZ2 > 0.9 and Part B: probZ1 + probZ2 < 0.9.

6.3.2 Missing energy and isolated lepton

To suppress the backgrounds containing prompt neutrinos, such as the semi-leptonic $l\nu bbqq$ and $ttqq$, the visible energy is required to be greater than 400 GeV and the missing P_t to be less than 60 GeV. On the other hand, in order to suppress the backgrounds with isolated leptons, the information of "plmax" and "econe" kept in the pre-selection can be used. We thus discard events if plmax $>$ 20 GeV and $\mathrm{E_{cone}} <$ 10 GeV. The cuts here (denoted by Cut1) can be summarized as:

$$\mathrm{Cut1}: \begin{cases} \mathrm{E_{vis}} > 400 \text{ GeV} \\ \mathrm{MissPt} < 60 \text{ GeV} \\ \mathrm{plmax} < 20 \text{ GeV } \textit{or } \mathrm{E_{cone}} > 10 \text{ GeV} \end{cases} \tag{6.2}$$

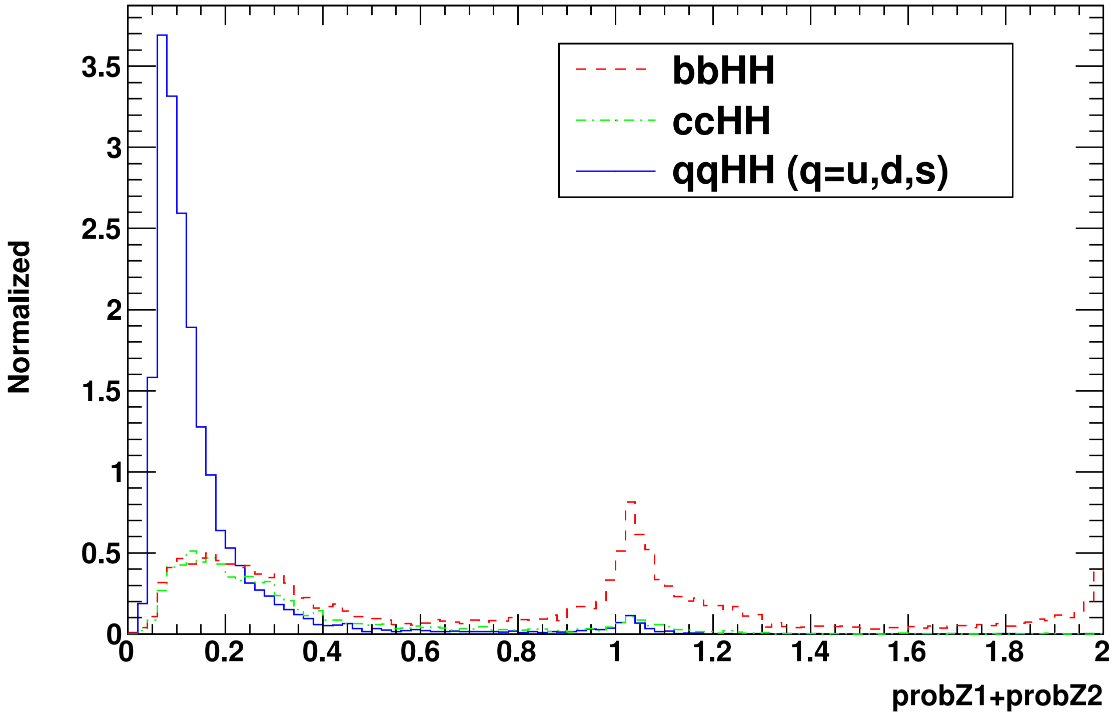

Figure 6.1: Distribution of the sum of b-likeness values of the two jets from Z for the signal. The red histogram is for bbHH, the green one for ccHH and the blue one for qqHH, where $q = u, d, s$.

6.3.3 $bbbb$ jets-poor background

As shown in Table 6.2, the number of the $bbbb$ background events is very large even after the pre-selection. As with the strategy for the $bbbb$ suppression in the $\nu\nu$HH mode, a neural-net is trained to further suppress this background, by using the following discriminative quantities:

- Axis of thrust. The $bbbb$ background mainly coms from t-channel two-body processes. The axis of thrust, denoted by “cosaxis”, is much more forward than that of the signal, as indicated in Figure 6.2.
- Y values. The jet multiplicity of the $bbbb$ background is very different from that of the signal. The Y values $Y_{6\to5}$, $Y_{5\to4}$ and $Y_{4\to3}$ can hence offer the main discriminative power. Distributions of these three Y values are shown in Figure 6.2, respectively, denoted by “yminus”, “yplus4”, “yminus4”.
- The reconstructed Z mass. The events are forced to four jets and then the four jets are paired as from ZZ. The reconstructed invariant masses of the two Z boson candidates are very discriminative. Distributions of these two Z masses, denoted by “mz14j” and “mz24j”, are shown in Figure 6.2.
- The largest jet momentum of the four jets as reconstructed from ZZ, and its polar angle. Distributions of these two quantities are shown in Figure 6.3, denoted by “pjmax4j” and “cosjmax4j”.

- The total number of PFOs. The total number of PFOs is much smaller than that of the signal. The distribution of this quantity, denoted by “npfos”, is shown in Figure 6.3.
- The smallest number of PFOs in a jet among the six jets. The distribution of this quantity is shown in Figure 6.3, denoted by “npfomin”.

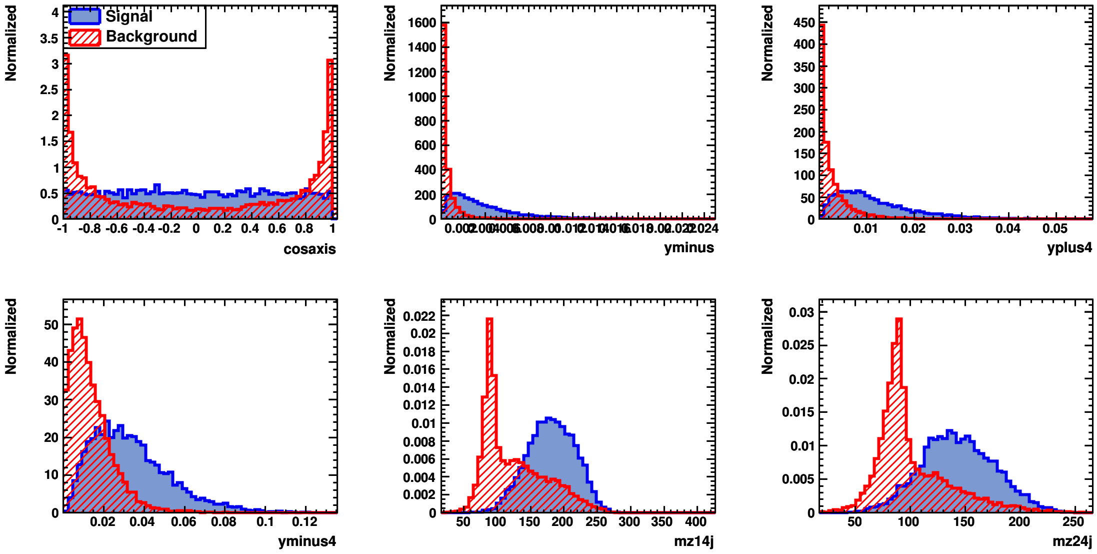

Figure 6.2: Discriminative quantities for the signal (blue) and the jets poor backgrounds $bbbb$ (red). The variable names are explained in the text.

By using these quantities as input variables, a neural-net is trained for the signal and the $bbbb$ background after a pre-cut on thrust < 0.9. For the neural-net training, a statistically independent $\nu\bar{\nu}$HH signal sample and the $bbbb$ background sample with statistics higher than 2 ab^{-1} are used. The neural-net outputs and the cut efficiencies for the signal and the background are shown in Figure 6.4. The $bbbb$ background is well separated by the neural-net output (MLP$_{bbbb}$).

6.3.4 The fully hadronic backgrounds

The fully hadronic backgrounds mainly refer to $bbcsdu$, $bbuddu$ and $bbcssc$, which come from $t\bar{t}$ and WWZ. The cross sections of these processes are very large. Though they are significantly suppressed by the b tagging in the pre-selection, the number of remaining events is still much larger than that of the signal, since they also have six quarks in the final state, making it very challenging to further suppress them. Another neural-net is trained to carry out the suppression, by using the following discriminative quantities:

- Reconstructed Z mass and two Higgs masses. Distributions of these quantities are shown in Figure 6.5, respectively, denoted by “mz”, “mh1”, “mh2”.

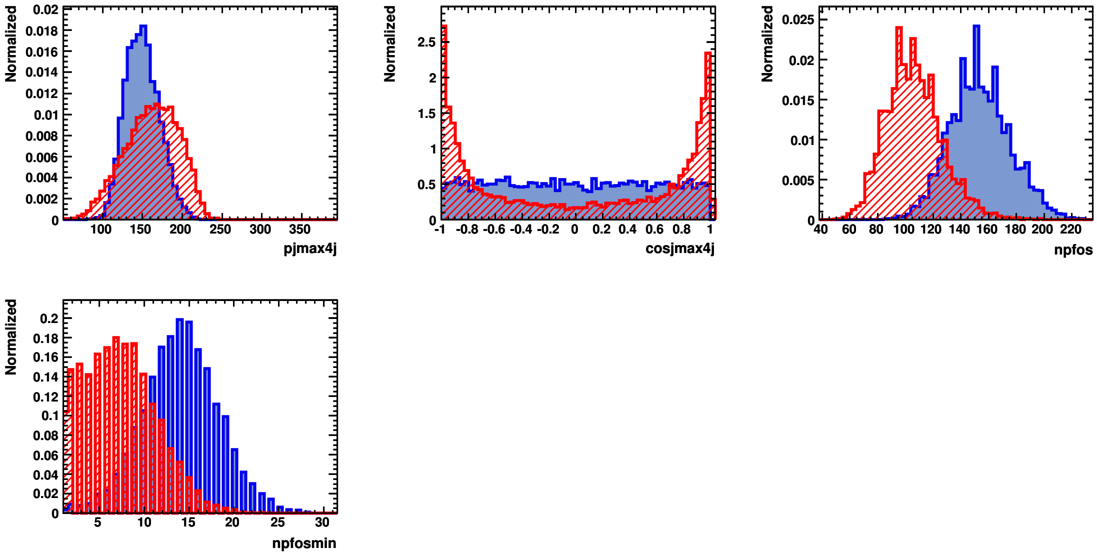

Figure 6.3: Discriminative quantities for the signal (blue) and the jets poor backgrounds *bbbb* (red). The variable names are explained in the text.

- Reconstructed W and Top masses. In order to eliminate the fully hadronic background from the $t\bar{t}$ process the six jets are paired as from a fully hadronic decay of $t\bar{t}$, by minimizing the χ^2 defined by

$$\begin{aligned}\chi^2 \;=\; & \frac{(M(j_1,j_2)-M(W))^2}{\sigma_W^2}+\frac{(M(j_3,j_4)-M(W))^2}{\sigma_W^2} \\ & +\frac{(M(j_1,j_2,j_5)-M(t))^2}{\sigma_t^2}+\frac{(M(j_3,j_4,j_6)-M(t))^2}{\sigma_t^2}\end{aligned} \tag{6.3}$$

  Invariant masses $M(j_1,j_2)$ and $M(j_3,j_4)$ correspond to the two W masses, while $M(j_1,j_2,j_5)$ and $M(j_3,j_4,j_6)$ correspond to the two Top masses. Distributions of these quantities are shown in Figure 6.5 − 6.6, denoted by “mw1tt”, “mw2tt”, “mt1tt” and “mt2tt”.

- Angle between two most b-like jets, the same as that in the llHH mode. The distribution of this quantity is shown in Figure 6.6, denoted by “cosbmax”.

- Largest jet momentum of the six jets and its polar angle. Distribution of these two quantities are shown in Figure 6.6, denoted by “pjmax6j” and “cosjmax6j”.

- The total number of PFOs. As mention in the llHH mode section, b jets usually have more PFOs. The distribution of this quantity is shown in Figure 6.3, denoted by “npfos”.

By using these quantities as input variables, yet another neural-net is trained for the signal and the *bbcsdu*, *bbuddu* and *bbcssc* backgrounds. For the neural-net training, a statistically independent $\nu\bar{\nu}$HH signal sample and the *bbcsdu*, *bbuddu* and *bbcssc* background samples with statistics higher than 2 ab^{-1} are used. The

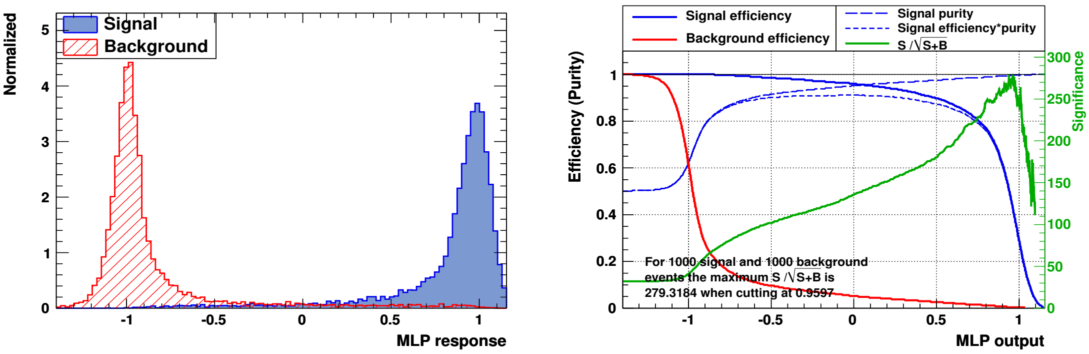

Figure 6.4: (left): The neural-net output for signal versus *bbbb* background, where blue histogram is for signal and red one is for *bbbb*. (right): The cut efficiencies of signal and background at different cuts on neural-net output, where solid blue curve is for signal and red one is for *bbbb*.

neural-net outputs and the cut efficiencies for the signal and the background are shown in Figure 6.7. As seen from the neural-net output (MLP_{bbqqqq}) distribution, the separation of these backgrounds is very limited.

6.3.5 Backgrounds with Same Final States

The backgrounds with the same final states mainly refer to $qqbbbb$ and $qqqqH$, coming from ZZZ and ZZH. The strategy to suppress them is the same as that for the $\nu\nu$HH modes. The following quantities are used for neural-net training, distributions of which are shown in Figure 6.8 − 6.9:

- Reconstructed Z and Higgs masses when re-reconstructed as from $qqZH$, while keeping the two jets previously paired as from Z, denoted by "mzzh" and "mhzh".
- Reconstructed two Z masses when re-reconstructed as from $qqZZ$, denoted by "mz1zz" and "mz2zz".
- Quantities reflecting t-channel characteristics expected for the ZZZ and ZZH backgrounds. The largest momentum of the three boson candidates formed with the ZZH hypothesis and the polar angle of that boson, denoted by "p1stzzh" and "cos1stzzh". Similarly for the ZZZ hypothesis, the largest momentum "p1stzzz" and its polar angle "cos1stzzz".

For the neural-net training, a statistically independent qqHH signal samples and the $qqbbbb$, $qqqqH$ background samples are used, each with statistics higher than 2 ab^{-1}. The neural-net outputs and the cut efficiencies for the signal and the backgrounds are shown in Figure 6.10.

6.3.6 B tagging

Similar to the b tagging strategy used for the llHH mode, the four jets from the two Higgs are ordered with the b-likeness values, Bmax1, Bmax2, Bmax3 and Bmax4.

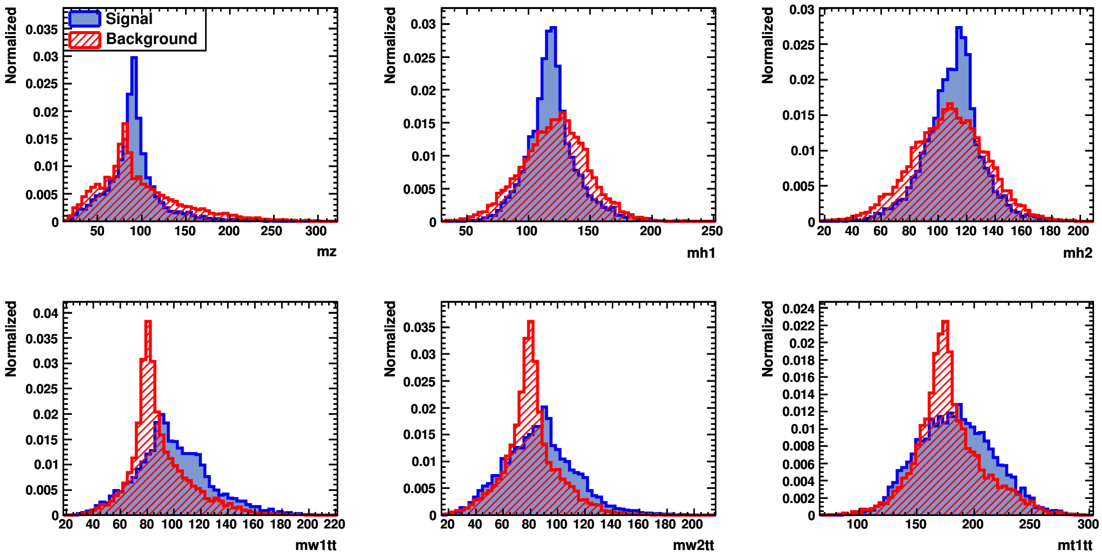

Figure 6.5: Discriminative quantities for the signal (blue) and the fully hadronic backgrounds *bbcsdu*, *bbuddu* and *bbcssc* (red). The variable names are explained in the text.

For the pre-selection, Bmax4 is required to be no less than 0.3. For the final selection, further cuts on Bmax3 and Bmax4 are required, as shown in following section.

6.4 Results

All the events are divided into two parts by the b-likeness values of the two jets from Z. The optimized cuts and consequently the results for these two parts are different, as shown in the following.

6.4.1 Part A: probZ1 + probZ2 > 0.9

For this part, most of the backgrounds are significantly suppressed by probZ1 + probZ2 > 0.9 thereby allowing us to relax the requirements on the neural-net outputs and the b tagging. For the final selection, we thus demand the following:

- Neural-net for *bbbb*: $MLP_{bbbb} > 0.2$, denoted by MLP1.
- Neural-net for *bbqqqq*: $MLP_{bbqqqq} > -0.3$, denoted by MLP2.
- Neural-net for *qqbbbb*: $MLP_{qqbbbb} > -0.6$, denoted by MLP3.
- B tagging: $Bmax3 > 0.76$ and $Bmax4 > 0.33$, denoted by B tagging.

The numbers of the remaining signal and background events after the final selection are shown in the reduction table 6.3 in the case of no beam polarization. 5.8 signal events survived with 9.0 background events. The effect of different beam polarization cases is tabluated in Table 6.4. As with the other two modes, the left handed

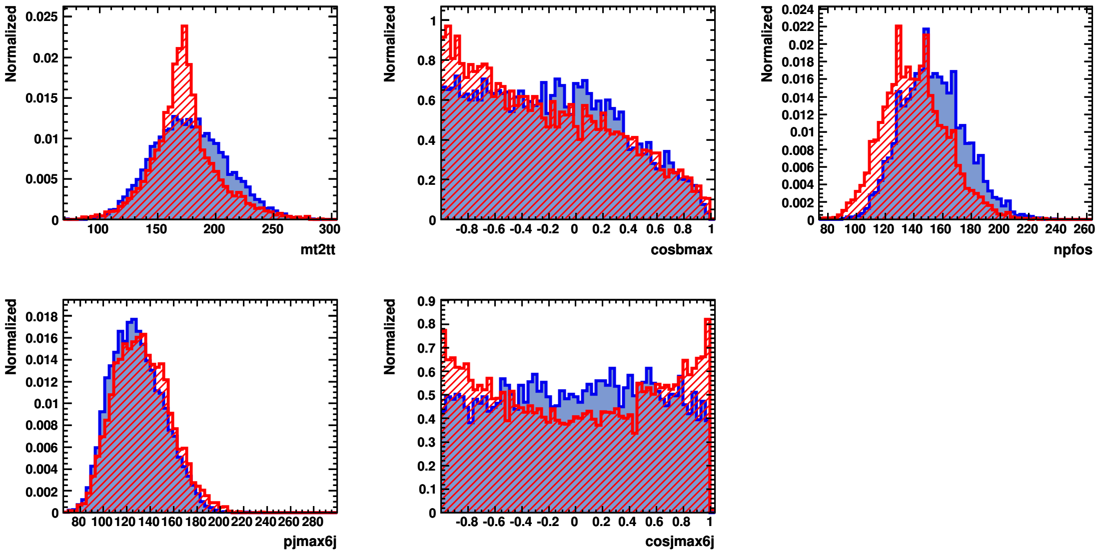

Figure 6.6: Discriminative quantities for the signal (blue) and the fully hadronic backgrounds *bbcsdu*, *bbuddu* and *bbcssc* (red). The variable names are explained in the text.

polarization is favored. The cuts on the neural-net output and the b tagging are optimized, as shown in Figure 6.11. The errors on the expected numbers of the signal and the backgrounds are shown in Table 6.5.

Table 6.3: Reduction table for the signal and the backgrounds after the final selection for Part A. The cut names are explained in text.

Process	Expected	Cut0	Part A	Cut1	MLP1	MLP2	MLP3	B tagging
*qq*HH	222	55.1	10.4	9.34	8.84	8.56	8.20	5.76
(*qqbbbb*)	97.6	43.9	9.33	8.74	8.31	8.06	7.73	5.53
bbcsdu	230600	1258	12.3	12.0	9.21	6.14	5.58	0.56
bbuddu	116200	212	6.36	5.27	4.19	4.19	2.01	2.01
bbcssc	115600	2874	31.7	29.2	25.6	19.9	18.2	1.38
bbbb	23900	4420	558	460	2.11	1.52	1.26	0.71
ttqq	1203	89.1	5.31	2.66	2.54	2.47	2.38	0.99
$l\nu bbqq$	477600	7086	134	20.3	3.58	3.58	2.82	0.50
bbbbbb	6.9	5.48	2.56	2.33	1.82	1.57	1.07	0.84
qqbbbb	87.6	27.4	1.70	1.60	1.05	0.90	0.65	0.28
*qqq*H	241	19.6	2.81	2.44	2.19	2.05	1.77	1.15

6.4.2 **Part B:** probZ1 + probZ2 < 0.9

For this part, the backgrounds are much larger than Part A, necessitating tighter cuts on the neural-net outputs and the b tagging. For the final selection, the cuts on the neural-net outputs and the b tagging are optimized as:

Table 6.4: The numbers of the remaining signal and background events for the different polarization cases and the corresponding significance for Part A.

Final selection	no polarization	left handed
qqHH	5.76	8.50
Background	9.03	11.7
significance (i)	1.7σ	2.2σ
significance (ii)	1.4σ	1.9σ
$bbcsdu$	0.56	1.38
$bbuddu$	2.01	0.28
$bbcssc$	1.38	2.01
$bbbb$	0.71	1.27
$ttqq$	0.99	1.85
$l\nu bbqq$	0.50	0.07
$bbbbb$	0.84	1.61
$qqbbbb$	0.28	0.55
$qqqq$H	1.15	2.70

Table 6.5: The expected numbers of the remaining signal and background events with errors in the case of the left handed polarization for Part A.

Final selection	left handed
qqHH	8.50 ± 0.2
Background	11.7 ± 1.5
$bbcsdu$	1.38 ± 0.92
$bbcssc$	2.01 ± 1.12
$bbbb$	1.27 ± 0.35
$ttqq$	1.85 ± 0.27
$qqbbbb$	2.09 ± 0.55
$qqqq$H	2.70 ± 0.14

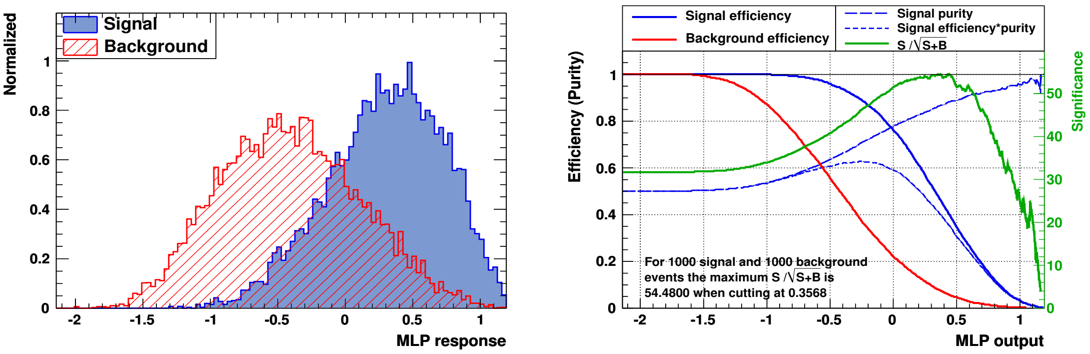

Figure 6.7: (left): The neural-net output for the signal versus the *bbcsdu*, *bbuddu* and *bbcssc* backgrounds, where the blue histogram is for the signal and the red one is for the backgrounds. (right): The cut efficiencies for the signal and the background at different cut values on the neural-net output, where the solid blue curve is for the signal and the red one is for the backgrounds.

- Neural-net for *bbbb*: $MLP_{bbbb} > -0.2$, denoted by MLP1.
- Neural-net for *bbqqqq*: $MLP_{bbqqqq} > 0.16$, denoted by MLP2.
- B tagging: $Bmax3 > 0.8$ and $Bmax4 > 0.52$, denoted by B tagging.

The numbers of the remaining signal and background events after the final selection are shown in the reduction table 6.6 in the case of no beam polarization. 11.3 signal events survived with 68.2 background events. The effect of different beam polarization cases is tabulated in Table 6.7, indicating the advantage of the left handed polarization. The cuts on the neural-net outputs and the b tagging are optimized, as shown in Figure 6.12. The errors on the expected numbers of the signal and the backgrounds are shown in Table 6.8

Table 6.6: Reduction table for the signal and the backgrounds in the final selection for Part B. The cut names are explained in the text.

Process	Expected	Cut0	Part A	Cut1	MLP1	MLP2	B tagging
*qq*HH	222	55.1	44.7	38.8	37.0	22.2	11.3
(*qqbbbb*)	97.6	43.9	34.5	32.8	31.7	19.4	10.2
bbcsdu	230600	1258	1246	1197	1077	195	17.3
bbuddu	116200	212	206	198	175	36.3	4.19
bbcssc	115600	2874	2842	2715	2430	361	22.6
bbbb	23900	4420	3862	3134	44.9	11.1	5.79
ttqq	1203	89.1	83.8	41.0	40.5	22.4	7.46
$l\nu bbqq$	477600	7086	6952	955	177	27.4	2.48
bbbbbb	6.9	5.48	2.92	2.63	2.05	0.65	0.38
qqbbbb	87.6	27.4	25.7	24.2	19.2	6.06	3.08
*qqqq*H	241	19.6	16.8	14.9	13.8	6.61	3.28

Table 6.7: The remaining signal and background events in the case of different polarization cases and the corresponding significances for Part B.

Final selection	no polarization	left handed
qqHH	11.3	16.6
Background	68.2	129
significance (i)	1.3σ	1.4σ
significance (ii)	1.2σ	1.3σ
$bbcsdu$	17.3	42.2
$bbuddu$	4.19	5.37
$bbcssc$	22.6	39.6
$bbbb$	5.79	9.12
$ttqq$	7.46	13.7
$l\nu bbqq$	2.48	4.34
$bbbbb$	0.38	0.91
$qqbbbb$	3.08	6.00
$qqqq$H	3.28	7.65

Table 6.8: The expected numbers of the remaining signal and background events with errors in the case of the left handed polarization for Part B.

Final selection	left handed
qqHH	16.6 ± 0.3
Background	129 ± 8
$bbcsdu$	42.2 ± 5.1
$bbuddu$	5.4 ± 3.6
$bbcssc$	39.6 ± 5.0
$bbbb$	9.1 ± 0.6
$ttqq$	13.7 ± 0.7
$qqbbbb$	6.7 ± 0.4
$qqqq$H	7.6 ± 0.2

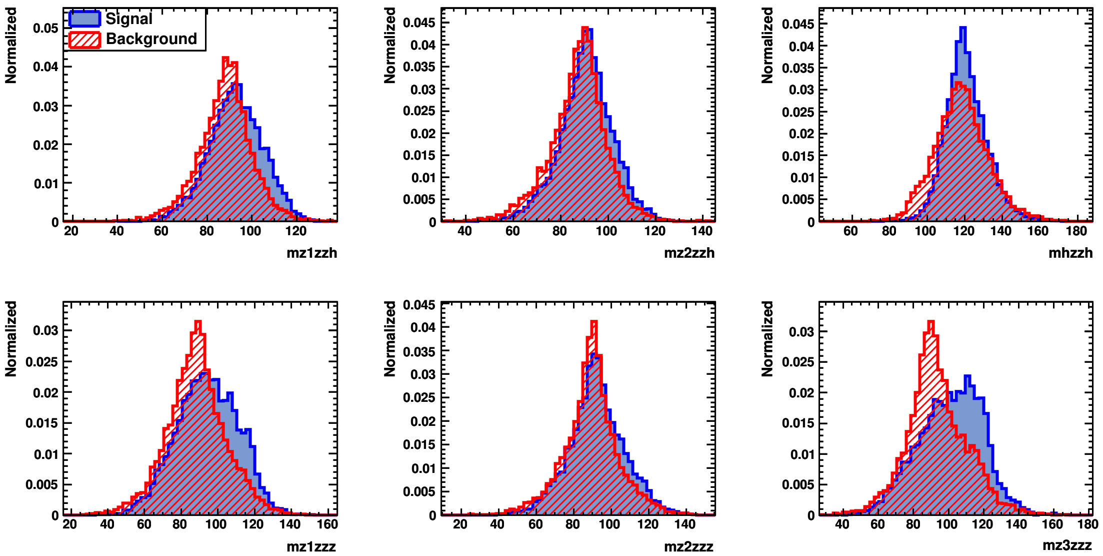

Figure 6.8: Discriminative quantities for the signal (blue) and the same final state backgrounds $qqbbbb$ and $qqqqH$ (red). The variable names are explained in the text.

6.4.3 Summary of the qqHH mode

In this $e^+ + e^- \to q\bar{q}$HH search mode, assuming the Higgs mass of 120 GeV and the integrated luminosity of 2 ab^{-1}, two independent signal samples are obtained. One (Part A) has 8.5 signal events with 11.7 background events, corresponding to a ZHH excess significance of 2.2σ and a measurement significance of 1.9σ; the other (Part B) has 16.6 signal events with 129 backgrounds, corresponding to a ZHH excess significance of 1.4σ and a measurement significance of 1.3σ.

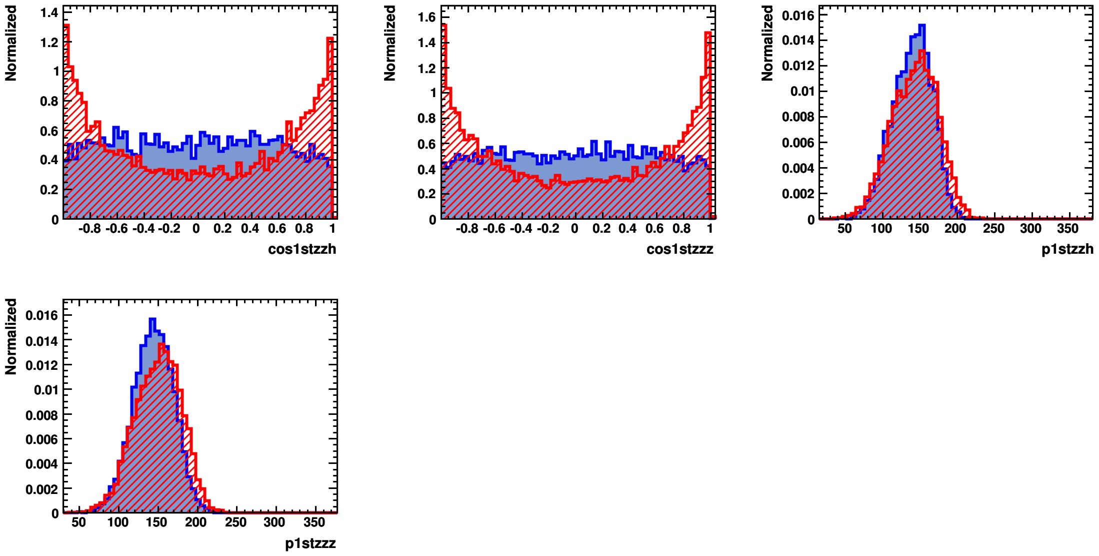

Figure 6.9: Discriminative quantities for the signal (blue) and the same final state backgrounds $qqbbbb$, $qqqqH$ (red). The variable names are explained in the text.

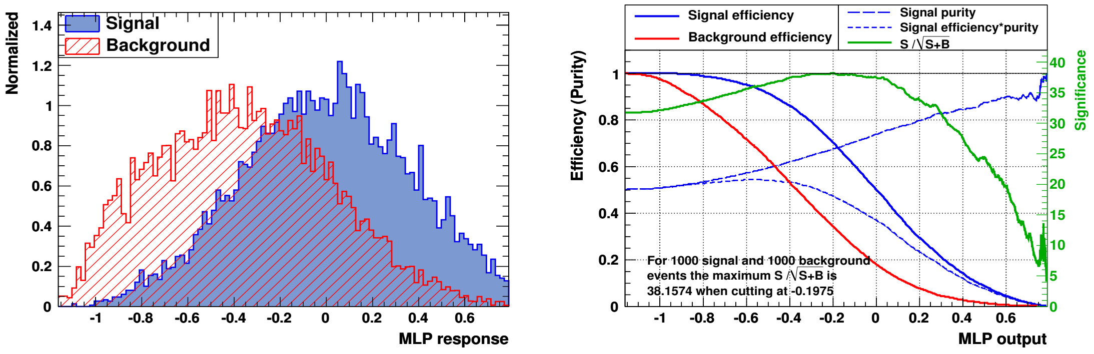

Figure 6.10: (left): The neural-net output for the signal versus the $qqbbbb$, $qqqqH$ backgrounds, where the blue histogram is for the signal and the red one is for the $qqbbbb$ and $qqqqH$. (right): The cut efficiencies for the signal and the background at different cut values on the neural-net output, where the solid blue curve is for the signal and the red one is for $qqbbbb$, $qqqqH$.

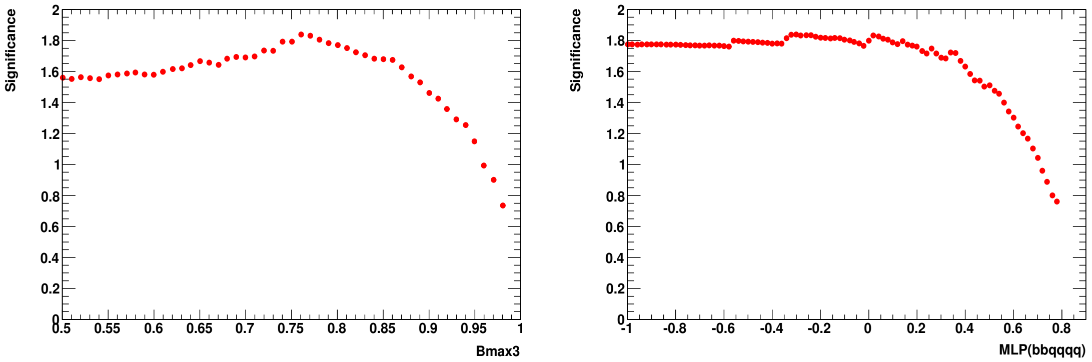

Figure 6.11: For Part A, (left): The optimization of the cut on the b-likeness Bmax3. (right): The optimization of the cut on the neural-net output for the full hadronic backgrounds *bbcsdu*, *bbuddu* and *bbcssc*.

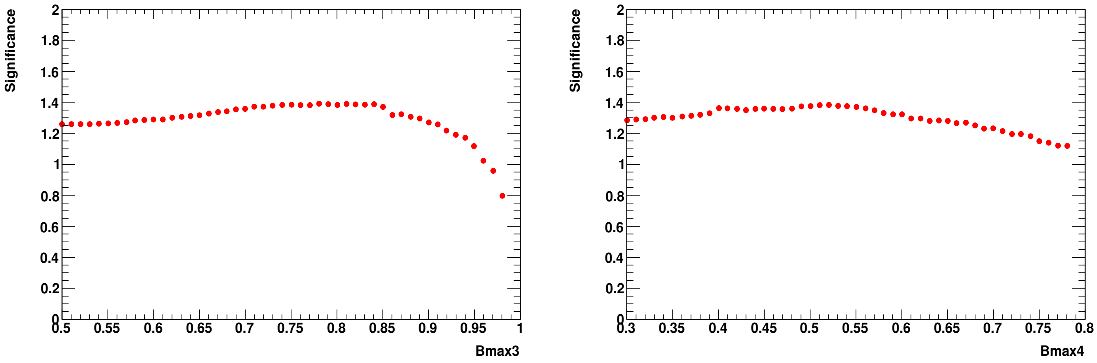

Figure 6.12: For Part B, (left): The optimization of the cut on the b-likeness Bmax3. (right): The optimization of the cut on the b-likeness Bmax4.

Chapter 7

Combined Result of the Full Simulation at 500 GeV

The three decay modes (llHH, $\nu\nu$HH, qqHH) of ZHH at 500 GeV have been fully simulated to test the feasibility of the Higgs self-coupling measurement at the ILC, assuming a Higgs mass of 120 GeV and an integrated luminosity of 2 ab^{-1}. The results of the three modes are shown in Table 7.1 for the left handed beam polarization, which is favored because of its higher sensitivity to the self-coupling. The ZHH excess significance (i) and the measurement significance (ii) are also shown there. Notice that there are two independent parts in the $q\bar{q}HH$ mode. In this chapter, we will combine these full simulation results and try to answer the following two crucial questions:

- Can we observe the ZHH events? Or how much is the combined ZHH excess significance?
- Can we observe the trilinear Higgs self-interaction? Or how precisely can we measure the trilinear Higgs self-coupling?

Table 7.1: The numbers of the remaining signal and background events in each search mode of the ZHH full simulation at 500 GeV, with the left handed beam polarization.

Searching Mode	Signal	Background	Significance (i)	Significance (ii)
$e^+ + e^- \to l^+l^-$HH	6.4	6.7	2.1σ	1.7σ
$e^+ + e^- \to \nu\bar{\nu}$HH	5.2	7.0	1.7σ	1.4σ
$e^+ + e^- \to q\bar{q}$HH	8.5	11.7	2.2σ	1.9σ
$e^+ + e^- \to q\bar{q}$HH	16.6	129	1.4σ	1.3σ

7.1 Statistical independence of the three modes

Before deriving the combined result, it is necessary to check the statistical independence of the three modes.

- Due to the very different visible energy requirement in the $\nu\nu$HH mode and the other two modes, events selected for the $\nu\nu$HH mode will not satisfy the selection criteria for the other two modes. Thus the $\nu\nu$HH mode is statistically independent of the llHH and qqHH modes.
- Due to the very energetic isolated lepton requirement for the llHH mode, all fully hadronic events will not be selected, so that the llHH mode is statistically independent of the qqHH mode.

Thus we conclude that all the three modes are statistically independent.

7.2 Combined ZHH excess significance

A hypothesis test is used to calculate the combined ZHH excess significance. Define the null hypothesis:

$$\mathrm{H}_0: \quad \text{there is only background (B).} \tag{7.1}$$

and the alternative hypothesis:

$$\mathrm{H}_1: \quad \text{there are ZHH signal and background (S+B).} \tag{7.2}$$

Then define the test variable

$$\chi^2 \equiv -2\ln\frac{L_{s+b}}{L_b} \tag{7.3}$$

where the likelihood L_{s+b} is defined as

$$L_{s+b} = \prod_i \frac{e^{-(s_i+b_i)}(s_i+b_i)^{n_i}}{n_i!} \tag{7.4}$$

and the L_b is defined as

$$L_b = \prod_i \frac{e^{-b_i}b_i^{n_i}}{n_i!}. \tag{7.5}$$

The s_i and b_i are the expected numbers of remaining signal and background events in mode i (search modes $i = 1, .., 4$). The n_i is the total number of observed events in mode i, which is a Poisson random variable, with mean value s_i+b_i under hypothesis H_1, and with mean value b_i under hypothesis H_0.

Figure 7.1 shows the distributions of the χ^2 test variable under hypothesis H_0, denoted by blue line, and under hypothesis H_1, denoted by red line, produced using a Toy Monte-Carlo. The black line shows the observed value of the test χ^2. The p value is defined as the probability of observing a test χ^2 value equal to or less than the current observed value under the hypothesis H_0:

$$p = \int_{-\infty}^{\chi^2_{obv}} f(\chi^2)\mathrm{d}\chi^2 \tag{7.6}$$

where $f(\chi^2)$ is the probability density function of the test χ^2 under hypothesis H_0, which is represented by the blue distribution. The p value is calculated to be

$$p = 4.6 \times 10^{-5} \tag{7.7}$$

corresponding to the gaussian significance:

$$1 - p = \int_{\infty}^{s\sigma} N(x; 0, 1)\mathrm{d}x \tag{7.8}$$

where N(x;0,1) is the normal gaussian distribution. The significance is obtained to be $s\sigma = 3.9\sigma$, meaning that the combined ZHH excess significance is 3.9σ.

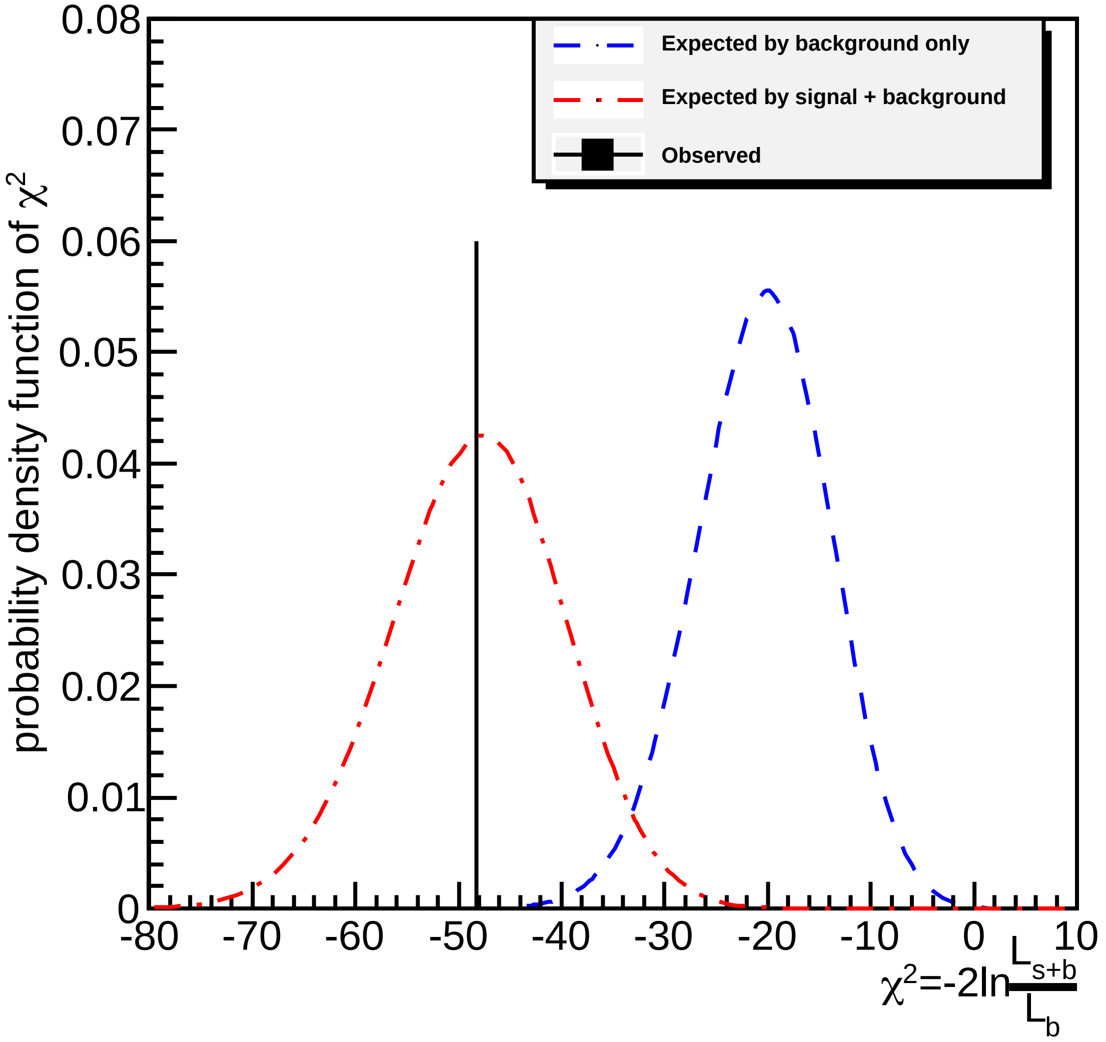

Figure 7.1: The distribution of the test χ^2 under the background only hypothesis (blue) and the signal + background hypothesis (red). The black vertical line denotes the observed value of the test χ^2 variable.

7.3 Extracting the Cross Section of ZHH

The precision of the Higgs self-coupling is determined by the precision of the ZHH cross section, as introduced in Eqn 2.32. The cross section measurement can be carried out by parameter estimation though Maximum Likelihood. Define the combined likelihood

$$L_{s+b} = \prod_i \frac{e^{-(s_i+b_i)}(s_i + b_i)^{n_i}}{n_i!}, \tag{7.9}$$

where b_i is the expected number of background events, which is known from MC simulations; n_i is the number of observed events, which is known from the measurement; s_i is related to the cross section σ_{ZHH}, which is the unique parameter. The relation between s_i and σ_{ZHH} is

$$s_i = (\sigma_{ZHH} + \sigma_i) \cdot \mathrm{Lumi} \cdot \mathrm{Br}_i \cdot \mathrm{Eff}_i \tag{7.10}$$

where Lumi is the integrated luminosity; Br_i is the branch ratio of mode i; Eff_i is the selection efficiency of mode i; σ_i is the fusion contribution for mode i, which is negligible at 500 GeV. The Likelihood hence contains only one parameter σ_{ZHH}. The minimization of $\chi^2 = -2\ln\frac{L}{L_{max}}$ is shown in Figure 7.2. The result is

$$\sigma_{ZHH} \cdot \mathrm{Lumi} = 488^{+145}_{-137}. \tag{7.11}$$

For the integrated luminosity of 2 ab^{-1}, we then have

$$\sigma_{ZHH} = 0.22 \pm 0.07\ \mathrm{fb}. \tag{7.12}$$

The precision of the cross section is 32%, corresponding to a precision of the Higgs self-coupling of 57%.

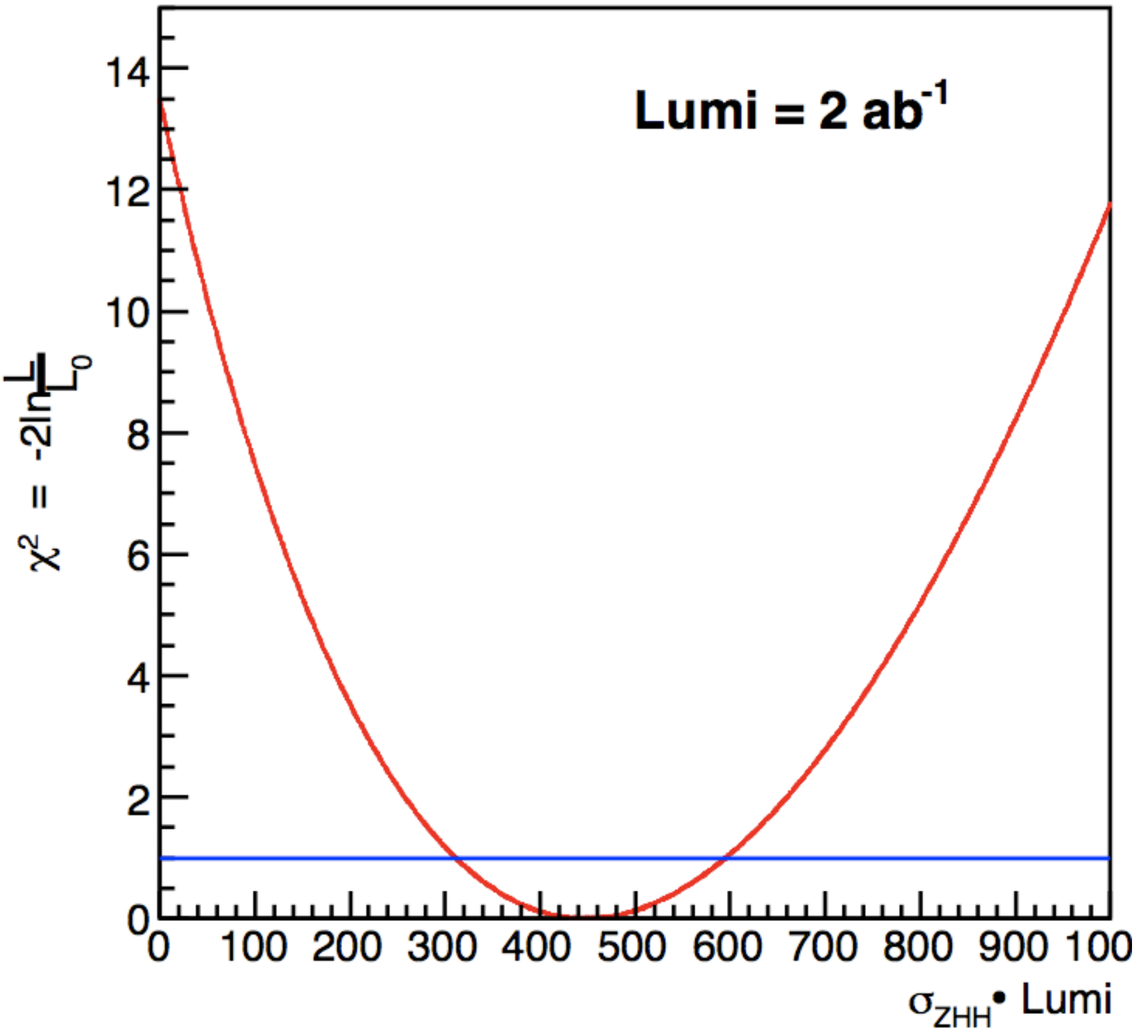

Figure 7.2: The χ^2 as a function of $\sigma_{ZHH} \cdot$ Lumi.

Chapter 8

Fast Simulation of $e^+ + e^- \to \nu_e\bar{\nu}_e\mathrm{HH} \to \nu_e\bar{\nu}_e b\bar{b}b\bar{b}$ at 1 TeV

8.1 Signal and Backgrounds

In this search mode, we focus on the WW fusion contribution of $\nu_e\bar{\nu}_e\mathrm{HH}$ at 1 TeV. The final state of a candidate signal event contains two missing neutrinos and four b quarks segmenting into four b jets. At 1 TeV, the cross section of $e^+ + e^- \to \nu_e\bar{\nu}_e\mathrm{HH}$ without the initial beam polarization and beamstrahlung, but with initial state radiation, is 71.3 ab for the Higgs mass of 120 GeV. The integrated luminosity of 2 ab^{-1}, is expected to yield 142.6 $\nu_e\bar{\nu}_e\mathrm{HH}$ events, of which 63.4 events lead to the $\nu_e\bar{\nu}_e b\bar{b}b\bar{b}$ final states.

Instead of considering parton level backgrounds as in the full simulation at 500 GeV, where backgrounds with the same final states are handled together even if they are coming from different processes, in the fast simulation presented in this chamber, backgrounds from different processes are considered individually. The cross sections of the main background processes and the expected numbers of events for the integrated luminosity of 2 ab^{-1} are shown in Table 8.1. The corresponding numbers of generated MC events are also shown there. It is seen that $t\bar{t}$ is the dominant background.

8.2 Pre-selction

As the pre-selection, we first require there are no isolated charged leptons. Then we force all the particles to four jets and pair the four jets to form two Higgs bosons.

8.2.1 Isolated Lepton Identification

Since the interactions between particles and each sub-detector are not fully simulated, the MC truth information is used to identify electrons and muons. The isolation requirement is much simpler than in the case of the full simulation. We

Table 8.1: Cross sections and the expected numbers of events for the signal and backgrounds in the $\nu_e\bar{\nu}_e$HH search mode, without beam polarization at 1 TeV.

Process	Cross Section (fb)	Expected	MC
$e^+ + e^- \to \nu_e\bar{\nu}_e\mathrm{HH}$	0.0713	143	500K
$e^+ + e^- \to t\bar{t}$	189	377600	500K
$e^+ + e^- \to W^+W^-Z$	61.7	123400	500K
$e^+ + e^- \to ZZZ$	0.832	1664	500K
$e^+ + e^- \to ZZH$	0.350	700	500K
$e^+ + e^- \to \nu_e\bar{\nu}_e ZZ$	6.05	12100	500K
$e^+ + e^- \to \nu_e\bar{\nu}_e ZH$	1.25	2500	500K
$e^+ + e^- \to \nu_e\bar{\nu}_e W^+W^-$	15.1	30200	50K
$e^+ + e^- \to t\bar{t}H$	2.48	4960	50K

require $P > 20$ GeV and $E_{\mathrm{cone}} < 20$ GeV, where P is the momentum and E_{cone} is the cone energy, as the criteria of isolation. A particle is thus defined to be an isolated lepton if it is identified as electron or muon and that it satisfies the isolation. Since the search mode considered here contains no isolated charged leptons, we require the absence of any isolated charged lepton. The signal efficiency after this requirement is expected to be higher than 97%, while the semi-leptonic decay of $t\bar{t}$ is significantly suppressed.

8.2.2 Jet Clustering and Jet Pairing

After requiring the absence of any isolated charged lepton, all the PFOs are forced to four jets by using the JadeE jet clustering algorithm. The resultant four jets j_1, j_2, j_3 and j_4 are then combined to form two pairs, so as the minimize the χ^2 defined as follows. Instead of adopting the traditional χ^2 definition such as Eqn 4.7 used in the full simulation, whose validity is limited if the invariant mass usually is gaussian distributed, a new definition is used:

$$\chi^2 \equiv -2\mathrm{ln}L = -2\mathrm{ln}(f(M_{12})f(M_{34})) = -2\mathrm{ln}f(M_{12}) - 2\mathrm{ln}f(M_{34}) \qquad (8.1)$$

where M_{12} and M_{34} are the invariant masses of jets pair (j_1, j_2) and (j_3, j_4) respectively, and $f(M)$ is the probability density function of the jet pair invariant mass in the case of correct pairing, which can be obtained by using MC truth information. M_{12} is regarded as the mass of the first Higgs, $M(H1)$, and M_{34} as the mass of the second Higgs, $M(H2)$. Figure 8.1 shows the distribution of $M(H1)$ and $M(H2)$, in the case of correct jet pairing for signal events. Based on this distribution, a binned non-parametric kernel function [74] is used to estimate the probability density function of $M(H)$:

$$\begin{aligned} F(x) &= \frac{1}{N}\sum_{j=1}^{m} n_j G(x; t_j, h_j) \qquad (8.2) \\ h_j &= \left(\frac{4}{3}\right)^{1/5} N^{-1/5} \triangle x \sqrt{\frac{N}{n_j}} \end{aligned}$$

where N is the total number of events, m is the number of bins, the summation is over all the bins, n_j is the number of events in bin j, $\triangle x$ is the bin width, t_j is the center of bin j, h_j is called the resolution of bin j, and $G(x; t_j, h_j)$ is a Gaussian probability density function with mean value t_j and width h_j, called gaussian kernel. The so estimated kernel function is shown in Figure 8.2, which indicates that the kernel function well reproduce the real distribution of $M(H)$.

This pairing algorithm turns out to improve the fraction of correct pairing from 80% to 85% for the signal events.

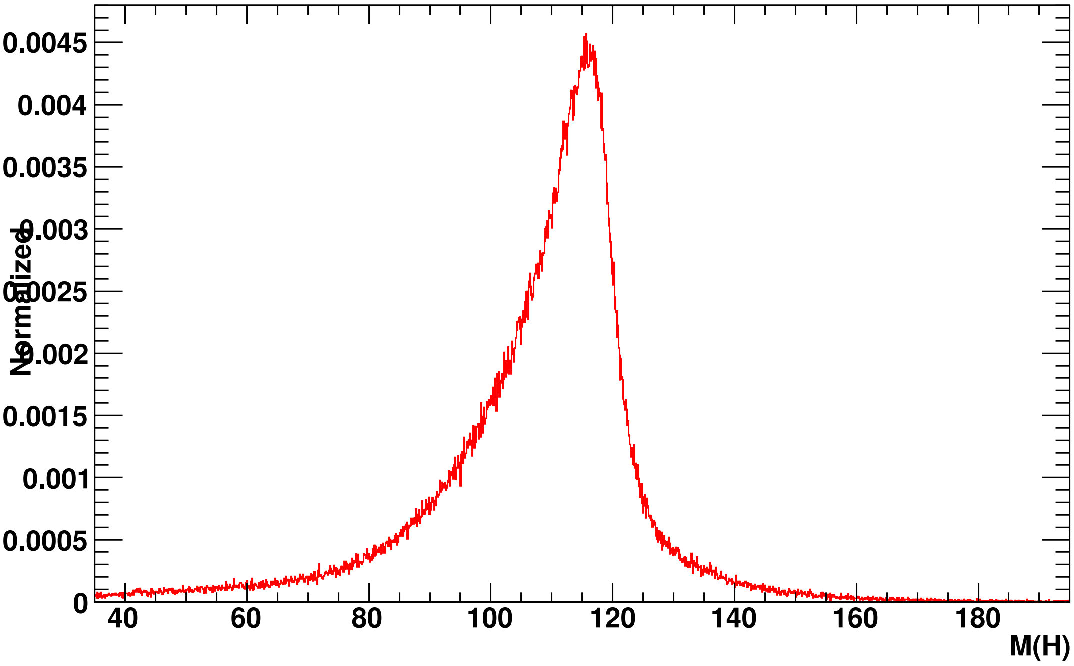

Figure 8.1: The invariant mass of Higgs in the case of correct pairing by using MC truth information. Two Higgs masses are histogrammed together.

8.3 Final Selection

The numbers of the remaining signal and background events after the pre-selection are shown in Table 8.2. One can see that although the semi-leptonic or leptonic decay modes of most of the backgrounds are suppressed after the pre-selection, $t\bar{t}$ still remains as the dominant background, which is to be suppressed by the final selection based on a neural-net method. The $\nu\nu ZZ$ and $\nu\nu ZH$ backgrounds can lead to the same final states as from the signal, and are thus difficult to suppress, necessitating another neural-net. The fully hadronic decay modes of most of the backgrounds can be suppressed by using missing energy requirement.

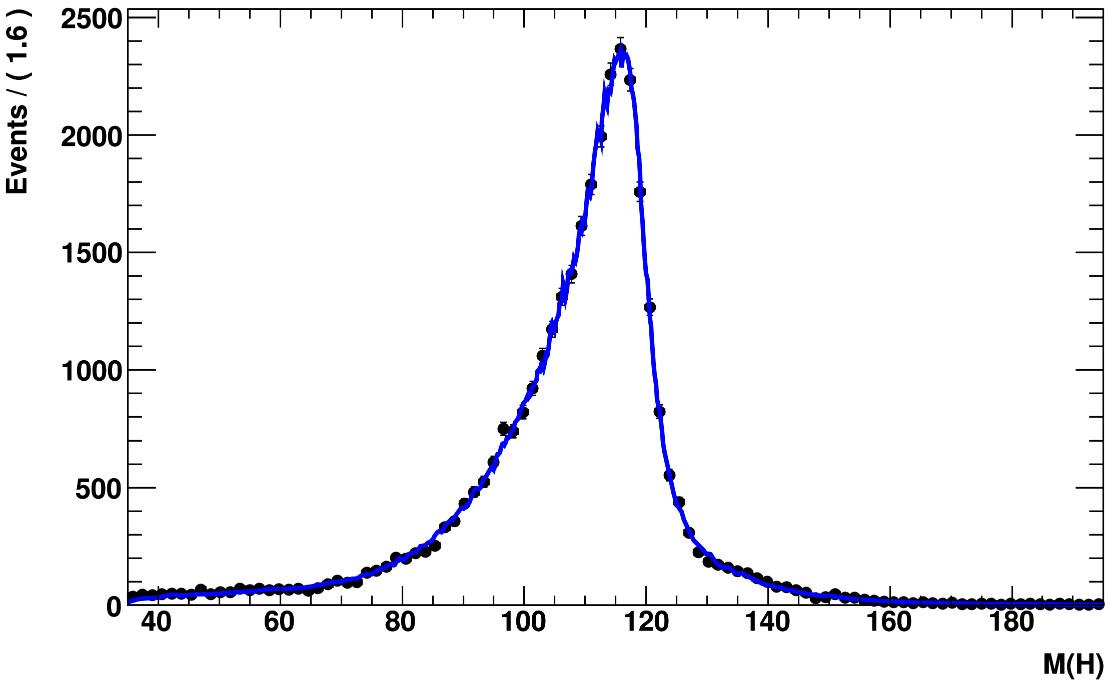

Figure 8.2: The estimated kernel function (blue line) and the corresponding Higgs mass distribution (black dot).

8.3.1 Missing Neutrinos

There are two missing neutrinos in the signal events, making the total visible energy much smaller than the fully hadronic backgrounds. Figure 8.3 shows the distribution of the visible energy for the signal and several background processes. Indeed, most of the remaining $t\bar{t}$ events have their visible energies near the nominal center of mass energy. However the $W \to \tau\nu$ decay of a W from $t\bar{t}$ makes a long tail towards very low visible energy, which might contaminate the signal significantly due to the large $t\bar{t}$ cross section. A cut, denoted by Cut1, on the visible energy, E_{vis}, is imposed as

$$E_{\text{vis}} < 600 \text{ GeV}. \tag{8.3}$$

8.3.2 Neural-net for $t\bar{t}$

After the visible energy cut, there still remain 32326 $t\bar{t}$ background events swamping 111 signal events. A statistically independent $t\bar{t}$ background and the signal samples with statistics higher than 2 ab^{-1} are used to train a neural-net to further suppress $t\bar{t}$. The following discriminative quantities are used as the input variables in this neural-net:

- Reconstructed Higgs mass. Distributions of two invariant masses of Higgs are shown in Figure 8.4, denoted by “mh1” and “mh2”.

Table 8.2: The numbers of remaining signal and background events after the pre-selection without beam polarization. The second line of the $\nu\nu$HH signal in the parentheses denotes the contribution of the $\nu\nu bbbb$ decay from $\nu\nu$HH.

Process	before selection	pre-selection
$e^+ + e^- \to \nu_e\bar{\nu}_e\mathrm{HH}$ $(\nu\nu bbbb)$	143 (63.4)	116 (61.1)
$e^+ + e^- \to t\bar{t}$	377600	160971
$e^+ + e^- \to W^+W^-Z$	123400	27772
$e^+ + e^- \to ZZZ$	1664	609
$e^+ + e^- \to ZZH$	700	240
$e^+ + e^- \to \nu_e\bar{\nu}_e ZZ$	12100	6112
$e^+ + e^- \to \nu_e\bar{\nu}_e ZH$	2500	1620
$e^+ + e^- \to \nu_e\bar{\nu}_e W^+W^-$	30200	14048
$e^+ + e^- \to t\bar{t}H$	4960	184

- Missing P_t. Signal events should have much larger missing P_t. Distributions of this quantity is shown in Figure 8.4, denoted by "mpt".

- Y value. In the case of both Ws from $t\bar{t}$ decaying into $\tau\nu$, the Y value $Y_{4\to3}$ should be smaller than that of the signal. The distribution of this quantity is shown in Figure 8.4, denoted by "ycut".

- The smallest number of particles in a jet out of the four jets. Similarly, if both Ws from $t\bar{t}$ decaying into $\tau\nu$, each τ is expected to be reconstructed as a jet, resulting in a very small number of particles in it. The distribution of this quantity is shown in Figure 8.4, denoted by "npart4".

- Angle between two Higgs bosons. The distribution of this quantity is shown in Figure 8.4, denoted by "coshh".

The neural-net is trained after the pre-cut $E_{\mathrm{vis}} < 600$ GeV. The neural-net outputs, denoted by MLP$_{tt}$, and the cut efficiencies for the signal and the background are shown in Figure 8.5. It is seen that the separation is limited. A tight cut, MLP$_{tt} > 0.6$, is required to further suppress the $t\bar{t}$ background, which is denoted as MLP1.

Additional two quantities are also useful to suppress $t\bar{t}$, though not included in the neural-net training. One is the mass of the jet with the smallest number of particles, denoted by "mjet4". For some $t\bar{t}$ events "mjet4"may peak at the nominal τ mass. The other is the minimal cone energy of all particles, denoted by "econmin". This quantity is designed to remove decay into one charged π, resulting in an isolated charged pions from some $t\bar{t}$ events. The following requirements on these two quantities are imposed, denoted by Cut2,

$$\mathrm{mjet4} > 2\ \mathrm{GeV}, \quad \mathrm{econmin} > 0.1\mathrm{GeV}. \tag{8.4}$$

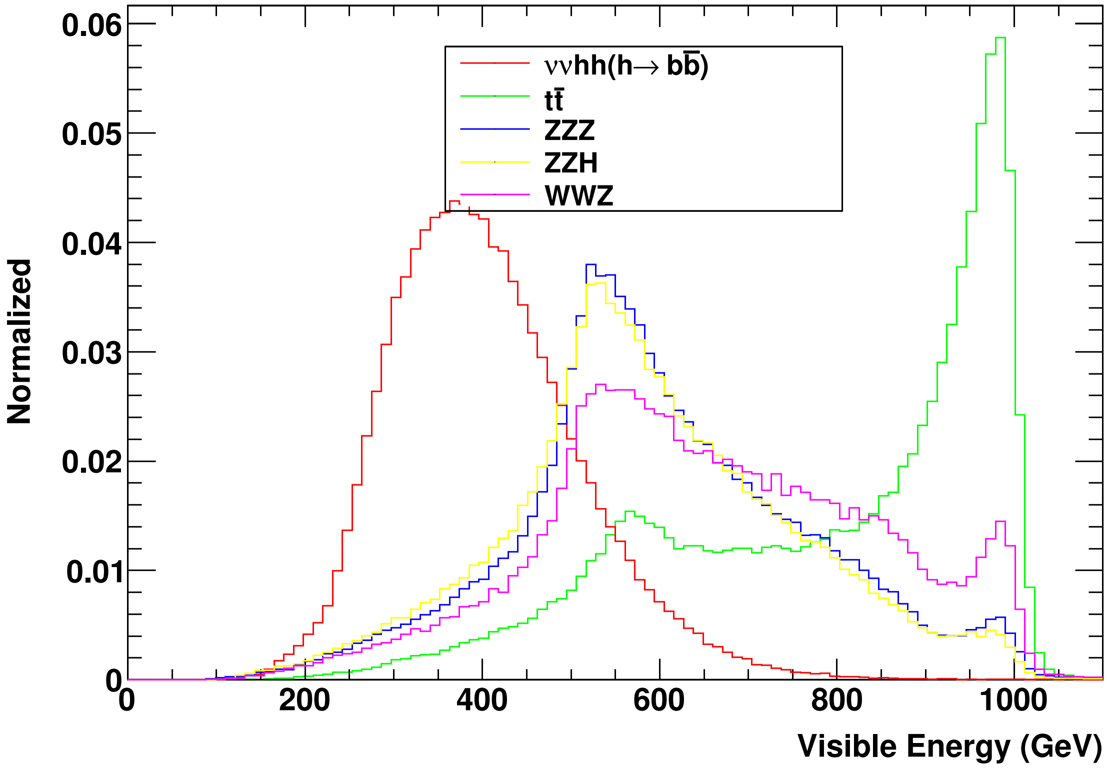

Figure 8.3: The distributions of visible energy for the signal: $\nu\nu$HH (red) and the backgrounds: $t\bar{t}$ (green), ZZZ (blue), ZZH (yellow) and WWZ (purple).

8.3.3 Backgrounds with the Same Final States

These backgrounds include $\nu\nu ZZ$ and $\nu\nu ZH$, which also come from WW fusion processes. The most useful quantities to suppress them are the invariant masses of jet pairs, which should be consistent with the Higgs mass. Another neural-net is thus trained with the following quantities as inputs, distributions of which are shown in Figure 8.6.

- Reconstructed Z and Higgs masses when paired under the $\nu\bar{\nu}ZH$ hypothesis, denoted by "mzzh" and "mhzh".
- Two Z masses re-reconstructed as from $\nu\bar{\nu}ZZ$, denoted by "mz1zz" and "mz2zz".
- Decay angles of H1 and H2. In the center of mass frame of each Higgs, the polar angle of one of the two jets measured from the parent Higgs momentum direction is defined as the decay angle of the Higgs. The absolute values of the two decay angles are used, denoted by "abs(cosj11h)" and "abs(cosj21h)".

For the neural-net training, a statistically independent $\nu\nu$HH signal and $\nu\nu ZZ$, $\nu\nu ZH$ background samples are used, each with statistics higher than 2 ab^{-1}. The neural-net outputs and the cut efficiencies for the signal and the background are shown in Figure 8.7. A tight cut on the neural-net output MLP$_{\nu\nu bbbb} > 0.6$ is used to suppress the same final state backgrounds, denoted by MLP2.

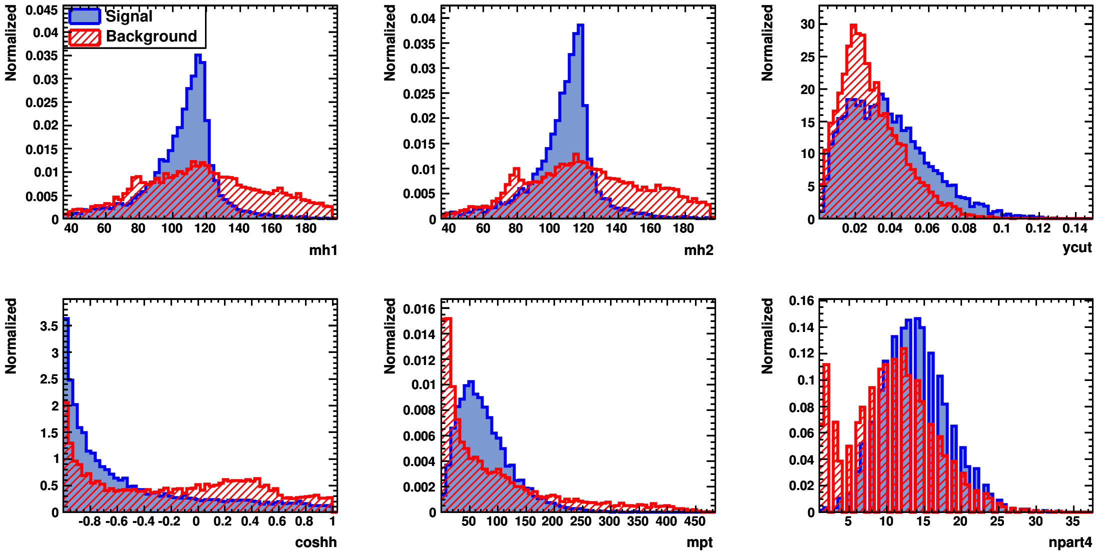

Figure 8.4: Discriminative quantities for the signal (blue) and the $t\bar{t}$ backgrounds (red). The variable names are explained in the text.

8.3.4 B Tagging Algorithm

As mentioned in Chap. 3, the b tagging algorithm used in fast simulation is much simplified. The criterion for tagging a jet is the number of off-vertex tracks belonging to that jet. The definition of the off-vertex track is based on a quantity called $Norm$:

$$Norm = \sqrt{\left(\frac{r}{\delta r}\right)^2 + \left(\frac{z}{\delta z}\right)^2} \tag{8.5}$$

where r and z are the coordinates of the point on the track which is closest to the beam axis in the cylindrical coordinates system, δr and δz are their measurement errors. This quantity reflects how many standard deviations the track is away from the interaction point and can be used to decide if the track is from the interaction point or from a secondary vertex. By introducing a cut $fNsigCut$, and demanding that $Norm$ is greater than $fNsigCut = 2.5$ we count off-vertex tracks.

The four jets are ordered by their numbers of off-vertex tracks in the descending order, denoted by $noff1 > noff2 > noff3 > noff4$. Figure 8.8 shows the distributions of the four numbers of off-vertex tracks. It turns out that $noff3$ and $noff4$ are the most discriminative. As the b tagging we require that at least three off-vertex tracks are contained in the third jet and at least one off-vertex track in the fourth jet, denoted by “Btagging”,

$$noff3 > 2, \quad noff4 > 0 \tag{8.6}$$

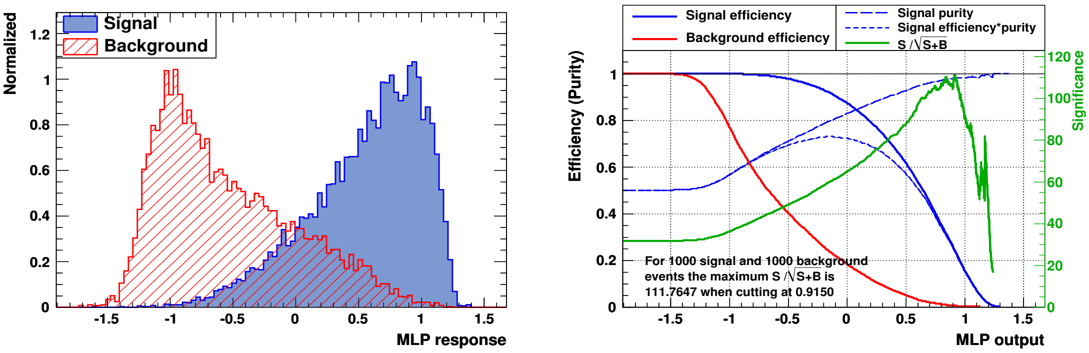

Figure 8.5: (left): The neural-net output for the signal versus the $t\bar{t}$ background, where the blue histogram is for the signal and the red one is for $t\bar{t}$. (right): The cut efficiencies of the signal and the background at different cut values on the neural-net output, where the solid blue curve is for the signal and the red one is for $t\bar{t}$.

8.4 Results and Conclusion

The numbers of the remaining signal and background events after the final selection are shown in the reduction table 8.3 in the case of no beam polarization. The main backgrounds are $t\bar{t}$, $\nu\nu ZZ$ and $\nu\nu ZH$. The other backgrounds are negligible. It is expected to obtain 6.0 signal evens, 5.6 of which come from the contribution of $\nu\nu$HH $\to$ $\nu\nu bbbb$, and 3.9 background events, corresponding to the $\nu\nu$HH excess significance of 2.4σ and the measurement significance of 1.9σ.

Table 8.3: The reduction table for the signal and backgrounds after the final selection. The cut names are explained in the text.

Process	Expected	pre-selection	Cut1	MLP1	MLP2	Btagging	Cut2
$\nu_e\bar{\nu}_e$HH $(\nu\nu bbbb)$	143 (63.4)	116 (61.1)	111 (58.3)	33.0 (20.7)	20.6 (12.8)	6.17 (5.80)	5.95 (5.62)
$t\bar{t}$	377600	160971	32326	377	183	3.78	1.51
W^+W^-Z	123400	27772	11512	57.5	17.0	0	0
ZZZ	1664	609	330	1.95	0.45	0.02	0.02
ZZH	700	240	135	2.42	0.60	0.05	0.04
$\nu_e\bar{\nu}_e ZZ$	12100	6112	5932	140	6.32	0.36	0.36
$\nu_e\bar{\nu}_e ZH$	2500	1620	1548	160	22.0	2.16	2.04
$\nu_e\bar{\nu}_e W^+W^-$	30200	14048	13626	172	4.83	0	0
$t\bar{t}H$	4960	184	89.2	2.38	1.78	0.40	0.20

From the fast simulation study of the WW fusion process $e^+ + e^- \to \nu_e\bar{\nu}_e$HH $\to$ $\nu_e\bar{\nu}_e b\bar{b}b\bar{b}$ at 1 TeV, assuming the Higgs mass of 120 GeV and the integrated luminosity of 2 ab^{-1}, without initial beam polarization, we thus expect a 2.4σ significance to observe $\nu\bar{\nu}$HH events and a 1.9σ significance for the measurement. The cross section of $\nu\bar{\nu}$HH can be measured to a precision of $\frac{\sqrt{6.0+3.9}}{6.0} = 52\%$, corresponding to a 44% precision for the Higgs self-coupling.

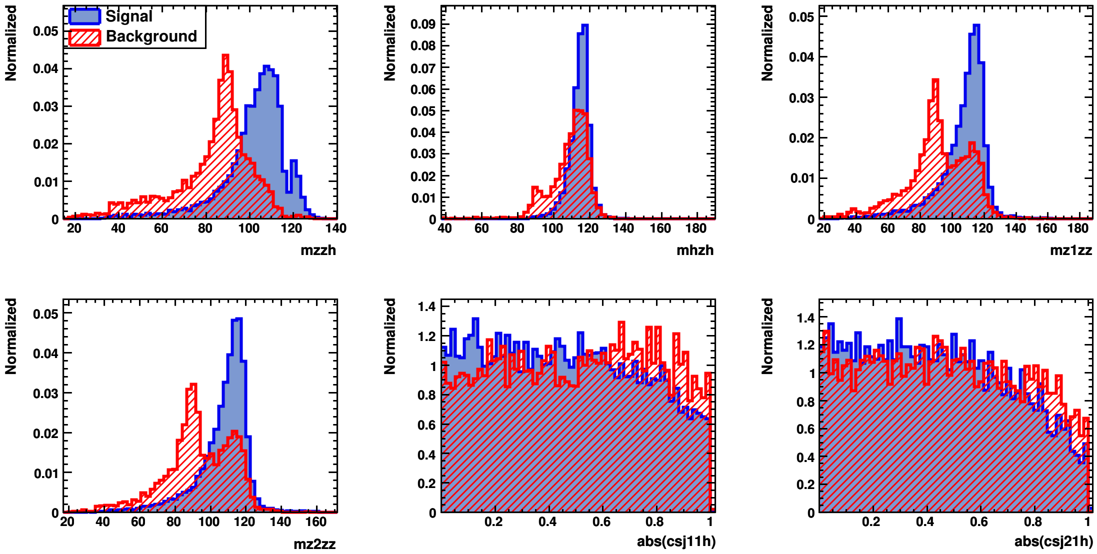

Figure 8.6: Discriminative quantities for the signal (blue) and the same final states backgrounds $\nu\nu ZZ$, $\nu\nu ZH$ (red). The variable names are explained in the text.

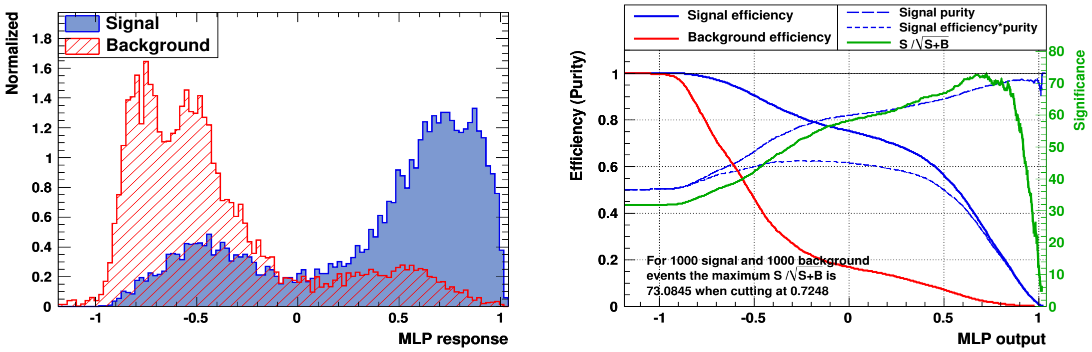

Figure 8.7: (left): The neural-net output for the signal versus $\nu\nu ZZ$, $\nu\nu ZH$ backgrounds, where the blue histogram is for the signal and the red one is for $\nu\nu ZZ$ and $\nu\nu ZH$. (right): The cut efficiencies of the signal and the background at different cut values on the neural-net output, where the solid blue curve is for the signal and the red one is for $\nu\nu ZZ$, $\nu\nu ZH$.

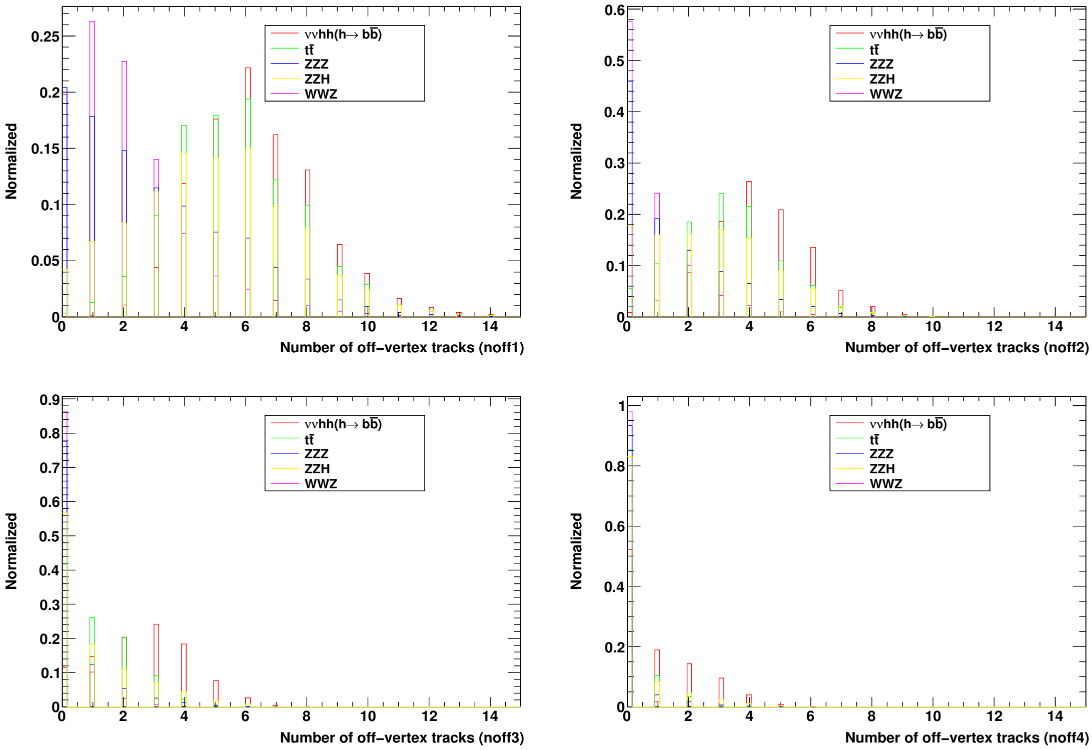

Figure 8.8: Distributions of the four numbers of off-vertex tracks, top left for noff1, top right for noff2, bottom left for noff3 and bottom right for noff4. The red histograms are for the signal, blue for ZZZ, green for $t\bar{t}$, yellow for ZZH and purple for WWZ.

Chapter 9

Conclusions

9.1 Full Simulation at 500 GeV

The decay modes of $e^+ + e^- \rightarrow$ ZHH at 500 GeV have been fully simulated to test the feasibility of the trilinear Higgs self-coupling measurement. This is the first full simulation study of the Higgs self-coupling measurement with all the three search modes analyzed together. And essentially all the possible standard model background processes have been considered in this study by using the huge common background samples prepared for the world-wide LoI studies. Assuming an integrated luminosity of 2 ab^{-1} and the Higgs mass of 120 GeV, in the case of left handed beam polarization, the combined result shows that an excess of ZHH events with 3.9σ significance can be observed, and the measurement of ZHH cross section with precision of 32% can be achieved. Hence the trilinear Higgs self-coupling can be determined to the precision of 57%, the first time that demonstrated the feasibility of the self-coupling measurement at 500 GeV based on full simulation. This result is much larger than that in study using fast simulation [43], where a 10% cross section measurement at an 18% Higgs self-coupling measurement were reported. Although the present analysis can be improved (see next paragraph), the main difference is probably due to the more background processes considered here and the fact that the fast simulation used there was still in an early stage of development and didn't include all detector effects, which can make the performances of single particle reconstruction, mass resolution and b tagging worse. However, this result is much better than that in study of full simulation [45], where the cross section is determined to the precision of 90%. The improvement is due to the inclusion of two decay modes of $e^+ + e^- \rightarrow$ ZHH in addition to the qqHH mode, better b tagging performance on ILD detector concept than LDC, and the sophisticated neural-net analyses. Nevertheless, the precision on Higgs self-coupling obtained in this thesis is already valuable for some new physics models [34][35], where trilinear Higgs self-coupling could deviate more than 100% from that predicted by the Standard Model.

B tagging, jet clustering and jets pairing are especially important to the three analyses. Prospects are that current technologies used for this thesis of these three algorithm can be improved. First, the neural-net for flavour tagging is trained using $Z \rightarrow q\bar{q}$ events at the center of mass energy of Z pole, where the energy of each jet is around 45 GeV. However, for ZHH events the average energy of each jet is about 70

GeV. Improvement of flavour tagging could be obtained by training the neural-net at center of mass energy of 140 GeV [75]. Second, in current jet clustering algorithm, tracks from same vertex of b parton can be clustered into different jets, making the b tagging performance in multi-jets events worse. A possible improvement is to force the tracks from same vertex to inside one jet. Third, as indicated in Chapter 8, the efficiency of correct-jet pairing can be improved by introducing more sophisticated probability density function of invariant mass by kernel estimation. Through these improvements, more accurate measurement of Higgs self-coupling at ILC would be possible.

9.2 Fast Simulation at 1 TeV

The possibility of measuring the trilinear Higgs self-coupling through WW fusion process at 1 TeV was investigated. Assuming an integrated luminosity of 2 ab^{-1} and Higgs mass of 120 GeV, without beam polarization, the result shows that excess of $\nu\nu$HH events with 2.4σ significance can be observed, and $\nu\nu$HH cross section can be measured to the precision of 52%. Benefitting from the smaller factor between the precision of the cross section and the precision of the Higgs self-coupling (Eqns. 2.32 and 2.33) the Higgs self-coupling can be measured to the precision of 44%. This result is larger than that in Ref. [47], which predicts a 12% precision on the Higgs self-coupling with 1 ab^{-1} data. This different is mainly due to the fact that Ref. [47] is based on a parton-level smearing, without parton showering and hadronizatio, and therefor doesn't include the effect of jet clustering. Another reason is that more background processes have been considered here.

Determining the Higgs self-coupling will be a challenging measurement at the ILC. By combining all the data collected at 500 GeV and 1 TeV, it will be possible to make an excellent trilinear Higgs self-coupling measurement and reveal the nature of electroweak symmetry breaking.

Bibliography

[1] "Strawman BCD, Baseline Configuration Document for ILC". http://lcdev.kek.jp/GDE/BCD/.

[2] **ILC Project**, J. Brau, Y. Okada, and N. Walker, eds., *ILC Reference Design Report Volume 1: Executive Summary*. 2007. arXiv:0712.1950 [physics.acc-ph]. ILC-REPORT-2007-001.

ILC Project, A. Djouadi *et al.*, eds., *International Linear Collider Reference Design Report Volume 2: Physics at the ILC*. 2007. arXiv:0709.1893 [hep-ph]. ILC-REPORT-2007-001.

ILC Project, N. Phinney, N. Toge, and N. Walker, eds., *ILC Reference Design Report Volume 3: Accelerator*. 2007. arXiv:0712.2361 [physics.acc-ph]. ILC-REPORT-2007-001.

ILC Project, T. Behnke *et al.*, eds., *International Linear Collider Reference Design Report Volume 4: Detectors*. 2007. arXiv:0712.2356 [physics.ins-det]. ILC-REPORT-2007-001.

[3] **ILD Concept Group - Linear Collider**, T. Abe *et al.*, "The International Large Detector: Letter of Intent" arXiv:1006.3396 [hep-ex].

[4] **The SiD Concept Group**, H. Aihara *et al.*, "SiD Letter of Intent" arXiv:0911.0006 [physics.ins-det].

[5] **GLD Concept Study Group**, K. Abe *et al.*, "GLD detector outline document" arXiv:physics/0607154.

[6] **LDC Working Group**, T. Behnke *et al.*, "The LDC detector concept" *Pramana* **69** (2007) 697–702.

[7] A. Mazzacane, "The 4th concept detector for the ILC" *Nucl.Instrum.Meth.* **A617** (2010) 173–176.

[8] P. W. Higgs, "Broken symmetries, massless particles and gauge fields" *Phys. Lett.* **12** (1964) 132–33.

P. W. Higgs, "BROKEN SYMMETRIES AND THE MASSES OF GAUGE BOSONS" *Phys. Rev. Lett.* **13** (1964) 508–509.

P. W. Higgs, "Spontaneous Symmetry Breakdown without Massless Bosons" *Phys. Rev.* **145** (1966) 1156–1163.

F. Englert and R. Brout, "BROKEN SYMMETRY AND THE MASS OF GAUGE VECTOR MESONS" *Phys. Rev. Lett.* **13** (1964) 321–322.

G. S. Guralnik, C. R. Hagen, and T. W. B. Kibble, "GLOBAL CONSERVATION LAWS AND MASSLESS PARTICLES" *Phys. Rev. Lett.* **13** (1964) 585–587.

[9] T. ALEPH, DELPHI, L3, O. Collaborations, and T. L. W. G. for Higgs Boson Searches, "Search for the standard model higgs boson at lep" *Physics Letters B* **565** (2003) 61 – 75.

[10] **CDF and D0**, T. Aaltonen *et al.*, "Combination of Tevatron searches for the standard model Higgs boson in the W+W- decay mode" *Phys. Rev. Lett.* **104** (2010) 061802, `arXiv:1001.4162 [hep-ex]`.

[11] ALEPH, CDF, D0, DELPHI, L3, OPAL, S. Collaborations, T. L. E. W. Group, T. T. E. W. Group, T. S. Electroweak, and H. F. Groups, "Precision Electroweak Measurements and Constraints on the Standard Model" `arXiv:0911.2604 [hep-ex]`.

[12] B. W. Lee, C. Quigg, and H. B. Thacker, "Weak Interactions at Very High-Energies: The Role of the Higgs Boson Mass" *Phys. Rev.* **D16** (1977) 1519.

[13] M. Luscher and P. Weisz, "Is There a Strong Interaction Sector in the Standard Lattice Higgs Model?" *Phys. Lett.* **B212** (1988) 472.

[14] U. M. Heller, M. Klomfass, H. Neuberger, and P. M. Vranas, "Numerical analysis of the Higgs mass triviality bound" *Nucl. Phys.* **B405** (1993) 555–573, `arXiv:hep-ph/9303215`.

[15] T. Hambye and K. Riesselmann, "Matching conditions and Higgs mass upper bounds revisited" *Phys. Rev.* **D55** (1997) 7255–7262, `arXiv:hep-ph/9610272`.

[16] K. G. Chetyrkin and M. Steinhauser, "The relation between the MS-bar and the on-shell quark mass at order alpha(s)**3" *Nucl. Phys.* **B573** (2000) 617–651, `arXiv:hep-ph/9911434`.

[17] A. H. Hoang *et al.*, "Top-antitop pair production close to threshold: Synopsis of recent NNLO results" *Eur. Phys. J. direct* **C2** (2000) 1, `arXiv:hep-ph/0001286`.

[18] M. Martinez and R. Miquel, "Multi-parameter fits to the t anti-t threshold observables at a future e+ e- linear collider" *Eur. Phys. J.* **C27** (2003) 49–55, `arXiv:hep-ph/0207315`.

[19] S. Heinemeyer, S. Kraml, W. Porod, and G. Weiglein, "Physics impact of a precise determination of the top quark mass at an e^+e^- linear collider" *JHEP* **09** (2003) 075, `arXiv:hep-ph/0306181`.

[20] “Understanding matter, energy, space and time: The case for the linear collider”. `http://physics.uoregon.edu/~lc/wwstudy/lc_consensus.html`.

[21] K. Fujii, D. J. Miller, and A. Soni, eds., *Linear Collider Physics In The New Millenium*. World Scienticifc, 2005.

[22] **SLAC-SP-017**, J. E. Augustin *et al.*, “Discovery of a Narrow Resonance in e+ e- Annihilation” *Phys. Rev. Lett.* **33** (1974) 1406–1408.

[23] I. Ginzburg, G. Kotkin, V. Serbo, and V. I. Telnov, “Production of High-Energy Colliding gamma gamma and gamma e Beams with a High Luminosity at Vlepp Accelerators” *JETP Lett.* **34** (1981) 491–495.

[24] E. Boos *et al.*, “Gold-plated processes at photon colliders” *Nucl. Instrum. Meth.* **A472** (2001) 100–120, `arXiv:hep-ph/0103090`.

[25] **LCTPC Collaboration**, “A TPC for a future linear collider”. LC-DET-2002-008, `http://www-flc.desy.de/lcnotes/notes/LC-DET-2002-008.ps.gz`.

[26] **CALICE Collaboration**, C. Adloff *et al.*, “CALICE Report to the Calorimeter R&D Review Panel” `arXiv:0707.1245 [physics.ins-det]`.

[27] M. Gell-Mann, “A Schematic Model of Baryons and Mesons” *Phys.Lett.* **8** (1964) 214–215.

H. Fritzsch, M. Gell-Mann, and H. Leutwyler, “Advantages of the Color Octet Gluon Picture” *Phys.Lett.* **B47** (1973) 365–368. Introduces the term ’color’.

D. Gross and F. Wilczek, “Ultraviolet Behavior of Nonabelian Gauge Theories” *Phys.Rev.Lett.* **30** (1973) 1343–1346.

H. Politzer, “Reliable Perturbative Results for Strong Interactions?” *Phys.Rev.Lett.* **30** (1973) 1346–1349.

[28] S. L. Glashow, “Partial Symmetries of Weak Interactions” *Nucl. Phys.* **22** (1961) 579–588.

S. Weinberg, “A Model of Leptons” *Phys. Rev. Lett.* **19** (1967) 1264–1266.

A. Salam in *Elementary Particle Theory*, S. N., Almqvist, Wiksells, and Stockholm, eds., p. 367. 1969.

[29] A. Djouadi, “The Anatomy of electro-weak symmetry breaking. II. The Higgs bosons in the minimal supersymmetric model” *Phys.Rept.* **459** (2008) 1–241, `arXiv:hep-ph/0503173 [hep-ph]`.

[30] **Particle Data Group**, K. Nakamura *et al.*, “Review of particle physics” *J. Phys.* **G37** (2010) 075021.

[31] N. Cabibbo, "Unitary Symmetry and Leptonic Decays" *Phys.Rev.Lett.* **10** (1963) 531–533.

M. Kobayashi and T. Maskawa, "CP Violation in the Renormalizable Theory of Weak Interaction" *Prog.Theor.Phys.* **49** (1973) 652–657.

[32] R. Behrends, R. Finkelstein, and A. Sirlin, "Radiative corrections to decay processes" *Phys.Rev.* **101** (1956) 866–873.

T. Kinoshita and A. Sirlin, "Radiative corrections to Fermi interactions" *Phys.Rev.* **113** (1959) 1652–1660.

T. van Ritbergen and R. G. Stuart, "Complete two loop quantum electrodynamic contributions to the muon lifetime in the Fermi model" *Phys.Rev.Lett.* **82** (1999) 488–491, `arXiv:hep-ph/9808283 [hep-ph]`.

[33] **LHC/LC Study Group**, G. Weiglein *et al.*, "Physics interplay of the LHC and the ILC" *Phys. Rept.* **426** (2006) 47–358, `arXiv:hep-ph/0410364`.

[34] S. Kanemura, S. Kiyoura, Y. Okada, E. Senaha, and C. Yuan, "New physics effect on the Higgs selfcoupling" *Phys.Lett.* **B558** (2003) 157–164, `arXiv:hep-ph/0211308 [hep-ph]`.

S. Kanemura, Y. Okada, E. Senaha, and C.-P. Yuan, "Higgs coupling constants as a probe of new physics" *Phys.Rev.* **D70** (2004) 115002, `arXiv:hep-ph/0408364 [hep-ph]`.

E. Asakawa, D. Harada, S. Kanemura, Y. Okada, and K. Tsumura, "Higgs boson pair production in new physics models at hadron, lepton, and photon colliders" *Phys.Rev.* **D82** (2010) 115002, `arXiv:1009.4670 [hep-ph]`.

A. Djouadi, W. Kilian, M. Muhlleitner, and P. M. Zerwas, "Testing Higgs Self-couplings at e+e- Linear Colliders" *Eur. Phys. J.* **C10** (1999) 27–43, `arXiv:hep-ph/9903229`.

[35] C. Grojean, G. Servant, and J. D. Wells, "First-order electroweak phase transition in the standard model with a low cutoff" *Phys.Rev.* **D71** (2005) 036001, `arXiv:hep-ph/0407019 [hep-ph]`.

S. Kanemura, Y. Okada, and E. Senaha, "Electroweak baryogenesis and quantum corrections to the triple Higgs boson coupling" *Phys.Lett.* **B606** (2005) 361–366, `arXiv:hep-ph/0411354 [hep-ph]`.

S. Ham and S. Oh, "Electroweak phase transition and Higgs self-couplings in the two-Higgs-doublet model" `arXiv:hep-ph/0502116 [hep-ph]`.

M. Aoki, S. Kanemura, and O. Seto, "Neutrino mass, Dark Matter and Baryon Asymmetry via TeV-Scale Physics without Fine-Tuning" *Phys.Rev.Lett.* **102** (2009) 051805, `arXiv:0807.0361 [hep-ph]`.

M. Aoki, S. Kanemura, and O. Seto, "A Model of TeV Scale Physics for Neutrino Mass, Dark Matter and Baryon Asymmetry and its Phenomenology" *Phys.Rev.* **D80** (2009) 033007, `arXiv:0904.3829 [hep-ph]`.

A. Noble and M. Perelstein, "Higgs self-coupling as a probe of electroweak phase transition" *Phys.Rev.* **D78** (2008) 063518, `arXiv:0711.3018 [hep-ph]`.

[36] A. G. Cohen, D. Kaplan, and A. Nelson, "Progress in electroweak baryogenesis" *Ann.Rev.Nucl.Part.Sci.* **43** (1993) 27–70, `arXiv:hep-ph/9302210 [hep-ph]`.

M. Quiros, "Field theory at finite temperature and phase transitions" *Helv.Phys.Acta* **67** (1994) 451–583.

V. Rubakov and M. Shaposhnikov, "Electroweak baryon number nonconservation in the early universe and in high-energy collisions" *Usp.Fiz.Nauk* **166** (1996) 493–537, `arXiv:hep-ph/9603208 [hep-ph]`.

[37] G. D. Kribs, T. Plehn, M. Spannowsky, and T. M. Tait, "Four generations and Higgs physics" *Phys.Rev.* **D76** (2007) 075016, `arXiv:0706.3718 [hep-ph]`.

[38] F. Gianotti, M. Mangano, T. Virdee, S. Abdullin, G. Azuelos, *et al.*, "Physics potential and experimental challenges of the LHC luminosity upgrade" *Eur.Phys.J.* **C39** (2005) 293–333, `arXiv:hep-ph/0204087 [hep-ph]`.

U. Baur, T. Plehn, and D. L. Rainwater, "Measuring the Higgs boson self coupling at the LHC and finite top mass matrix elements" *Phys.Rev.Lett.* **89** (2002) 151801, `arXiv:hep-ph/0206024 [hep-ph]`.

U. Baur, T. Plehn, and D. L. Rainwater, "Determining the Higgs boson selfcoupling at hadron colliders" *Phys.Rev.* **D67** (2003) 033003, `arXiv:hep-ph/0211224 [hep-ph]`.

U. Baur, T. Plehn, and D. L. Rainwater, "Probing the Higgs selfcoupling at hadron colliders using rare decays" *Phys.Rev.* **D69** (2004) 053004, `arXiv:hep-ph/0310056 [hep-ph]`.

U. Baur, T. Plehn, and D. L. Rainwater, "Examining the Higgs boson potential at lepton and hadron colliders: A Comparative analysis" *Phys.Rev.* **D68** (2003) 033001, `arXiv:hep-ph/0304015 [hep-ph]`.

[39] G. Gounaris, D. Schildknecht, and F. Renard, "TEST OF HIGGS BOSON NATURE IN e+ e- → H H Z" *Phys.Lett.* **B83** (1979) 191.

A. Djouadi, H. Haber, and P. Zerwas, "Multiple production of MSSM neutral Higgs bosons at high-energy e+ e- colliders" *Phys.Lett.* **B375** (1996) 203–212, `arXiv:hep-ph/9602234 [hep-ph]`.

V. Ilyin, A. Pukhov, Y. Kurihara, Y. Shimizu, and T. Kaneko, "Probing the H**3 vertex in e+ e-, gamma e and gamma gamma collisions for light and intermediate Higgs bosons" *Phys.Rev.* **D54** (1996) 6717–6727, `arXiv:hep-ph/9506326 [hep-ph]`.

[40] V. D. Barger and T. Han, "DOUBLE HIGGS BOSON PRODUCTION VIA W W FUSION IN TeV e+ e- COLLISIONS" *Mod.Phys.Lett.* **A5** (1990) 667–674.

F. Boudjema and E. Chopin, “Double Higgs production at the linear colliders and the probing of the Higgs selfcoupling” *Z.Phys.* **C73** (1996) 85–110, `arXiv:hep-ph/9507396 [hep-ph]`.

[41] Y. Yasui *et al.*, “Measurement of the Higgs self-coupling at JLC” `arXiv:hep-ph/0211047`.

[42] A. Djouadi, J. Kalinowski, and M. Spira, “HDECAY: A Program for Higgs boson decays in the standard model and its supersymmetric extension” *Comput.Phys.Commun.* **108** (1998) 56–74, `arXiv:hep-ph/9704448 [hep-ph]`.

[43] C. Castanier, P. Gay, P. Lutz, and J. Orloff, “Higgs self coupling measurement in e+ e- collisions at center-of-mass energy of 500-GeV” `arXiv:hep-ex/0101028 [hep-ex]`.

[44] T. Barklow, “Higgs self-coupling measurement”. Presentation for LCWS07.

[45] M. F. Giannelli, “Sensitivity to the Higgs Self-coupling Using the ZHH Channel” `arXiv:0901.4895 [hep-ex]`.

[46] Y. Takubo, “Analysis of Higgs Self-coupling with ZHH at ILC” `arXiv:0907.0524 [hep-ph]`.

Y. Takubo, “Analysis of ZHH in the 4-jet mode” `arXiv:0901.3598 [hep-ph]`.

J. Tian, K. Fujii, and Y. Gao, “Study of Higgs Self-coupling at ILC” `arXiv:1008.0921 [hep-ex]`.

[47] S. Yamashita, “A study of Higgs self-coupling measurement at about 1 TeV”. Presentation for LCWS04.

[48] P. Mora de Freitas and H. Videau, “Detector simulation with MOKKA / GEANT4: Present and future”. Prepared for International Workshop on Linear Colliders (LCWS 2002), Jeju Island, Korea, 26-30 Aug 2002.

`http://ilcsoft.desy.de/portal/software_packages/mokka/`.

[49] F. Gaede, “Marlin and LCCD: Software tools for the ILC” *Nucl. Instrum. Meth.* **A559** (2006) 177–180.

[50] L. Garren and P. Lebrun, “STDHEP webpage”. `http://cepa.fnal.gov/psm/stdhep/`.

[51] F. Gaede, T. Behnke, N. Graf, and T. Johnson, “LCIO: A persistency framework for linear collider simulation studies” *Proceedings of CHEP 03, La Jolla, California, 24-28 Mar 2003, TUKT001* (2003) , `arXiv:physics/0306114`.

[52] W. Kilian, T. Ohl, and J. Reuter, “WHIZARD: Simulating Multi-Particle Processes at LHC and ILC” `arXiv:0708.4233 [hep-ph]`.

[53] T. Ohl, "O'Mega and WHIZARD: Monte Carlo event generator generation for future colliders" `arXiv:hep-ph/0011287 [hep-ph]`.

T. Ohl, "O'mega: An Optimizing matrix element generator" *AIP Conf.Proc.* **583** (2001) 173–175, `arXiv:hep-ph/0011243 [hep-ph]`.

M. Moretti, T. Ohl, and J. Reuter, "O'Mega: An Optimizing matrix element generator" `arXiv:hep-ph/0102195 [hep-ph]`.

[54] T. Stelzer and W. Long, "Automatic generation of tree level helicity amplitudes" *Comput.Phys.Commun.* **81** (1994) 357–371, `arXiv:hep-ph/9401258 [hep-ph]`.

[55] A. Pukhov, E. Boos, M. Dubinin, V. Edneral, V. Ilyin, *et al.*, "CompHEP: A Package for evaluation of Feynman diagrams and integration over multiparticle phase space" `arXiv:hep-ph/9908288 [hep-ph]`. User's manual for version 33.

CompHEP Collaboration, E. Boos *et al.*, "CompHEP 4.4: Automatic computations from Lagrangians to events" *Nucl.Instrum.Meth.* **A534** (2004) 250–259, `arXiv:hep-ph/0403113 [hep-ph]`.

[56] T. Ohl, "Vegas revisited: Adaptive Monte Carlo integration beyond factorization" *Comput.Phys.Commun.* **120** (1999) 13–19, `arXiv:hep-ph/9806432 [hep-ph]`.

[57] T. Sjostrand, S. Mrenna, and P. Z. Skands, "PYTHIA 6.4 Physics and Manual" *JHEP* **0605** (2006) 026, `arXiv:hep-ph/0603175 [hep-ph]`.

[58] **GEANT4 Collaboration**, S. Agostinelli *et al.*, "GEANT4: A simulation toolkit" *Nucl. Instrum. Meth.* **A506** (2003) 250–303.

[59] F. Gaede *et al.*, "MarlinReco webpage". `http://ilcsoft.desy.de/portal/software_packages/marlinreco`.

[60] **ALEPH Collaboration**, D. Buskulic *et al.*, "Performance of the ALEPH detector at LEP" *Nucl.Instrum.Meth.* **A360** (1995) 481–506.

[61] I. Knowles and G. Lafferty, "Hadronization in Z^0 decay" *J.Phys.G* **G23** (1997) 731–789, `arXiv:hep-ph/9705217 [hep-ph]`.

[62] V. Morgunov, "Energy flow method for multi - jet effective mass reconstruction in the highly granulated TESLA calorimeter".

A. Raspereza, "Modular implementation of particle flow algorithm with minimized dependence on the detector geometry" `arXiv:physics/0601069 [physics]`.

M. Charles, "PFA Performance for SiD" `arXiv:0901.4670 [physics.data-an]`.

[63] M. Thomson, "Particle Flow Calorimetry and the PandoraPFA Algorithm" *Nucl.Instrum.Meth.* **A611** (2009) 25–40, `arXiv:0907.3577 [physics.ins-det]`.

[64] **LCFI**, . D. Bailey *et al.*, “The LCFIVertex package: vertexing, flavour tagging and vertex charge reconstruction with an ILC vertex detector” *Nucl. Instrum. Meth.* **A610** (2009) 573–589, `arXiv:0908.3019 [physics.ins-det]`.

[65] **JADE**, S. Bethke *et al.*, “Experimental Investigation of the Energy Dependence of the Strong Coupling Strength” *Phys. Lett.* **B213** (1988) 235.

[66] S. Bethke, Z. Kunszt, D. Soper, and W. Stirling, “New jet cluster algorithms: Next-to-leading order QCD and hadronization corrections” *Nucl.Phys.* **B370** (1992) 310–334.

[67] `http://www-jlc.kek.jp/subg/offl/jsf/`.

[68] `http://www-jlc.kek.jp/subg/offl/physsim/`.

[69] H. Murayama, I. Watanabe, and K. Hagiwara, “HELAS: HELicity amplitude subroutines for Feynman diagram evaluations”.

[70] S. Kawabata, “A New Monte Carlo Event Generator for High-Energy Physics” *Comput. Phys. Commun.* **41** (1986) 127.

[71] `http://acfahep.kek.jp/subg/sim/simtools/`.

[72] K. Ikematsu, A. Miyamoto, and K. Fujii, “Feasibility study of the forward-backward asymmetry of the e+e- -¿ t t-bar process in all-hadronic decay modes at sqrt(s) = 500-DeV with the ILD detector” `arXiv:1005.4635 [hep-ex]`.

[73] P. Speckmayer, A. Hocker, J. Stelzer, and H. Voss, “The toolkit for multivariate data analysis, TMVA 4” *J.Phys.Conf.Ser.* **219** (2010) 032057.

[74] M. W. Grunewald *et al.*, “Four-fermion production in electron positron collisions” `arXiv:hep-ph/0005309`.

[75] Y. Takubo, “ZHH analysis with ILD”. `http://neutrino.kek.jp/~takubo/zhh_takubo091001.pdf`. Presentation for ALCPG09.

[76] **BES Collaboration**, M. Ablikim *et al.*, “Study of J/Psi decays into eta K*0 anti-K*0” *Phys.Lett.* **B685** (2010) 27–32, `arXiv:0909.2087 [hep-ex]`.

[77] **BABAR Collaboration**, B. Aubert *et al.*, “A Structure at 2175-MeV in $e^+e^- \to \phi$ f0(980) Observed via Initial-State Radiation” *Phys.Rev.* **D74** (2006) 091103, `arXiv:hep-ex/0610018 [hep-ex]`.

[78] **BES Collaboration**, M. Ablikim *et al.*, “Observation of Y(2175) in J / psi → eta phi f(0)(980)” *Phys.Rev.Lett.* **100** (2008) 102003, `arXiv:0712.1143 [hep-ex]`.

[79] **Belle Collaboration**, C. Shen *et al.*, “Observation of the phi(1680) and the Y(2175) in e+e- → phi pi+ pi-” *Phys.Rev.* **D80** (2009) 031101, `arXiv:0808.0006 [hep-ex]`.

[80] **BABAR Collaboration**, B. Aubert *et al.*, “Observation of a broad structure in the $\pi^+\pi^- J/\psi$ mass spectrum around 4.26-GeV/c^2” *Phys.Rev.Lett.* **95** (2005) 142001, `arXiv:hep-ex/0506081 [hep-ex]`.

[81] S.-L. Zhu, “The Possible interpretations of Y(4260)” *Phys.Lett.* **B625** (2005) 212, `arXiv:hep-ph/0507025 [hep-ph]`.

[82] F. E. Close and P. R. Page, “Gluonic charmonium resonances at BaBar and BELLE?” *Phys.Lett.* **B628** (2005) 215–222, `arXiv:hep-ph/0507199 [hep-ph]`.

[83] E. Kou and O. Pene, “Suppressed decay into open charm for the Y(4260) being an hybrid” *Phys.Lett.* **B631** (2005) 164–169, `arXiv:hep-ph/0507119 [hep-ph]`.

[84] F. J. Llanes-Estrada, “Y(4260) and possible charmonium assignment” *Phys.Rev.* **D72** (2005) 031503, `arXiv:hep-ph/0507035 [hep-ph]`.

[85] L. Maiani, V. Riquer, F. Piccinini, and A. Polosa, “Four quark interpretation of Y(4260)” *Phys.Rev.* **D72** (2005) 031502, `arXiv:hep-ph/0507062 [hep-ph]`.

[86] C.-F. Qiao, “One explanation for the exotic state Y(4260)” *Phys.Lett.* **B639** (2006) 263–265, `arXiv:hep-ph/0510228 [hep-ph]`.

[87] G.-J. Ding and M.-L. Yan, “A Candidate for 1– strangeonium hybrid” *Phys.Lett.* **B650** (2007) 390–400, `arXiv:hep-ph/0611319 [hep-ph]`.

[88] G.-J. Ding and M.-L. Yan, “Y(2175): Distinguish Hybrid State from Higher Quarkonium” *Phys.Lett.* **B657** (2007) 49–54, `arXiv:hep-ph/0701047 [hep-ph]`.

[89] Z.-G. Wang, “Analysis of the Y(2175) as a tetraquark state with QCD sum rules” *Nucl.Phys.* **A791** (2007) 106–116, `arXiv:hep-ph/0610171 [hep-ph]`.

[90] **BES Collaboration**, J. Bai *et al.*, “The BES upgrade” *Nucl.Instrum.Meth.* **A458** (2001) 627–637.

[91] **BES Collaboration**, M. Ablikim *et al.*, “BESII detector simulation” *Nucl.Instrum.Meth.* **A552** (2005) 344–356, `arXiv:physics/0503001 [physics]`.

[92] S. Fang *et al. High Energy Phys. Nucl. Phys.* **A27** (2003) 277.

[93] **BABAR Collaboration**, B. Aubert *et al.*, “The e+ e- → 2(pi+ pi-) pi0, 2(pi+ pi-) eta, K+ K- pi+ pi- pi0 and K+ K- pi+ pi- eta Cross Sections Measured with Initial-State Radiation” *Phys.Rev.* **D76** (2007) 092005, `arXiv:0708.2461 [hep-ex]`.

[94] **Particle Data Group**, C. Amsler *et al.*, "Review of Particle Physics" *Phys.Lett.* **B667** (2008) 1–1340.

[95] **BES Collaboration**, M. Ablikim *et al.*, "Observation of a broad 1– resonant structure around 1.5-GeV/c**2 in the K+ K- mass spectrum in J/psi → K+ K- pi0" *Phys.Rev.Lett.* **97** (2006) 142002, `arXiv:hep-ex/0606047 [hep-ex]`.

[96] D. Aston, N. Awaji, T. Bienz, F. Bird, J. D'Amore, *et al.*, "A Study of K- pi+ Scattering in the Reaction K- p → K- pi+ n at 11-GeV/c" *Nucl.Phys.* **B296** (1988) 493.

Appendix A

Study of J/ψ decays into $\eta K^{*0}\overline{K}^{*0}$

This analysis is published in [76].

A.1 Introduction

Following the observation of $Y(2175)$ by the BaBar Collaboration in $e^+e^- \to \gamma_{ISR}\phi f_0(980)$ via initial-state radiation [77], the resonance was observed by the BES Collaboration in $J/\psi \to \eta\phi f_0(980)$ [78] and more recently by the Belle Collaboration in $e^+e^- \to \gamma_{ISR}\phi\pi^+\pi^-$ [79]. Since both the $Y(2175)$ and $Y(4260)$ [80] are observed in e^+e^- annihilation via initial-state radiation and these two resonances have similar decay modes, it was speculated that $Y(2175)$ may be an s-quark version of $Y(4260)$ [77]. There have been a number of different interpretations proposed for the $Y(4260)$, that include a $gc\bar{c}$ hybrid [81] [82] [83], a 4^3S_1 $c\bar{c}$ state [84], a $[cs]_S[\bar{c}\bar{s}]_S$ tetraquark state [85], or a baryonium [86]. Likewise $Y(2175)$ has been correspondingly interpreted as: a $gs\bar{s}$ hybrid [87], a 2^3D_1 $s\bar{s}$ state [88], or a $s\bar{s}s\bar{s}$ tetraquark state [89]. None of these interpretations has either been established or ruled out by experimental observations.

According to Ref. [88], a hybrid state may have very different decay patterns compared to a quarkonium state. Measuring the branching fractions of some decay modes may shed light on understanding the nature of $Y(2175)$. Among those promising decay modes, $Y(2175) \to K^{*0}\overline{K}^{*0}$ is of special importance. This decay mode is forbidden if $Y(2175)$ is a hybrid state but allowed if it is a quarkonium state.

On the other hand, there are still lots of unknown decay modes of J/ψ and investigating more of them is useful to understand the mechanism of J/ψ decays. Based on a sample of 58M J/ψ events collected by the BESII detector at the Beijing Electron-Positron Collider (BEPC), a search for the process $J/\psi \to \eta Y(2175), Y(2175) \to K^{*0}\overline{K}^{*0}$ is performed. In addition, the first measurement of the branching fraction $\mathrm{Br}(J/\psi \to \eta K^{*0}\overline{K}^{*0})$ is obtained.

A.2 Detector and data samples

The upgraded Beijing Spectrometer detector (BESII) was located at the Beijing Electron-Positron Collider (BEPC). BESII was a large solid-angle magnetic spectrometer which is described in detail in Ref. [90]. The momentum of charged particles is determined by a 40-layer cylindrical main drift chamber (MDC) which has a momentum resolution of σ_p/p=1.78%$\sqrt{1+p^2}$ (p in GeV/c). Particle identification is accomplished using specific ionization (dE/dx) measurements in the drift chamber and time-of-flight (TOF) information in a barrel-like array of 48 scintillation counters. The dE/dx resolution is $\sigma_{dE/dx} \simeq 8.0\%$; the TOF resolution for Bhabha events is $\sigma_{TOF} = 180$ ps. Radially outside of the time-of-flight counters is a 12-radiation-length barrel shower counter (BSC) comprised of gas tubes interleaved with lead sheets. The BSC measures the energy and direction of photons with resolutions of $\sigma_E/E \simeq 21\%/\sqrt{E}$ (E in GeV), $\sigma_\phi = 7.9$ mrad, and $\sigma_z = 2.3$ cm. The iron flux return of the magnet is instrumented with three double layers of proportional counters that are used to identify muons.

A GEANT3 based Monte Carlo (MC) package (SIMBES) [91] with detailed consideration of real detector performance (such as dead electronic channels) is used. The consistency between data and Monte Carlo has been carefully checked in many high purity physics channels, and the agreement is quite reasonable [91].

A.3 Analysis

The decay channel under investigation, $J/\psi \to \eta K^{*0}\overline{K}^{*0}, \eta \to \gamma\gamma, K^{*0} \to K^+\pi^-, \overline{K}^{*0} \to K^-\pi^+$, has two charged kaons, two charged pions, and two photons in its final state. A candidate event is therefore required to have four good charged tracks reconstructed in the MDC with net charge zero and at least two isolated photons in the BSC. A good charged track is required to (1) be well fitted to a three dimensional helix in order to ensure a correct error matrix in the kinematic fit; (2) originate from the interaction region, i.e. the point of closest approach of the track to the beam axis is within 2 cm of the beam axis and within 20 cm from the center of the interaction region along the beam line; (3) have a polar angle θ, within the range $|\cos\theta| < 0.8$; and (4) have a transverse momentum greater than 70 MeV/c. The TOF and dE/dx information is combined to form a particle identification confidence level for the π, K, and p hypotheses, and the particle type with the highest confidence level is assigned to each track. The four charged tracks selected are further required to be consistent with an unambiguously identified $K^+\pi^+K^-\pi^-$ combination. An isolated neutral cluster is considered as a good photon when (1) the energy deposited in the BSC is greater than 60 MeV, (2) the angle between the nearest charged track and the cluster is greater than 15°, (3) the angle between the cluster development direction in the BSC and the photon emission direction is less than 30°, and (4) at least two layers have deposits in the BSC and the first hit is in the beginning six layers. A four-constraint (4-C) kinematic fit is performed to the hypothesis $J/\psi \to \gamma\gamma K^+K^-\pi^+\pi^-$, and if there are more than two good photons, the combination with the smallest $\chi^2_{\gamma\gamma K^+K^-\pi^+\pi^-}$ value is selected. We further require that $\chi^2_{\gamma\gamma K^+K^-\pi^+\pi^-} < 20$. Because we are not interest in the events of which the two photons come from π^0, we require the invariant mass of two photons to be greater than 0.3 GeV/c^2.

A.3.1 Branching fraction of $J/\psi \to \eta K^{*0}\overline{K}^{*0}$

After applying the above event selection criteria, Fig. A.1(a) shows the scatter plot of $M_{K^+\pi^-}$ versus $M_{K^-\pi^+}$. One can see $K^{*0}\overline{K}^{*0}$, $K^{*0}K^-\pi^+$, $\overline{K}^{*0}K^+\pi^-$, and $K^+\pi^-K^-\pi^+$ events scattered in different regions of the plot. The signal region in this analysis is defined by $|M_{K^\pm\pi^\mp} - m_{K^{*0}}(m_{\overline{K}^{*0}})| < 0.05$ GeV/c^2, which is shown as the middle box in Fig. A.1(a). Other boxes shown are side-band regions, and events in these regions are used to estimate the background in the signal region. The $K^\pm\pi^\mp$ invariant mass spectra are shown in Fig. A.1(b), where the solid histogram is $K^+\pi^-$ and the dashed histogram is $K^-\pi^+$. Figure A.2(a) shows the $\gamma\gamma$ invariant mass spectrum for events in the signal region, where an η is seen. In Fig. A.2(a), the shaded histogram is the spectrum obtained requiring two good photons, while the dashed histogram is the spectrum for more than two photons. When there are more than two photons, the ratio of signal over background is much lower. In order to remove potential backgrounds as much as possible, we also require the number of good photons to be two.

Figure A.2(b) shows the $\gamma\gamma$ invariant mass spectrum of events surviving the above selection, while the shaded histogram is the normalized background estimated using the side-band regions shown in Fig. A.1(a). The number of $J/\psi \to \eta K^{*0}\overline{K}^{*0}$ events is determined by fitting the spectra in Fig. A.2(b). The $J/\psi \to \eta K^{*0}\overline{K}^{*0}$ branching fraction is determined using

$$Br(J/\psi \to \eta K^{*0}\overline{K}^{*0}) = \frac{N_{sig}-N_{sb}}{N_{J/\psi}\cdot\epsilon\cdot Br(K^{*0}\to K^+\pi^-)\cdot Br(\overline{K}^{*0}\to K^-\pi^+)\cdot Br(\eta\to\gamma\gamma)},$$

where $N_{sig} = 347$ is the number of events in the signal region, obtained by fitting the spectrum in Fig. A.2(b) (the blank histogram); $N_{sb} = 138$ is the number of background events estimated from side-band regions, obtained by fitting the spectrum in Fig. A.2(b) (the shaded histogram); $N_{J/\psi}$ is the total number of J/ψ events [92]; $\epsilon = 1.79\%$ is the detection efficiency obtained from MC simulation of $J/\psi \to \eta K^{*0}\overline{K}^{*0}$; and $Br(K^{*0} \to K^+\pi^-)$, $Br(\overline{K}^{*0} \to K^-\pi^+)$ and $Br(\eta \to \gamma\gamma)$ are the corresponding branching fractions. Figures A.3(a) and A.3(b) show respectively the fitting results of the signal and side-band events, where the shape of the $\gamma\gamma$ invariant mass spectrum obtained from the MC sample $J/\psi \to \eta K^{*0}\overline{K}^{*0}$ is used as the signal shape and a third order Chebyshev polynomial is used as the background shape. The $J/\psi \to \eta K^{*0}\overline{K}^{*0}$ branching fraction is determined to be

$$Br(J/\psi \to \eta K^{*0}\overline{K}^{*0}) = (1.15 \pm 0.13) \times 10^{-3},$$

where the error is statistical only. It is the first measurement for this decay mode of J/ψ and it is shown that this mode is a typical three bodies decay. The branching fraction is compatible with the result of $Br(J/\psi \to \eta K^+K^-\pi^+\pi^-) = (1.84 \pm 0.28) \times 10^{-3}$ given by BaBar Collaboration [93]. It is worth mention of that this branching fraction is several times smaller than the radiative decay mode $J/\psi \to \gamma K^{*0}\overline{K}^{*0}$ which is very different from the situation of $p\bar{p}$ that the branching fraction of $J/\psi \to \eta p\bar{p}$ is much bigger than $J/\psi \to \gamma p\bar{p}$.

A.3.2 $J/\psi \to \eta Y(2175) \to \eta K^{*0}\overline{K}^{*0}$

Next, we search for a possible resonance recoiling against η. So in addition to the above requirements, we require that the $\gamma\gamma$ invariant mass satisfies $|M_{\gamma\gamma} - m_\eta| <$

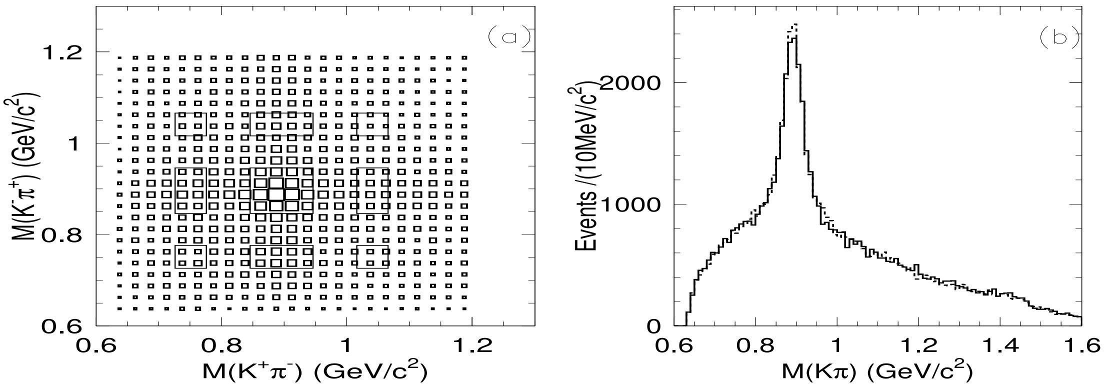

Figure A.1: (a) Scatter plot of $M_{K^+\pi^-}$ versus $M_{K^-\pi^+}$ invariant mass, where the middle box is the signal region and the other boxes are the side-band regions. (b) The invariant mass spectra of $K^\pm\pi^\mp$; the solid histogram is $K^+\pi^-$ and the dashed is $K^-\pi^+$.

0.04 GeV/c^2 and define the side-band region to be 0.1 GeV/c^2 $< |M_{\gamma\gamma} - m_\eta| <$ 0.14 GeV/c^2. The $K^{*0}\overline{K}^{*0}$ invariant mass spectrum recoiling against η for $J/\psi \to \eta K^{*0}\overline{K}^{*0}$ is shown in Fig. A.4, where the dashed histogram is the contribution from phase space for $J/\psi \to \eta K^{*0}\overline{K}^{*0}$ and the shaded histogram is the contribution from the normalized side-band events in the η, K^{*0} and $\overline{K}^{*0}$ side-band regions. There is no obvious enhancement in the region around 2.175 GeV/c^2.

The backgrounds in the selected event sample are studied with MC simulations. For the decay $J/\psi \to \eta K^{*0}\overline{K}^{*0}$, the possible main background channels are: $J/\psi \to \eta K^{*0}\overline{K}^{*0} \to (3\pi^0)K^{*0}\overline{K}^{*0}$; $J/\psi \to a_0^+K^-K^{*0} \to (\eta\pi^+)K^-K^{*0} + c.c.$; $J/\psi \to \rho^+K^{*-}K^{*0} \to (\pi^+\pi^0)(K^-\pi^0)K^{*0} + c.c.$; $J/\psi \to \gamma\pi^0K^{*0}\overline{K}^{*0}$; $J/\psi \to \phi\eta' \to K^+K^-\eta\pi^+\pi^-$; for each channel a sizable MC sample is simulated. There is no peak around 2.175 GeV/c^2 in the $K^{*0}\overline{K}^{*0}$ invariant mass distribution in any background channel.

We fit the mass distribution to determine a possible signal, where three parts are included in the total probability distribution function (p.d.f): (1) for the signal p.d.f, we use the shape of the $K^{*0}\overline{K}^{*0}$ invariant mass spectrum obtained from MC simulation of $J/\psi \to \eta Y(2175) \to \eta K^{*0}\overline{K}^{*0}$ produced with the mass and width of $Y(2175)$ fixed to BaBar's results; (2) for the normalized phase space contribution p.d.f., we use the shape of the $K^{*0}\overline{K}^{*0}$ invariant mass distribution obtained in the $J/\psi \to \eta K^{*0}\overline{K}^{*0}$ MC simulation, normalized with the branching ratio obtained in the previous section; (3) for the other possible backgrounds, we use a third order Chebyshev polynomial.

The product branching ratio is determined using

$$\begin{gathered}Br(J/\psi \to \eta Y(2175)) \cdot Br(Y(2175) \to K^{*0}\overline{K}^{*0}) = \\ \frac{N^{obs}}{N_{J/\psi} \cdot \epsilon \cdot Br(K^{*0} \to K^+\pi^-) \cdot Br(\overline{K}^{*0} \to K^-\pi^+) \cdot Br(\eta \to \gamma\gamma)} = (0.7 \pm 0.8) \times 10^{-4},\end{gathered}$$

where $N^{obs} = 11 \pm 12$ is the number of signal events, $N_{J/\psi}$ is the total number of J/ψ events [92], $\epsilon = 1.57\%$ is the detection efficiency obtained from MC simulation of $J/\psi \to \eta Y(2175) \to \eta K^{*0}\overline{K}^{*0}$, where the first step decay used an angular distribution $1 + \cos^2\theta$, θ is the polar angle of the η momentum in the center of mass frame,

$Br(K^{*0} \to K^+\pi^-)$ and $Br(\overline{K}^{*0} \to K^-\pi^+)$ and $Br(\eta \to \gamma\gamma)$ are the corresponding branching fractions. The error is only the statistical error. The signal significance is only 0.88σ.

The upper limit of $Br(J/\psi \to \eta Y(2175)) \cdot Br(Y(2175) \to K^{*0}\overline{K}^{*0})$ at the 90% confidence level is obtained using a Bayesian approach [94]. We obtain the upper limit:

$$Br(J/\psi \to \eta Y(2175)) \cdot Br(Y(2175) \to K^{*0}\overline{K}^{*0}) <$$
$$\frac{N_{up}^{obs}}{N_{J/\psi}\cdot\epsilon\cdot Br(K^{*0}\to K^+\pi^-)\cdot Br(\overline{K}^{*0}\to K^-\pi^+)\cdot Br(\eta\to\gamma\gamma)\cdot(1-\sigma^{sys})} = 2.52 \times 10^{-4},$$

where $N_{up}^{obs} = 31$ is upper limit at the 90% confidence level, σ^{sys} is the systematic error discussed below, and the other symbols are defined as above.

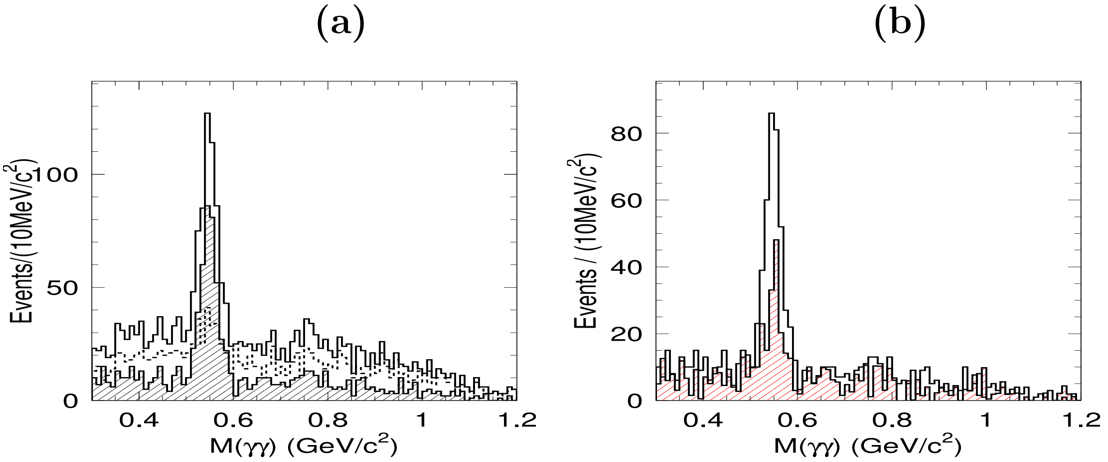

Figure A.2: (a) The $\gamma\gamma$ invariant mass spectrum for data; the dashed histogram is from the $N_\gamma > 2$ events, the shaded histogram is from the $N_\gamma = 2$ events, and the blank histogram is from all events. (b) The $\gamma\gamma$ invariant mass spectrum for $N_\gamma = 2$, where the blank histogram is from signal region events, and the shaded one is from the side-band regions events.

A.4 Systematic Errors

In this analysis, the systematic errors on the branching fraction and upper limit mainly come from the following sources:

A.4.1 MDC Tracking efficiency and kinematic fitting

The systematic errors from MDC tracking and kinematic fitting are estimated by using simulations with different MDC wire resolutions [91]. In this analysis, the systematic errors from this source are 12.8% for $J/\psi \to \eta K^{*0}\overline{K}^{*0}$ and 12.0% for $J/\psi \to \eta Y(2175) \to \eta K^{*0}\overline{K}^{*0}$.

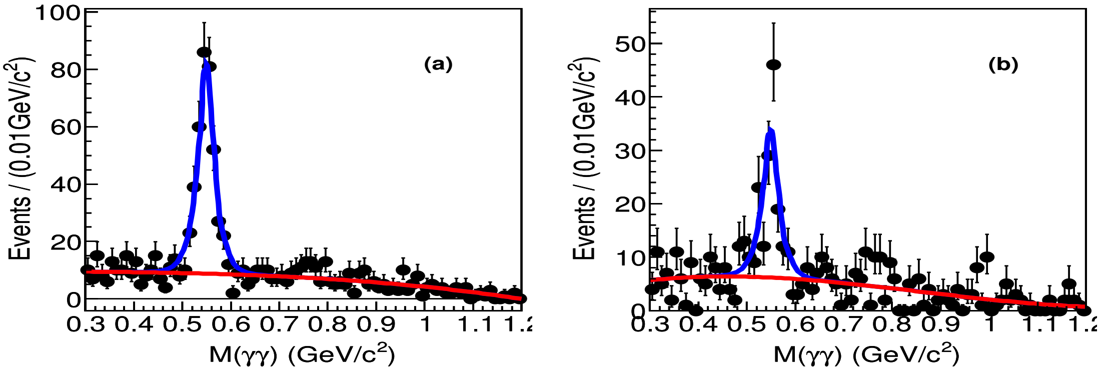

Figure A.3: Unbinned fitting results of $\gamma\gamma$ invariant mass spectra: (a) for the signal region events; (b) for the side-band region events, where the signal shape is obtained from the MC $\gamma\gamma$ invariant mass distribution and the background shape is a third order Chebyshev polynomial.

A.4.2 Photon detection efficiency

The photon detection efficiency is studied in reference [91]. The results indicate that the systematic error is less than 1% for each photon. Two good photons are required in this analysis, so 2% is taken as the systematic error for the photon detection efficiency.

A.4.3 Particle identification (PID)

In references [91] and [95], the efficiencies of pion and kaon identification are analyzed. The systematic error from PID is about 1% for each charged track. In this analysis, four charged tracks are required, so 4% is taken as the systematic error from PID.

A.4.4 Uncertainty of intermediate decay

The branching fraction uncertainties for $\eta \to \gamma\gamma$ and $K^{*0}(\overline{K}^{*0}) \to K^+\pi^-(K^-\pi^+)$ from PDG08 [94] are taken as systematic errors.

A.4.5 Number of J/ψ events

The number of J/ψ events is $(57.70 \pm 2.62) \times 10^6$, determined from the number of inclusive 4-prong hadrons [92]. The uncertainty 4.72% is taken as a systematic error.

A.4.6 Fitting

$J/\psi \to \eta K^{*0}\overline{K}^{*0}$ branching fraction

When fitting the $\gamma\gamma$ invariant mass spectrum, as described in section III.A, the η signal shape obtained from MC is fixed, and different order polynomials are used for the background shape. The difference is taken as the systematic error for the

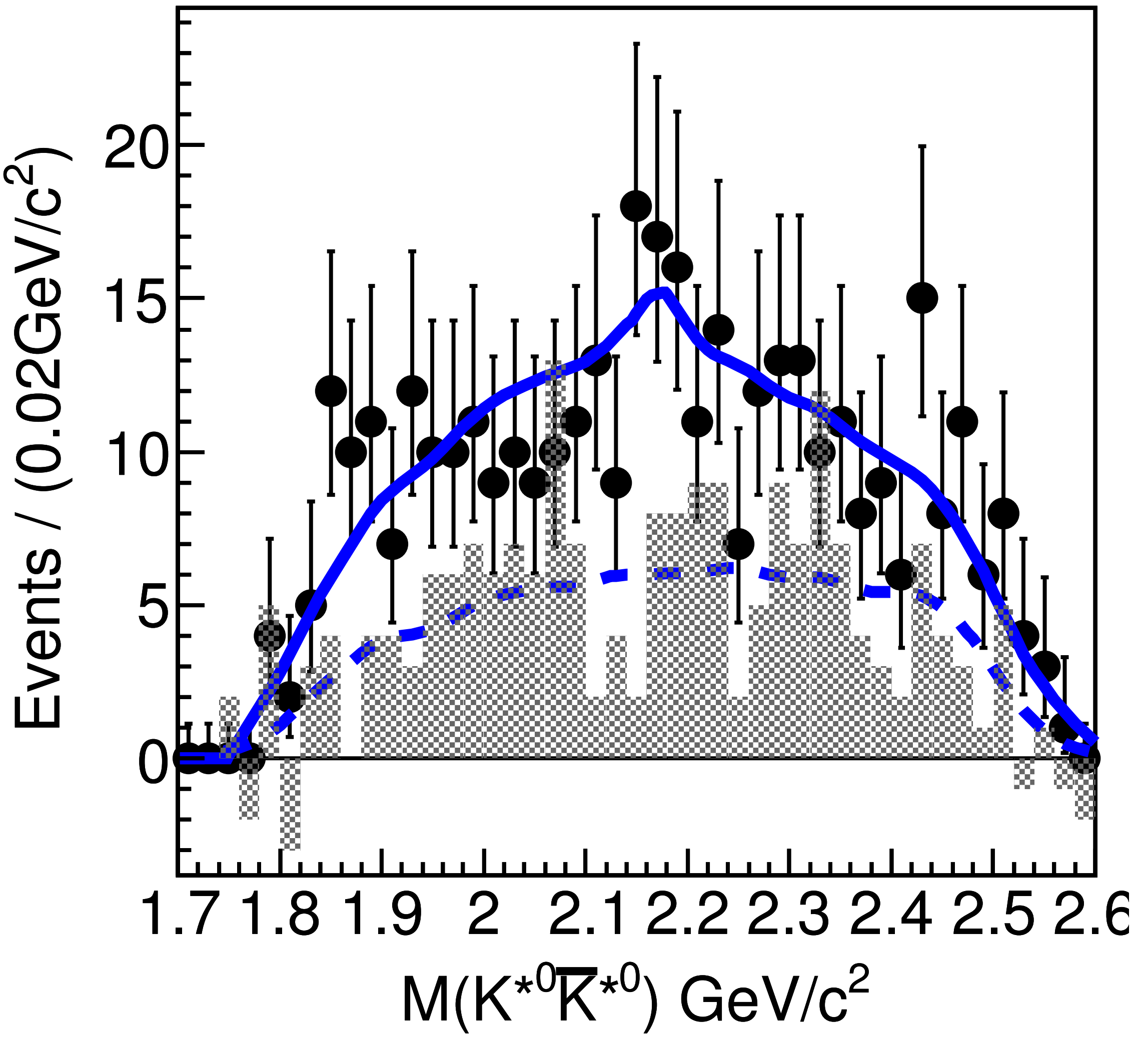

Figure A.4: The $K^{*0}\overline{K}^{*0}$ invariant mass spectrum, where points with error bars are candidate events, the dashed histogram is from MC phase space for $J/\psi \to \eta K^{*0}\overline{K}^{*0}$, the shaded histogram is from side-band events, and the solid curve is the fitting result, where the Y(2175) shape used is from MC simulation.

background uncertainty. We also use different regions in fitting the invariant mass spectrum. The total systematic error from fitting is 6.7%.

Br($J/\psi \to \eta Y(2175)$) · Br($Y(2175) \to K^{*0}\overline{K}^{*0}$) upper limit

When fitting the invariant mass spectrum of $K^{*0}\overline{K}^{*0}$, as described in section III.B, there are three sources of systematic error: for the first p.d.f, we used the different resonance parameters measured by BaBar and BES, and take the difference as the systematic error from the uncertainty of signal parameters; for the second, the systematic error comes from the error of the branching fraction of $J/\psi \to \eta K^{*0}\overline{K}^{*0}$ measured in section III.A; for the third, we used the difference between fitting with a third order Chebyshev polynomial and fitting with the invariant mass shape from $K^{*0}\overline{K}^{*0}$ side-band events as the systematic error for the background uncertainty. Combining these contributions, 16.3% is obtained as the systematic error from fitting.

A.4.7 Different selection of side-band regions

We used different side-band regions to estimate the backgrounds both in section III.A and III.B, and take the difference as a source of systematic error. The result is 10.0% for the measurement of branching fraction and 4.2% for the upper limit.

A.4.8 Number of photons

To estimate the systematic error from the requirement of two good photons, we compare the efficiency difference for this requirement between data and MC sample, and obtain 4.4%, which is taken as the systematic error from the two photon requirement.

A.4.9 K^* simulation

The K^* is simulated with a P-wave relativistic Breit-Wigner function $BW = \frac{\Gamma(s)^2 {m_0}^2}{(s-{m_0}^2)^2+\Gamma(s)^2 {m_0}^2}$, with the width $\Gamma(s) = \Gamma_0 \frac{m_0}{m} \frac{1+r^2 {p_0}^2}{1+r^2p^2} [\frac{p}{p_0}]^3$, where r is the interaction radius and the value $(3.4 \pm 0.6 \pm 0.3)(GeV/c)^{-1}$ measured by a $K^-\pi^+$ scattering experiment [96] is used. Varying the value of r by 1σ, the difference of the detection efficiencies for $J/\psi \to \eta K^{*0}\overline{K}^{*0}$, $J/\psi \to \eta Y(2175) \to \eta K^{*0}\overline{K}^{*0}$ is taken as the systematic error from the uncertainty of the r value.

The systematic errors from the different sources and the total systematic errors are shown in Table I.

A.5 Summary

With 58M BESII J/ψ events, the branching fraction of $J/\psi \to \eta K^{*0}\overline{K}^{*0}$ is measured for the first time:

$$Br(J/\psi \to \eta K^{*0}\overline{K}^{*0}) = (1.15 \pm 0.13 \pm 0.22) \times 10^{-3}.$$

Table A.1: Systematic errors (%)

Error sources	Br($J/\psi \to \eta K^{*0}\overline{K}^{*0}$)	Upper limit
MDC tracking efficiency and 4-C fitting	12.8	12.0
Photon detection efficiency	2	2
PID	4	4
Intermediate decay	~ 1	~ 1
Number of J/ψ events	4.7	4.7
Fitting	6.7	16.3
Side-band region	10.0	4.2
Photon number	4.4	4.4
K^* simulation	3.5	2.6
Total systematic error	19.5	22.3

No obvious enhancement near 2.175 GeV/c^2 in the invariant mass spectrum of $K^{*0}\overline{K}^{*0}$ is observed. The upper limit on $Br(J/\psi \to \eta Y(2175)) \cdot Br(Y(2175) \to K^{*0}\overline{K}^{*0})$ at the 90% C.L. is 2.52×10^{-4}. Due to the limited statistics, we can not distinguish whether the $Y(2175)$ is a hybrid or quarkonium state.